Electronic and vibrational properties of fullerenes and metallofullerenes studied by STM and STS

Von der Fakultät für Mathematik, Informatik und Naturwissenschaften der Rheinisch-Westfälischen Technischen Hochschule Aachen zur Erlangung des akademischen Grades einer Doktorin der Naturwissenschaften genehmigte Dissertation

vorgelegt von

Anna Stróżecka, M.Sc.

aus Bydgoszcz, Polen

Berichter: Priv.-Doz. Dr. Bert Voigtländer
Univ.-Prof. Dr. Markus Morgenstern

Tag der mündlichen Prüfung: 27 November 2007

Abstract

This thesis presents the results of a low temperature scanning tunneling microscopy (STM) study on fullerenes and endohedrally doped fullerenes. The measurements have been performed for three different molecules: C_{60}, $Ce@C_{82}$ and $Ce_2@C_{80}$, adsorbed on metal surfaces. The investigated molecules belong to different classes of the fullerene family and exhibit substantial differences in structural and electronic properties. The study has been focused mainly on the metallofullerenes, special attention has been paid to the features arising due to the presence of the encapsulated atoms. The electronic and vibrational structure of the fullerenes have been studied by scanning tunneling spectroscopy (STS) and inelastic electron tunneling spectroscopy (STM-IETS). In particular, the influence of the chemisorption on the molecular properties has been explored.

The STM images resolve the internal structure of the molecules and give insight into the bonding configuration of the fullerenes. The preferential orientation of C_{60} on Cu(111) has been established by considering the symmetry of the molecular orbitals. For $Ce@C_{82}$ on Cu(111) no favoured adsorption geometry has been found. The different bonding configurations observed for $Ce@C_{82}$ could be identified based on the density functional theory (DFT) calculations.

The investigation of the electronic properties by tunneling spectroscopy indicates that the electronic structure of the molecules is influenced by the interaction with the substrate, in particular the charge donation from Cu(111). In the STS spectrum of C_{60} an additional feature has been identified, originating from the partial filling of the LUMO orbitals of the molecule. For $Ce@C_{82}$ a strong dependence of the dI/dV spectra on the molecular orientation has been observed. Modifications in the electronic structure have been found for different bonding configurations of $Ce_2@C_{80}$. The observed changes in the electronic spectra of the metallofullerenes are related to the presence of highly localized metal-cage hybridized orbitals. As indicated by DFT calculations, such hybrid states dominate the density of states (DOS) of the endohedral fullerenes.

The inelastic tunneling spectroscopy study reveals that only few vibrational modes are active in the STM-IETS spectra of the fullerenes. Two internal cage phonons have been identified if case of C_{60}. In the vibrational spectra of $Ce@C_{82}$ only pure C_{82} modes have been resolved and no signature of the dynamics of encapsulated cerium has been found. However, in case of $Ce_2@C_{80}$, apart from the features related to the cage phonons also a low frequency mode has been observed. The theoretical calculations of the vibrational structure of the molecule indicate that the feature corresponds most

probably to the movement of Ce atoms.

Interesting conclusions follow from the spectroscopic measurements on $Ce_2@C_{80}$ molecules. The results reveal an unusually high increase in the differential conductance of this molecule at low bias voltages. The experiments indicate that the effect may be related to the excitation of vibrational modes, that strongly modify the tunneling current.

Finally also the electron transport properties of the fullerenes have been investigated. The controlled contact formation to the C_{60} and $Ce_2@C_{80}$ molecules is demonstrated. The conductance measurements of single-molecule STM junctions indicate the main differences in the transport properties of the hollow and endohedrally doped fullerenes. In particular it has been found that the encapsulation of metal ions hinders the conduction process along the carbon cage which results in the reduced conductivity of the doped fullerenes compared to the hollow species.

Zusammenfassung

In dieser Arbeit werden die experimentellen Ergebnisse einer Untersuchung von Fullerenen und endohedral dotierten Fullerenen mittels Rastertunnelmikroskopie (STM) und Rastertunnelspektroskopie (STS) präsentiert. Die Messungen wurden für drei verschiedene Moleküle durchgeführt: C_{60}, $Ce@C_{82}$ and $Ce_2@C_{80}$, die auf verschiedenen Metalloberflächen adsorbiert worden sind. Die untersuchten Moleküle gehören zu verschiedenen Klassen der Fulleren-Familie und zeigen unterschiedliche Eigenschaften. Der Schwerpunkt der Arbeit lag dabei auf der Untersuchung der Metallofullerene und deren charakteristischen Verhalten aufgrund der eingeschlossenen Atome. Mit Hilfe der elastischen (STS) und inelastischen (IETS) Rastertunnelspektroskopie wurden die molekulare Elektronen- und Vibrationsstruktur untersucht. Insbesondere wurde der Einfluss der Chemisorption auf die Eigenschaften der Fullerene erforscht.

Die STM Aufnahmen lieferten Informationen über die innere Struktur der Moleküle und ermöglichten es, die unterschiedlichen Adsorptionskonformationen, die die Moleküle auf der Oberfläche einnehmen, zu bestimmen. Die bevorzugte Orientierung von C_{60} auf der Cu(111)- Oberfläche wurde auf Grund der Molekülsymmetrie identifiziert. Um die Adsorptionskonfiguration der Metallofullerene zu ermitteln, wurden die erzielten experimentellen Ergebnisse mit DFT Berechnungen verglichen.

Die Rastertunnelspektroskopie-Messungen weisen darauf hin, dass die elektronischen Eigenschaften der Molekäle durch die Wechselwirkung mit dem Substrat modifiziert wurden. Im STS-Spektrum von C_{60} erscheint ein zusätzlicher Peak, als Folge des Ladungstransfers zwischen Fulleren und Kupferoberfläche. Bei den Metallofullerenen $Ce@C_{82}$ und $Ce_2@C_{80}$ wurde herausgefunden, dass die elektronischen Spektren von der Adsorptionsorientierung des Moleküls abhängig sind. Die beobachteten Modifikationen sind auf die stark lokalisierten Hybridorbitale zwischen den eingeschlossenen Metallatomen und dem Fulleren-Käfig zurückzuführen. Die DFT-Berechnungen deuten darauf hin, dass solche Hybridzustände die Zustandsdichte der endohedral dotierten Fullerene dominieren.

Nur wenige Vibrationsmoden der Fullerene konnten mittels STM-IETS beobachtet werden. Für C_{60} wurden zwei verschiedene Käfigvibrationen identifiziert. Auch die Spektren des $Ce@C_{82}$ Moleküls zeigen nur Käfigschwingungen und es wurde kein charakteristisches Zeichen der Dynamik des eingeschlossenen Ce-Atoms gefunden. Jedoch wurde im Fall des $Ce_2@C_{80}$ Moleküls neben den Käfigschwingungen auch eine zusätzliche Schwingung bei niedrigen Frequenzen gefunden. Mittels DFT Berechnungen konnte diese Schwingung den Ce-Atomen zugeordnet werden.

Interessante Erkenntnisse konnten aus den spektroskopischen Messungen am $Ce_2@C_{80}$ Molekül gewonnen werden. Die erzielten Ergebnisse zeigen eine außergewöhnliche Zunahme des differenziellen Leitwerts bei niedrigen Spannungen. Die experimentellen Daten deuten an, dass dieser Effekt mit einer Anregung der Molekülschwingung verbunden ist.

Die Ladungstransporteigenschaften der Fullerene wurden zusätzlich untersucht. Die kontrollierte Bildung eines Kontakts zwischen dem Molekül und der STM-Spitze wurde demonstriert. Es wurden Messungen der Leitfähigkeit einzelner Molekülen durchgeführt und der Einfluss der inneren Metallatome auf die Leitfähigkeit des Fullerens studiert. Dabei stellte sich heraus, dass die Anwesenheit der Metallatome im Käfig den Ladungstransport durch das Molekül behindert. Daher besitzen dotierten Fullerene eine etwa fünfmal niedrigere Leitfähigkeit als nicht dotierten Fullerene.

Contents

Chapter 1

Introduction

Over the last decades, the technological progress has made it possible to investigate and control the matter on the atomic level. The reason for the growing interest in the nanoscience is, apart from the hope of futher miniaturization of the microelectronic devices, also the prospect of understanding the novel physical and chemical behavior occurring at the nanometer scale. The study of single atoms and molecules provides new insight into the processes on surfaces and gives a crucial basis for fabrication of the nanostructured materials with potential applications in molecular electronics [1, 2] or spintronics [3, 4].

With the invention of the scanning tunneling microscope (STM) by Binnig and Rohrer [5, 6], a new method appeared to deal with nanometer scale structures. STM is a powerful tool to investigate and control properties of single molecules and their interaction with the environment. Measurements at low temperature ($T = 7\,\mathrm{K}$) allow to combine the imaging capabilities of STM with spectroscopic analysis, manipulation and chemical modification, which gives insight in the phenomena not accessible to other techniques [7]. The first molecules observed with the STM were phthalocyanine [8] and benzene [9]. Since then, a great variety of molecules have been studied and a number of fascinating experiments have been presented, among them: electronic and vibrational spectroscopy of molecules [10, 11], observation of negative differential resistance (NDR) [12], manipulation of single adsorbates [13, 14, 15], vibration induced motion [16, 17, 18], chemical bond breaking and dissociation of molecules [19, 20], controlling a chemical reaction [21, 22] or photo-induced resonant tunneling [23].

Among the investigated nanostructured materials a special attention is paid to the carbon-based systems, including nanotubes and fullerene-based compounds [24, 25]. The C_{60} molecule has became a custom 'building block' of the nanoscience and the base for synthesis of novel molecular materials. To the family of fullerene-based structure belong, i.e. intercalated fullerites [26, 27], polymers [28] or functionalized fullerenes [29]. One of the fascinating features of fullerenes is that an atom or a small molecule can be introduced into the empty space inside the carbon cage [30]. The resulting endohedral complexes have several advantages over the hollow fullerenes, since their properties can be tuned by doping with different type of atoms without changing the structure of the outer shell [31]. Of special interest are the metallofullerenes. The possible

isolation of magnetic or radioactive metal atoms from the surrounding environment has made endohedral fullerenes interesting for many fields, including interdisciplinary areas like biology and medicine [32]. The potential applications include electronic devices [33], spin-based quantum computing [34, 35] and medical applications, e.g. magnetic resonance imaging (MRI) [36].

However, the endohedral fullerene research has been hindered so far by the limited availability of the material, due to a low production yield and difficult purification process. Therefore, even though the properties of metallofullerenes in solutions are relatively well studied, a number of questions regarding the chemisorbed metallofullerenes still remains open. Futher studies are required to determine the influence of the chemisorption on the electronic structure of the molecules, especially how the molecule-substrate interaction affects the metal-cage bonding. Another issue is the identification of the intramolecular vibrational modes of the adsorbed fullerenes, where of highest interest is the dynamics of the encapsulated species. Finally, charge transport properties of the metallofullerenes need to be established, in particular the role of the encaged atoms.

Investigation of these issues has been the main aim of this thesis. The work has been done within the project[1] bringing together the areas of chemistry, experimental physics and theoretical modelling, with the goal of establishing the properties of adsorbed endohedral complexes, in particular cerium metallofullerenes. Cerium is one of the most reactive elements of rare earth series. Its complex physical behavior, arising from the presence of a localized $4f$ electron, makes the Ce-based complexes the important members of the endohedral fullerene family, with potentially intriguing properties. The thesis summarizes the results obtained for three different molecules: C_{60}, $Ce@C_{82}$ and $Ce_2@C_{80}$, adsorbed on metal surfaces. The measurements have been performed on a low temperature scanning tunneling microscope. The study has been focused on the investigation of the electronic and vibrational structure of the individual molecules, by means of elastic and inelastic scanning tunneling spectroscopy.

The thesis is organized as follows.

Chapter 2 briefly introduces the principles of scanning tunneling microscopy. The emphasis is laid on the discussion of the spectroscopic techniques: scanning tunneling spectroscopy (STS) and STM-based inelastic electron tunneling spectroscopy (STM-IETS). Also a short introduction to the lateral manipulation of single adsorbates is given.

Chapter 3 describes the main properties of fullerenes and endohedrally doped fullerenes. The particular sections summarize the structural, electronic and vibrational properties of C_{60} and rare-earth endohedral complexes. The principles of the production and purification of metallofullerenes are briefly introduced.

[1] Marie Curie Actions, MEST-CT-2004-506854 (NANOCAGE - Imaging, Spectroscopy and Theory of Caged Atoms)

Chapter 4 shortly discusses the synthesis and purification of cerium metallofullerenes. It also gives the description of the experimental apparatus, sample preparation and measuring procedures.

Chapter 5 summarizes the findings regarding the properties of C_{60} adsorbed on Cu(111). The results reveal the influence of the charge transfer from the substrate on the electronic and vibrational structure of the fullerenes. It is also demonstrated that the lateral manipulation technique can be used to assemble artificial molecular nanostructures.

Chapter 6 presents the results of the study of $Ce@C_{82}$ metallofullerene. The orientation of the molecules with respect to the substrate has been identified by comparison of the experimental and simulated STM images. The calculations allow also to interpret the electronic features resolved by STS, and indicate that the structure of the molecule observed in STM is dominated by the cerium-cage hybridized states.

Chapter 7 is focused on the properties $Ce_2@C_{80}$ metallofullerene. The results of the elastic and inelastic tunneling spectroscopy are discussed in detail. Especially interesting conclusions follow from the energy resolved spatial mapping of the electronic and vibrational features. In the vicinity of the Fermi energy, drastic changes in the differential conductance of the molecule are observed. The experiments suggest that this intriguing behavior is related to the excitation of molecular vibrational modes.

Chapter 8 discusses the electron transport properties of the fullerenes. The measurements of the conductance of a single-molecule STM junction are presented. The results reveal important differences in the transport character in case of hollow and endohedrally doped fullerenes.

Finally, **Chapter 9** summarizes the results presented in this work.

Chapter 2

Scanning Tunneling Microscopy

2.1 Principles

Scanning tunneling microscopy (STM), invented by Binning and Rohrer in 1982 [6, 5], was the first scanning probe technique that offered the possibility to observe the matter in the real space and on the atomic scale.

The principle of STM is based on the quantum tunneling phenomenon, i.e. the current tunneling through a potential barrier. The basic idea of STM is illustrated in Fig. 2.1(a). A sharp metallic tip is brought close to the sample. The lateral tip position (x and y) as well as the vertical position z are controlled on the subatomic scale by the voltage applied to the piezoelectric actuator elements. If the distance between tip and sample is small enough (typically between 5-10Å), so that wave functions of the two surfaces overlap, the electrons can tunnel through the vacuum barrier, when the bias voltage V is applied between tip and sample. The corresponding potential energy diagram is shown in Fig. 2.1(b). Once the sample and tip are brought in thermodynamical equilibrium, their chemical potentials equalize. When the voltage V is applied to the sample, the Fermi levels of the two materials are shifted with respect to each other, allowing the current to flow.

The resulting tunneling current I depends exponentially on the tip-sample distance z:

$$I = I_0 e^{-2\kappa z} \tag{2.1}$$

where $\kappa = \sqrt{2m\overline{\Phi}/\hbar^2}$ is an inverse decay length and $\overline{\Phi} = \frac{\Phi_t+\Phi_s}{2} - \frac{eV}{2}$ is the mean barrier height. Typically 1 Å displacement in z yields one order of magnitude change in current, which corresponds to the decay length $\kappa \approx 1\,\text{Å}^{-1}$. With this level of sensitivity, tunneling current can be used to control the tip-sample separation with very high vertical resolution. When the tip is scanned along the surface in the x and y directions, the feedback mechanism constantly adjusts the tip height, by approaching or withdrawing the tip, so that the tunneling current remains constant. The record of the feedback signal, as the function of the lateral position of the tip, gives a map of the surface topography. This way of imaging is called a "constant current" mode. The alternative scanning mode is the "constant height" mode, when the height of the tip is

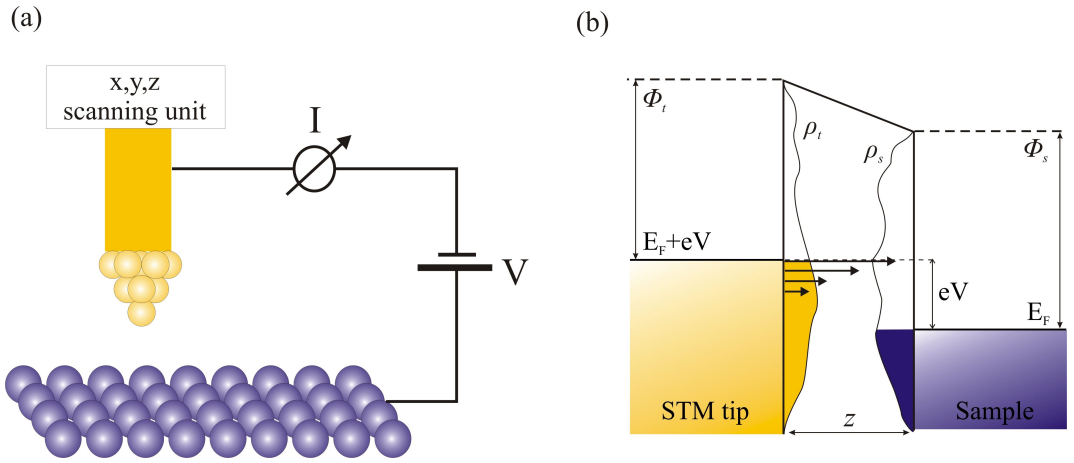

Figure 2.1: (a) Schematic drawing of the scanning tunneling microscope. When the bias voltage V is applied between tip and sample the tunneling current I is measured. (b) Corresponding energy level diagram of tip and sample. The applied bias shifts the Fermi level by $\pm|eV|$. Density of states of tip and sample is represented by ρ_t and ρ_s respectively (the filled states are colored). Φ_t and Φ_s are the work functions of tip and sample.

kept constant and the features of the surface are reflected as changes in the tunneling current. However, the constant height mode can be practically used only in the cases when the surface is extremely flat.

2.2 Theory of Scanning Tunneling Microscopy

The image obtained by STM does not correspond directly to the topography of the surface but contains also information about the surface and tip electronic structure. Therefore the interpretation of results is usually not trivial. The proper modelling of tunneling process requires good understanding of the electronic structure of both tip and sample and the interaction between them.

Soon after the invention of scanning tunneling microscope various theoretical models were developed in order to fully explain the STM experiments. Already in 1961 Berdeen proposed a model of the planar tunneling junction based on the time-dependent perturbation approach [37]. By neglecting the interaction between the two separately considered electrodes he showed that the tunneling probability of the electron is determined by the overlap of the surface wavefunctions. The tunneling matrix element M can be calculated as

$$M = -\frac{\hbar^2}{2m}\int_S d\vec{S}(\psi^*\nabla\chi - \psi\nabla\chi^*). \tag{2.2}$$

The integral is done on the separation surface S between the two electrodes, the wavefunctions of the electrodes are ψ and χ.

Based on this formalism, the tunneling current can be evaluated by summing over all the relevant states

$$I = \frac{4\pi e}{\hbar} \int_{-\infty}^{\infty} [f(E_F + \epsilon) - f(E_F - eV + \epsilon)] \times \rho_S(E_F + \epsilon)\rho_T(E_F - eV + \epsilon)|M|^2 d\epsilon \quad (2.3)$$

where $f(E)$ is the Fermi-Dirac distribution defined as $f(E) = (1 + \exp(E/k_BT))^{-1}$, V is the voltage applied between the electrodes and ρ_S and ρ_T are the local densities of states (LDOS) of sample and tip respectively. The above equation can be simplified in the limit of low temperatures. The Fermi-Dirac distribution is then approximated by the step function and Eq. (2.3) becomes

$$I = \frac{4\pi e}{\hbar} \int_{0}^{eV} \rho_S(E_F + \epsilon)\rho_T(E_F - eV + \epsilon)|M|^2 d\epsilon. \quad (2.4)$$

Assuming futher that the tunneling matrix element $|M|$ does not change significantly with the voltage, we obtain

$$I \propto \int_{0}^{eV} \rho_S(E_F + \epsilon)\rho_T(E_F - eV + \epsilon) d\epsilon \quad (2.5)$$

Obtained relation for the tunneling current (Eq. (2.5)) points out, that what STM actually measures is the convolution of the DOS of both tip and sample. Since both DOS enter the formula symmetrically, the tunneling current is equally determined by the electronic structure of tip and sample.

In the Bardeen approach tip and sample are treated as separate subsystems with a planar geometry. The first theory of STM including the non-planar tip geometry was developed in 1983 by Tersoff and Hamman [38, 39]. The tip was modelled as locally spherical, having only s-type wavefunctions. The model shows that, in the limit of low voltage and low temperature, the tunneling current becomes

$$I \propto \frac{e^2 V}{\hbar} \rho_S(\overrightarrow{r_0}, E_F)\rho_T(E_F). \quad (2.6)$$

A constant-current STM image can be then interpreted as contour of constant LDOS of the surface at the Fermi level, $\rho_S(E_F)$, measured at the tip curvature center $\overrightarrow{r_0}$.

2.3 Scanning Tunneling Spectroscopy

One of the capabilities of STM is a direct probing of the electronic states of the sample [40, 41]. The technique which allows the local spectroscopic analysis of the surface is called scanning tunneling spectroscopy (STS).

The local density of states (LDOS) of the surface can be determined from the current-voltage characteristic of the tunneling junction. The expression for the tunneling current calculated within the Bardeen approach (Eq. (2.4)) involves the integration

over all the electron states between the Fermi level and the applied voltage. To access the electronic states at the given energy the derivative of the current dI/dV has to be determined. The relation between the dI/dV and LDOS of the surface can be shown by evaluating the derivative of Eq.(2.4). Denoting the mean transmission rate per energy ΔE as $M(E,V) = \langle|M|^2\rangle$, where E is the energy of tunneling electron with respect to E_F, we can rewrite the formula (2.4) as

$$I \propto \int_{E_F}^{E_F+eV} \rho_S(E)\rho_T(E-eV)M(E,V)dE. \tag{2.7}$$

Taking the derivative leads to

$$\begin{aligned}\frac{dI(V_0)}{dV} \propto\ & \rho_S(E_F+eV_0)\rho_T(E_F)M(E_F+eV_0,V_0) + \\ & + \int_{E_F}^{E_F+eV_0} \rho_S(E)\frac{d\rho_T(E')}{dE'}\Big|_{E'=E-eV_0} M(E,V_0)dE + \\ & + \int_{E_F}^{E_F+eV_0} \rho_S(E)\rho_T(E-eV_0)\frac{dM(E,V)}{dV}\Big|_{V=V_0} dE\end{aligned} \tag{2.8}$$

The equation can be simplified by assuming that the tip density of states ρ_T and the transmission probability M are constant over the considered energy range. The two integrals in Eq. (2.8) vanish and only first term is left:

$$\frac{dI(V_0)}{dV} \propto \rho_S(E_F+eV_0)\rho_T(E_F)M(E_F+eV_0,V_0). \tag{2.9}$$

This yields that differential conductance is proportional to the local density of states of the sample

$$\frac{dI(V_0)}{dV} \propto \rho_S(E_F+eV_0). \tag{2.10}$$

Relation (2.10) is valid only upon the assumption that the transmission probability M is constant. However, in reality the transmission probability strongly depends on both voltage and tip-sample separation. As showed by Feenstra [40, 41, 42], this voltage and distance dependence can be removed by the normalization of the differential conductance dI/dV by the total conductance I/V. The obtained dimensionless quantity, $(dI/dV)/(I/V) = d(lnI)/d(lnV)$, called normalized conductance, provides a good approximation of the normalized density of states [43]. The cancellation of the separation dependence can be seen by considering the theoretical expression of the tunneling current (Eq. (2.7)).

Assuming constant DOS of the tip, dividing the Eq. (2.8) by the I/V yields:

$$\frac{dI/dV}{I/V}\Big|_{V=V_0} \propto \frac{\rho_S(E_F+eV_0)}{\frac{1}{eV}\int_{E_F}^{E_F+eV_0}\rho_S(E)\frac{M(E,V_0)}{M(E_F+eV_0,V_0)}dE} + \\ + \frac{\int_{E_F}^{E_F+eV_0}\frac{\rho_S(E)}{M(E_F+eV_0,V_0)}\frac{dM}{dV}dE}{\frac{1}{eV}\int_{E_F}^{E_F+eV_0}\rho_S(E)\frac{M(E,V_0)}{M(E_F+eV_0,V_0)}dE} \tag{2.11}$$

The terms $M(E,V_0)$ and $M(E_F+eV_0,V_0)$ appear as ratios in this equation and their dependances on the voltage and tip-sample separation tend to cancel. The first term of the Eq. (2.11) gives us then that in the first approximation the normalized differential conductance is proportional to the normalized density of states:

$$\frac{dI/dV}{I/V}\Big|_{V=V_0} \approx \frac{\rho_S(E_F+eV_0)}{\frac{1}{eV}\int_{E_F}^{E_F+V_0}\rho_S(E')dE'}. \tag{2.12}$$

The second term gives rise to a smoothly varying background.

Experimentally, the dI/dV signal can be measured by lock-in amplifier, using the AC modulation technique. A small voltage modulation $V_{mod}\cos(\omega t)$ applied to the tunneling voltage induces an in-phase modulated contribution to the tunneling current. This signal can be detected by lock-in amplifier and its amplitude is for small modulation voltages proportional to dI/dV. The contribution of the dI/dV to the tunneling current can be clearly seen by expanding the current in a Taylor series (the higher order terms are neglected)

$$I(V_0+V_{mod}cos(\omega t)) = I_0+\underbrace{\frac{dI(V_0)}{dV}V_{mod}}_{lock-in\ signal}cos(\omega t)+\frac{d^2I(V_0)}{dV^2}V_{mod}^2\underbrace{cos^2(\omega t)}_{\frac{1}{2}(1+\cos(2\omega t))}+\dots \tag{2.13}$$

From the equation it follows that the n-th derivative of the current can be measured by lock-in detection of the amplitude of the signal at n-times the modulation frequency. The quantity d^2I/dV^2 is important for studying the processes related to the inelastic tunneling, e.g. excitation of vibrational modes of the molecules [10] or spin flips of atoms [4]. The inelastic electron tunneling spectroscopy, based on the measurements of d^2I/dV^2, is explained in detail in the next section.

The STS spectrum is acquired using the following method: the tip is positioned over the surface; the feedback loop is disabled; the dI/dV signal is recorded over the desired range of voltages. Normally during the measurement the tip-sample separation is kept fixed. However, when the tunneling conductivity varies strongly over the measured voltage range, it becomes necessary to change the tip-sample distance during recording the

spectrum, in order to amplify the tunneling current at low bias to a conveniently measurable value. Such acquisition method gives a wide dynamic range of tunneling current and conductivity. The distance dependence, resulting from the varying separation, can be removed by the normalization of the data, as discussed above.

The last important issue to mention, is the role of the tip density of states. The spectra acquired with STM always contain information about the electronic states of the tip and dI/dV is a good approximation of the sample density of stated only for the tips with a flat DOS ($\rho_T(V) \approx const$). In the actual experiment however, the tip DOS is not always constant, and a special procedure to control the condition of the tip is necessary. In case of the adsorbates on the metal surfaces, the reference measurement can be done on the clean substrate. Only the tips giving the expected reference spectrum of bare surface can be used for probing the density of states of the adsorbate.

2.3.1 Spectroscopic imaging

More information about the electronic structure of the surface can be gained by the spatial mapping of a specific spectroscopic feature [44]. A spectroscopic image yielding the map of the LDOS can be obtained by performing a slow constant current STM scan at the certain bias voltage V_0 and simultaneous recording of the dI/dV signal. The parameters of the scan have to be chosen carefully, so that the voltage modulation frequency is above the bandwidth of the feedback.

2.4 Inelastic Electron Tunneling Spectroscopy

The inelastic electron tunneling spectroscopy (IETS) was first demonstrated by in 1966 Jaklevic and Lambe [45], who showed that the tunneling electrons are able to excite the vibrational modes of the molecules buried at the metal-oxide interface of a metal-oxide-metal tunneling junction. The vibrations are excited due to the the inelastic scattering processes occurring in the tunneling junction. Soon after invention of the STM, it has been proposed that similar mechanism of vibrational excitation should be possible in STM [46]. Here, the two metal electrodes are substituted by tip and sample, and oxide layer by tip-sample vacuum gap.

First molecular vibrational spectra acquired by STM have been demonstrated by Stipe *et al.* [10]. In the last years, the investigation of inelastic processes gave also new insight into the fundamentals of single molecule chemistry, e.g. intra molecular energy transfer [18, 47, 48], chemical reactions on surfaces [20, 21, 22] or conformational changes [12]. The review on the development of the STM-IETS technique can be found in Ref. [7, 11, 49].

The principle of the inelastic spectroscopy with STM is illustrated in Fig. 2.2(a). The tip is positioned over the molecule and the bias voltage between tip and sample is increased. The excitation of the molecular vibration becomes possible when the energy of the tunneling electrons reaches the energy of the vibrational mode. At this threshold voltage, a new inelastic electron tunneling channel opens. This process is accompanied

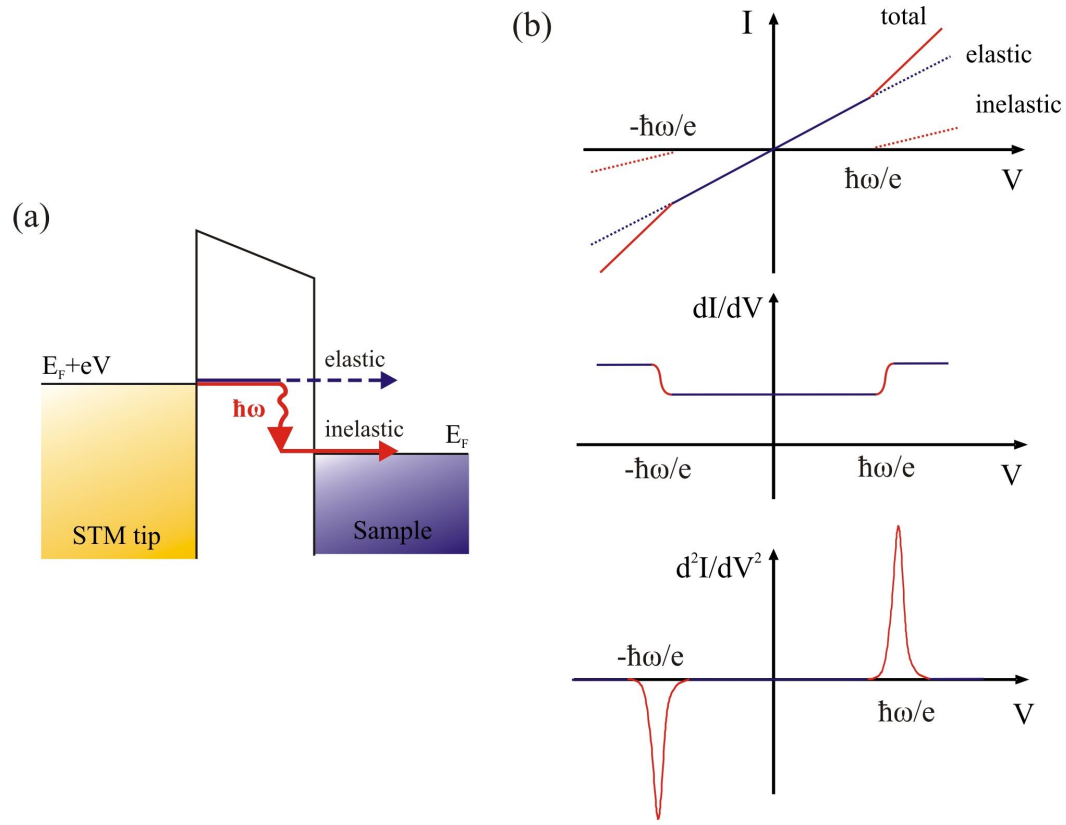

Figure 2.2: (a) Schematic drawing of the potential diagram of the STM illustrating the principle of the inelastic spectroscopy. Molecular vibrations are excited by the inelastically tunneling electrons. The inelastic channel opens when the bias voltage crosses the threshold corresponding to the energy of the vibrational mode $\hbar\omega$. (b) The effect of the inelastic process on the current-voltage characteristics. The current consists of inelastic and elastic contribution. The inelastic channel opens at the threshold voltage $V \geq \hbar\omega/e$. In result, a step-like increase is observed in dI/dV curve. In d^2I/dV^2 spectrum a characteristic peak and dip appear symmertically around E_F, at bias voltage corresponding to the energy of vibrational mode.

by a slight increase in the tunneling current and corresponding to it abrupt change in the conductance dI/dV. The change in the dI/dV is usually too small to be detected, so the information about vibrational modes is extracted from the d^2I/dV^2 signal, where a clear peak appears at the threshold voltage. The mode can be excited by electrons tunneling in both directions: from tip to the sample and from sample to the tip. This implies an important feature of the STM vibrational spectrum: the dip occurs in the negative bias voltage, symmertically to the peak in the positive bias. The effect of the opening of the inelastic channel on the I, dI/dV and d^2I/dV^2 curves is schematically shown in Fig. 2.2(b).

The influence of the inelastic excitation on the dI/dV and d^2I/dV^2 spectra can be understood by considering a simple model of the tunneling current [45]. The model

can describe the position and width of the peaks at the finite temperature, treating the electron-molecule interaction as a parameter. In Section 2.2 (Eq. (2.6)) it has been shown that in the limit of low temperature and low voltages the elastic current I_e is proportional to the bias voltage: $I_e = \sigma_e V$. The excitation of vibration gives rise to the inelastic contribution I_e, as schematically shown in Fig. 2.2(b). The additional current I_e can evaluated by considering the tip-sample tunneling associated with releasing the energy $\hbar\omega$, taking into account the Fermi-Dirac distributions of tip and sample. The total tunneling current, $I = I_e + I_i$, can be then represented as

$$I = \sigma_e V + \frac{\sigma_i}{e}\int_{-\infty}^{\infty}[\underbrace{f(\epsilon - eV + \hbar\omega)(1 - f(\epsilon))}_{tip\rightarrow sample} + \underbrace{f(\epsilon)(1 - f(\epsilon - eV - \hbar\omega))}_{sample\rightarrow tip}]d\epsilon. \tag{2.14}$$

where, the σ_e and σ_i are denote the elastic and inelastic linear conductance. The $f(E)$ is the Fermi-Dirac distribution, defined as $f(E) = (1 + \exp(E/k_BT))^{-1}$. The first term of the inelastic contribution describes the tunneling form tip to the sample, the second term corresponds to the tunneling from sample to the tip. The constant σ_i defines the intensity of the vibrational feature and is determined by the electron-molecule interaction, in particular electron-phonon coupling. Solving the integral in Eq. (2.14) analytically gives [45]:

$$I = \sigma_e V + \frac{\sigma_i}{e}\left(\frac{(eV_0 - \hbar\omega)g(eV_0 - \hbar\omega)}{g(eV_0 - \hbar\omega) - 1} + \frac{(eV_0 + \hbar\omega)g(-eV_0 - \hbar\omega)}{g(-eV_0 - \hbar\omega) - 1}\right) \tag{2.15}$$

where function $g(E)$ stands for $g(E) = \exp(E/k_BT)$.

Taking the derivative of this equation with respect to the tunneling voltage yields:

$$\begin{aligned}\frac{dI(V_0)}{dV} = \sigma_e + \sigma_i\Bigg(&\frac{g(eV_0 - \hbar\omega)\Big(g(eV_0 - \hbar\omega) - 1 - \dfrac{eV_0 - \hbar\omega}{k_BT}\Big)}{\Big(g(eV_0 - \hbar\omega) - 1\Big)^2} + \\ &+ \frac{g(-eV_0 - \hbar\omega)\Big(g(-eV_0 - \hbar\omega) + 1 + \dfrac{eV_0 + \hbar\omega}{k_BT}\Big)}{\Big(g(-eV_0 - \hbar\omega) - 1\Big)^2}\Bigg)\end{aligned} \tag{2.16}$$

The complex equation (2.16) can be simplified to the formula :

$$\frac{dI(V_0)}{dV} = \sigma_e + \sigma_i\Big(\tilde{f}(-eV_0 + \hbar\omega) + \tilde{f}(eV_0 + \hbar\omega)\Big), \tag{2.17}$$

where $\tilde{f}$ is a modified Fermi-Dirac distribution: $\tilde{f}(E) = (1 + \exp(E/1.46k_BT))^{-1}$ [50]. The resulting dI/dV curve exhibits a step-like increase symmetrically around E_F at $\pm\hbar\omega$, as schematically shown in Fig. 2.2(b). The usual increase in the differential conductance cause by excitation of vibration is in the range 1-10%.

Calculation of the second derivative leads to the following expression for d^2I/dV^2 [45]:

$$\frac{d^2I(V_0)}{dV^2} = \sigma_i \frac{e^2}{k_BT}\Bigg(g(eV_0-\hbar\omega)\frac{(\frac{eV_0-\hbar\omega}{k_BT}-2)g(eV_0-\hbar\omega)+\frac{eV_0-\hbar\omega}{k_BT}+2}{\Big(g(eV_0-\hbar\omega)-1\Big)^3}+ \\ + g(-eV_0-\hbar\omega)\frac{(\frac{-eV_0-\hbar\omega}{k_BT}-2)g(-eV_0-\hbar\omega)+\frac{-eV_0-\hbar\omega}{k_BT}+2}{\Big(g(-eV_0-\hbar\omega)-1\Big)^3}\Bigg) \quad (2.18)$$

The formula 2.18 describes the asymmetric peak and dip at $\pm\hbar\omega/e$, as shown in Fig. 2.2. The predicted linewidth at half-maximum of the peak, due to the finite temperature, is equal to $5.4\,k_BT$ [45].

Experimentally, the d^2I/dV^2 signal is measured using a lock-in technique, as briefly described in Section 2.3. To detect by lockin amplifier the small change in conductance (maximum of 10%) a relatively long acquisition time is necessary and the stability of the STM becomes a crucial issue. The required stability conditions, as well as the high energy resolution, can be achieved only at cryogenic temperatures. Apart from the broadening due to the finite temperature, included in Eq. 2.16, also the modulation voltage broadens the detected signal. Detailed description of the influence of experimental parameters on the STM-IETS spectrum can be found in Ref.[51].

The main advantage of STM-IETS is the possibility to study the vibrations of single molecules in the well defined and controlled environment, however, the disadvantage is the small number of active modes. Extensive theoretical works have been carried to understand the fundamentals of the excitation mechanism [52, 53, 54, 55], but until now no clear selection rules have been defined. The complete theoretical description of STM-IETS, including the electron-molecule interaction, is based on many-body extension of Tersoff and Hamann approach. The electron-vibration coupling is treated as a perturbation. The vibration couples the final state f of the tunneling electron with the initial state i by the presence of the deformation potential δv, giving the matrix element $\langle\varphi_f|\delta v|\varphi_i\rangle$. The potential δv is defined as the change of one electron potential due to the movement of the nucleus. The final and initial electronic states $\langle\varphi_f|$ and $|\varphi_i\rangle$ are calculated by the density functional theory (DFT). Details of the theoretical analysis can be found in Ref.[53, 55]. The main conclusions of the model are:

- The electron-phonon coupling, and hence the intensity of the vibrational signal in STM-IETS, is strongly influenced by the electronic structure of the adsorbate near the Fermi energy.
- The inelastic contribution to the conductance is related to the energy transfer from the tunneling electron to the vibration quantum. It involves the modification of the adsorbate's wavefunction due to the excitation of vibration. The change of the wavefunction alters the tunneling probability and gives in result the increase of the conductance.

- The opening of the inelastic channel modifies also the elastic tunneling. The change in elastic tunneling is related to the many-body exchange effects, namely the exchange process between the tunneling electron and the electron from the Fermi gas, via a virtual excitation and de-excitation of the vibration. This term gives always a negative contribution to the conductance. The decrease is the strongest, when the adsorbate exhibits a very high density of states (sharp resonance) at the Fermi level.

- The total change in the conductance is the sum of the inelastic (positive) and elastic (negative) contributions. This cancelling effect is responsible for the intensity and number of observed modes.

The spatial map of the STM-IETS feature can be obtained in the similar way as the maps of the LDOS (look Section 2.3.1). The mapping of the intensity of vibrational signal gives more understanding of the basis of the excitation process and for some molecules enables the localization of molecular bonds [54].

2.5 Lateral manipulation of single adsorbates

The scanning tunneling microscope, initially intended to image the surfaces, has also been used as an operative tool, capable of manipulating the adsorbate on the surface. The idea using the STM tip to reposition the single atoms was first realized by Eigler and Schweizer [14], by manipulation of the Xe atoms on Ni(110) surface. Since then, the manipulation technique has been used to fabricate artificial atomic-scale nanostructures [15] and investigate the novel quantum phenomena, e.g. electron standing-waves [56], electron life-time inside a nanostructure [57] or quantum transport [58]. The manipulation experiments are usually performed at cryogenic temperatures, when the diffusion and motion of the molecule is frozen. However for some systems, mostly molecules on semiconductor surfaces, manipulation has been proved to be possible also at room temperatures [59, 60].

Two main techniques of manipulation can be distinguished: lateral manipulation and vertical manipulation. In the lateral manipulation, the moved adsorbate stays all the time bounded to the surface. In the vertical manipulation the adsorbate is picked up by the tip and released in a different location [13]. In this work the lateral manipulation has been used and the details of this technique are considered in the following.

The lateral manipulation is usually performed by using the following procedure:

- The bias voltage is decreased and simultaneously the tunnelling current is increased, so the tunnelling resistance drops down and the STM tip approaches the surface.

- The tip is moved in the lateral direction in the constant current or constant height mode. The molecule moves along the surface due the interaction with the tip.

- The tip is moved back to the normal imaging-height.

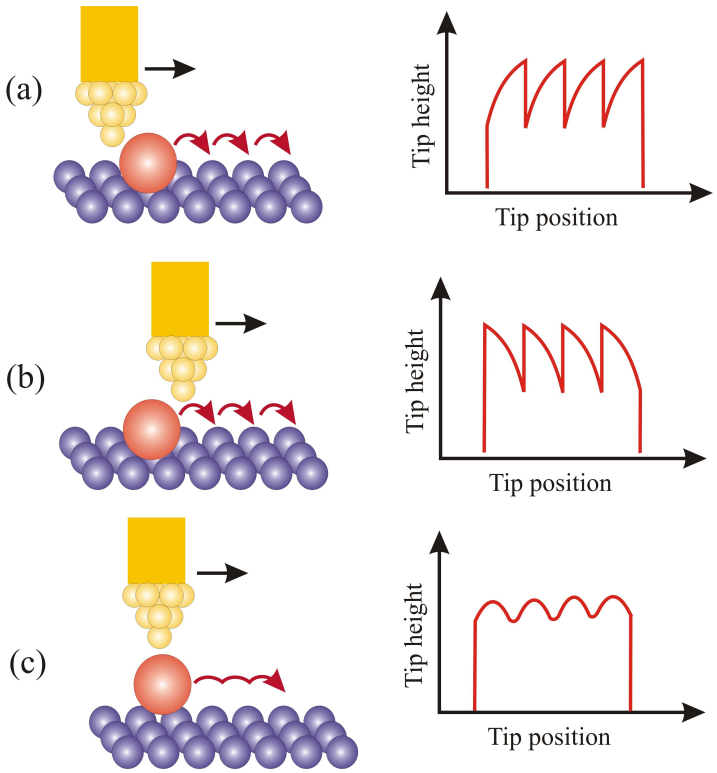

Figure 2.3: Schematic drawing of the manipulation mechanisms, together with the corresponding plots of the tip height during manipulation: (a) pushing, (b) pulling and (c) sliding.

The movement of the adsorbate is driven by the tip-adsorbate interaction, i.e. the van der Waals or chemical forces. More information about the nature of this interaction can be gained by recording the response of the STM feedback (in constant current manipulation mode) or the tunneling current (in constant height manipulation mode) during the manipulation procedure. Based on the type of the forces involved, three different manipulation mechanisms have been determined: pushing, pulling and sliding [61]. The three processes are shown schematically in Fig. 5.7, together with the characteristic plots of the tip height.

The *pushing* manipulation mechanism involves the repulsive interaction between the adsorbate and the tip. In the initial part the tip starts to move up the contour of the molecule. At some point, due to the repulsive forces, the atom or molecule jumps forwards, what is seen as a sudden decrease in the tip height. The whole process repeats again. The *pulling* takes place when the adsorbate experiences an attractive interaction with the tip. The molecule follows the tip by hopping from one adsorption site to the next one. The upward jump of the tip corresponds to the moment when the attractive interaction forces the molecules to towards the tip. Applying higher attractive forces leads to the sliding mechanism, when the molecule is manipulated in a continuous way. The distance between the tip and the adsorbate remains almost constant and the tip

scans the corrugation of the surface.

From tip height plot one can determine the hopping distance of the adsorbate during lateral manipulation. The periodicity of plot reflects the periodicity of the substrate. The simple tip trajectories presented schematically in Fig. 5.7 are usually observed when atom/molecule is manipulated along a close-packed row direction ([110] direction) on face-centered-cubic (fcc) (111) surfaces [62]. The plots become more complex for manipulation away from the [110] direction or for manipulation of large molecules. The detailed analysis of the tip trajectory reveals more information about the internal mechanics of the complex molecules [63], the mechanism of the covalent bond breaking [60], or tip-adsorbate forces [64].

Chapter 3

Fullerenes and endohedral metallofullerenes

Fullerenes are next to graphite and diamond the third allotrope of carbon. Their discovery by Kroto and Smalley in 1985 [65], awarded a Nobel Prize in 1996, introduced into science a new class of solely carbon-based nanostructures. The family of carbon structures has been then soon enlarged by the carbon nanotubes [66] and recently also by graphene [67]. The fullerenes are sphere-like shaped carbon cages with a hollow core and typical diameter around 1 nm. A big breakthrough in the fullerene science was a development of a production method by Kraetschmer and Huffman [68]. The technique enabled the production of fullerenes in large quantities and since then the molecules became a basic 'building block' in nanoscience. The fullerene based compounds exhibit a number of fascinating properties [25], among them superconductivity [27] or ferromagnetism [26]. One of the interesting feature of the fullerenes is that they can encapsulate an atom or molecule into the hollow empty space within the cage. The endohedral doping alters the properties of the empty fullerenes creating a new class of the hybrid material, called endohedral fullerenes or metallofullerenes [30].

The purpose of this chapter is to discuss the main aspects of the physics of fullerenes and fullerene-based materials. The basic properties of the C_{60} molecule will be introduced, especially the geometry and electronic and vibrational structure. Subsequently, we will focus on the doped fullerenes and discuss the main features of the endohedral complexes, in particular the rare earth metallofullerenes.

3.1 Fullerene molecules

3.1.1 Basic properties of C_{60}

The most common and intensively studied molecule among the fullerenes is C_{60}. In the C_{60} molecule 60 equivalent carbon are located on the vertices of a truncated icosahedron. The cage consists of 20 hexagonal faces and 12 pentagonal faces, as shown in Fig. 3.1. Each pentagon is surrounded by five hexagons, consistent with the Euler's theorem and Isolated Pentagon Rule (IPR) [69], discussed in the next section (Section

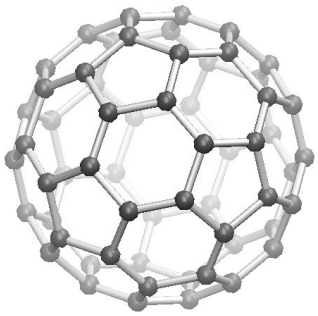

Figure 3.1: A schematic representation of the C_{60} molecule.

3.1.2). The icosahedral symmetry (I_h) of the C_{60} cage is one of the highest symmetries attainable in nature and comprises together 120 symmetry operations: identity operator, 6 fivefold axes (C_5) going through the centers of the pentagonal faces, 10 threefold axes (C_3) through the centers of hexagonal faces, 15 twofold axes (C_2) through the edges between the two hexagons and the composites of each these operations with the inversion operation.

Each of the carbon atoms is bonded to the neighbors in a predominately sp^2 bonding configuration. The pure sp^2 hybridization, however, has a planar geometry, as in the case of graphite. The curvature of the cage introduces a partial re-hybridization and leads to a deviation towards the sp^3 configuration, characteristic for the tetrahedral structure of diamond. The carbon bonds in C_{60} are not equivalent. The C-C bond between the hexagon and pentagon is usually referred to as a electron-poor single bond and has a length of 1.46 Å. The bond between two hexagons is shorter, 1.40 Å, and is addressed as a electron-rich double bond. The diameter of the cage is about 7.1 Å, which results in a total size of around 1 nm, when one includes the width of the π electron cloud around the molecule.

The four valence electrons of each carbon atom are involved in three bonding σ orbitals and one bonding π orbital. The energies of the σ orbitals are well below the Fermi level, and the electronic properties of the molecule are mostly determined by the π orbitals lying near the Fermi level. The electronic structure of the molecule, i.e. the ordering of the π energy levels, can be established based on the Hückel calculations, taking into account the high icosahedral symmetry of the cage [25, 70]. The results are shown in Fig. 3.2. The electronic structure of C_{60} is a closed shell structure, with a non-degenerate ground state. The highest occupied molecular orbital (HOMO) is fivefold-degenerate and has h_{1u} symmetry. The lowest unoccupied molecular orbital, of t_{1u} symmetry, is threefold-degenerate. The molecular local density approximation calculations for C_{60} yield a value of 1.92 eV for the HOMO-LUMO gap of the free molecule [25].

C_{60} can form a solid state, called fullerite, where all the molecules are arranged in the face-centered cubic lattice (fcc) with a lattice constant of $a_0 = 14.17$ Å. The molecules in the solid, bounded by the van der Waals forces, interact weakly with each

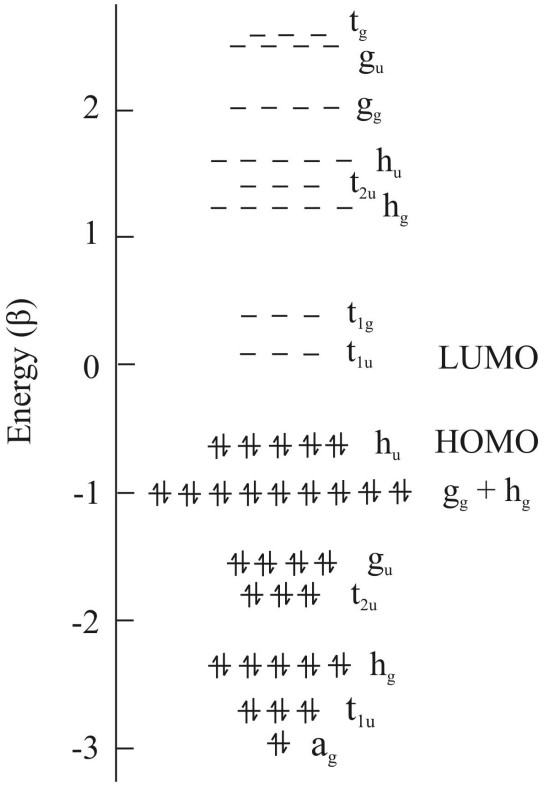

Figure 3.2: Diagram of the π-derived molecular levels of C_{60} by Hückel calculations, with the corresponding symmetries of the eigenstates [71]. The HOMO is five-fold degenerate and the LUMO is three-fold degenerate. (Adapted from Refs.[25, 70].)

other. The van der Waals distance between two C_{60} is $d_{C_{60}-C_{60}} = 10.02\,\text{Å}$. Due to the week coupling, the intermolecular vibrational modes of a C_{60} lattice have rather low frequencies. The intramolecular modes (the modes of the molecule itself), can be analyzed in terms of the symmetry representations of the I_h symmetry group [25]. The isolated C_{60} molecule has 174 vibrational degrees of freedom: $60 \times 3 = 180$ degrees of freedom in total reduced by six corresponding to rotation and translation. Due to the icosahedral symmetry of the cage most of the vibrational modes are highly degenerate and fall into 46 distinct mode frequencies. The intramolecular modes can be analyzed and classified according to their symmetry, using the group theory. The symmetries of the 46 modes are following:

$$\Gamma_{mol} = 2A_g + 3F_{1g} + 4F_{2g} + 6G_g + 8A_g + A_u + 4F_{1u} + 5F_{2u} + 6G_u + 7H_u. \qquad (3.1)$$

The symmetry labels A_g, H_g etc. correspond to the irreducible representations of the icosahedral (I_h) symmetry group [71]. The subscripts g (gerade - even) and u (ungerade - odd) indicate symmetry and antisymmetry with respect to inversion. From group theory it follows that 10 of the modes are Raman active (A_g and H_g), 4 are infrared (IR) active (F_{1u}) and the remaining 32 are optically silent. All the vibrational

modes of C_{60}, their symmetries and energies are listed in Table 3.1. The frequencies of the C_{60} modes lie between around $250\,cm^{-1}$ and $1600\,cm^{-1}$, what corresponds to energies between 30 meV and 200 meV. The general tendency is that the lower-frequency vibrations involve predominately radial displacement of the atoms, whereas higher-frequency modes are mostly tangential ones.

Even parity					Odd parity				
	Frequency (cm^{-1})					Frequency (cm^{-1})			
ω_i	Expt.	Th.1	Th.2	Th.3	ω_i	Expt.	Th.1	Th.2	Th.3
$\omega_1(A_g)$	497.5	492	478	483	$\omega_1(A_u)$	1143.0	1142	850	1012
$\omega_2(A_g)$	1470.0	1468	1499	1470					
					$\omega_1(F_{1u})$	526.5	505	547	547
$\omega_1(F_{1g})$	502.0	501	580	584	$\omega_2(F_{1u})$	575.8	589	570	578
$\omega_2(F_{1g})$	975.5	981	788	879	$\omega_3(F_{1u})$	1182.9	1208	1176	1208
$\omega_3(F_{1g})$	1357.5	1346	1252	1297	$\omega_4(F_{1u})$	1429.2	1450	1461	1445
$\omega_1(F_{2g})$	566.5	541	547	573	$\omega_1(F_{2u})$	355.5	367	342	377
$\omega_2(F_{2g})$	865.0	847	610	888	$\omega_2(F_{2u})$	680.0	677	738	705
$\omega_3(F_{2g})$	914.0	931	770	957	$\omega_3(F_{2u})$	1026.0	1025	962	1014
$\omega_4(F_{2g})$	1360.0	1351	1316	1433	$\omega_4(F_{2u})$	1201.0	1212	1185	1274
					$\omega_5(F_{2u})$	1576.5	1575	1539	1564
$\omega_1(G_g)$	486.0	498	486	449					
$\omega_2(G_g)$	621.0	626	571	612	$\omega_1(G_u)$	399.5	385	356	346
$\omega_3(G_g)$	806.0	805	759	840	$\omega_2(G_u)$	760.0	789	683	829
$\omega_4(G_g)$	1075.5	1056	1087	1153	$\omega_3(G_u)$	924.0	929	742	931
$\omega_5(G_g)$	1356.0	1375	1296	1396	$\omega_4(G_u)$	970.0	961	957	994
$\omega_6(G_g)$	1524.5	1521	1505	1534	$\omega_5(G_u)$	1310.0	1327	1298	1425
					$\omega_6(G_u)$	1446.0	1413	1440	1451
$\omega_1(H_g)$	273.0	269	258	268					
$\omega_2(H_g)$	432.5	439	439	438	$\omega_1(H_u)$	342.5	361	404	387
$\omega_3(H_g)$	711.0	708	727	692	$\omega_2(H_u)$	563.0	543	539	521
$\omega_4(H_g)$	775.0	788	767	782	$\omega_3(H_u)$	696.0	700	657	667
$\omega_5(H_g)$	1101.0	1102	1093	1094	$\omega_4(H_u)$	801.0	801	737	814
$\omega_6(H_g)$	1251.0	1217	1244	1226	$\omega_5(H_u)$	1117.0	1129	1205	1141
$\omega_7(H_g)$	1426.5	1401	1443	1431	$\omega_6(H_u)$	1385.0	1385	1320	1358
$\omega_8(H_g)$	1577.5	1575	1575	1568	$\omega_7(H_u)$	1559.0	1552	1565	1558

Table 3.1: Frequencies of intramolecular vibrational modes a C_{60}. The experimental mode frequencies are derived from the first and second order Raman [72] and IR [73] spectra. The calculated values presented in columns *Th.1*, *Th.2* and *Th.3* are taken from [74], [75] and [76] respectively. (Adapted from [25].)

3.1.2 Structure of higher fullerenes

Apart from C_{60}, also other fullerenes with higher masses, up to C_{116}, have been isolated. The properties of the higher fullerenes are usually more complex due to the lower molecular symmetry. Some of them highly deviate from the spherical shape. The basic structural rules common for the whole fullerene family may be concluded from the Euler's theorem. Euler's theorem establishes following general relation for the polyhedron

$$f + v = e + 2, \tag{3.2}$$

where f, v and e are the number of faces, vertices and edges, respectively. For a fullerene, which is a polyhedron formed from only hexagonal and pentagonal faces, follows that number of pentagons in the cage must be equal to twelve. The twelve pentagonal faces form the curvature of the cage and each new fullerene is formed by adding a hexagonal face. Since each hexagon adds two carbon atoms to the cage, there total number of carbon atoms accounting for the fullerene must be even. Each of the 12 pentagons tends to get isolated by the hexagons [69]. Such situation is energetically favorable for a fullerene, since it reduces the local curvature and minimizes the strain. This empirical rule is called Isolated Pentagon Rule (IPR). C_{60} is the smallest fullerene that satisfies the IPR. The next one is C_{70}, which also agrees with the fact that no fullerenes between C_{60} and C_{70} are found during the production. For the fullerenes higher than C_{70} different geometrical structures obeying the IPR are possible and consequently different stable isomers of the cage exist [77].

3.2 Endohedral doping of fullerenes

One of the interesting features of the fullerenes is that their properties may be tuned by doping. Doped fullerenes are usually charge transfer compounds i.e. the dopant atoms donate some or all of their valence electrons to the empty molecular orbitals of the cage. In principle, there are three different ways of doping: exohedral, substitutional and endohedral. The classification is based on the position of the dopant with respect to the cage, as illustrated in Fig. 3.3.

The most common doped compounds are the exohedrally doped fullerenes. In exohedral species the doping atoms or molecules stay outside the fullerene cage or in between them. This method is usually applied to C_{60} solids, where the dopants are introduced onto the C_{60} crystalline phase and fill the interstitial voids. The intercalation compounds, called fullerides, are normally prepared with alkali or alkali-earth metals. The metal atoms partly or completely donate their outer electrons to the C_{60} molecules, which can substantially alter the fullerite properties. Among the known fascinating properties of different intercalation compounds are metallic conductivity [78], superconductivity [27], ferromagnetism [26] or polymer formation [28].

In the substitutional doping, one of the carbon atoms on the cage is replaced with an atom of different valence state. Since the carbon atom is very small, the only known substitutional dopants are boron and nitrogen, forming the heterofullerenes B_nC_{60-n}

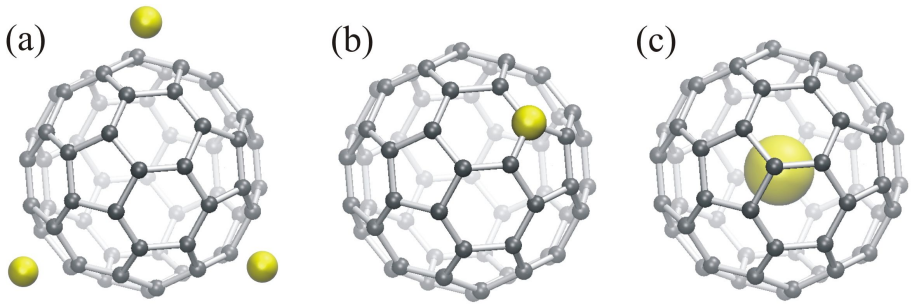

Figure 3.3: Possible ways of doping fullerenes: (a) exohedral doping, (b) substitutional doping, (c) endohedral doping.

and N_nC_{60-n}.

The endohedrally doped fullerenes are formed by introducing a dopant into the empty hollow space inside the cage. The first report on the possible encapsulation of the atom inside a fullerene appeared soon after the discovery of C_{60}. Kroto *et al.* found in the mass spectrum a feature corresponding to the LaC_{60} and proposed the endohedral nature of the molecule, i.e. La atom trapped in the ball-like shaped C_{60}[79]. However, the evidence for the atom encapsulation were not convincing, until the first structural characterization of $Y@C_{82}$ by XRD (x-ray diffraction) measurements in 1995 [80]. The electron density distribution map of the molecule, derived from the x-ray results by combined Retvield and maximum entropy method (MEM) analysis [81], revealed the high electron density inside the cage and finally confirmed its endohedral structure.

So far, a huge number of species have been encapsulated in the carbon cages. Elements experimentally trapped inside the fullerenes are listed in Fig. 3.4. Fullerenes can encapsulate various metal atoms, among them rare earth, alkaline earth and alkali metals. Compounds formed by incorporation of small clusters have also been reported [82]. Surprisingly, the most stable endohedral complexes are based on cages higher than C_{60}. The first C_{60}-based endohedral compounds have been isolated relatively late, due to their low stability in air and solution [30]. Among the interesting elements reported to be captured in C_{60} are e.g. the rare-gas atoms [83], but the most intriguing representatives of this class are perhaps $N@C_{60}$ and $P@C_{60}$. The encaged nitrogen and phosphorus atoms are well isolated from the surrounding environment, $N@C_{60}$ is also the only compound where highly reactive nitrogen occupies its ground state [84]. The unique spin properties of these fullerenes, e.g. long electron spin lifetimes, account for their possible application as qubits in quantum computing [34, 35].

The endohedral complexes studied in this work, $Ce@C_{82}$ and $Ce_2@C_{80}$, are representatives of the lanthanide fullerenes. The particular properties of $M@C_{82}-$ and $M_2@C_{80}-$type molecules (M denoting a metal atom), are summarized in Section 3.4.

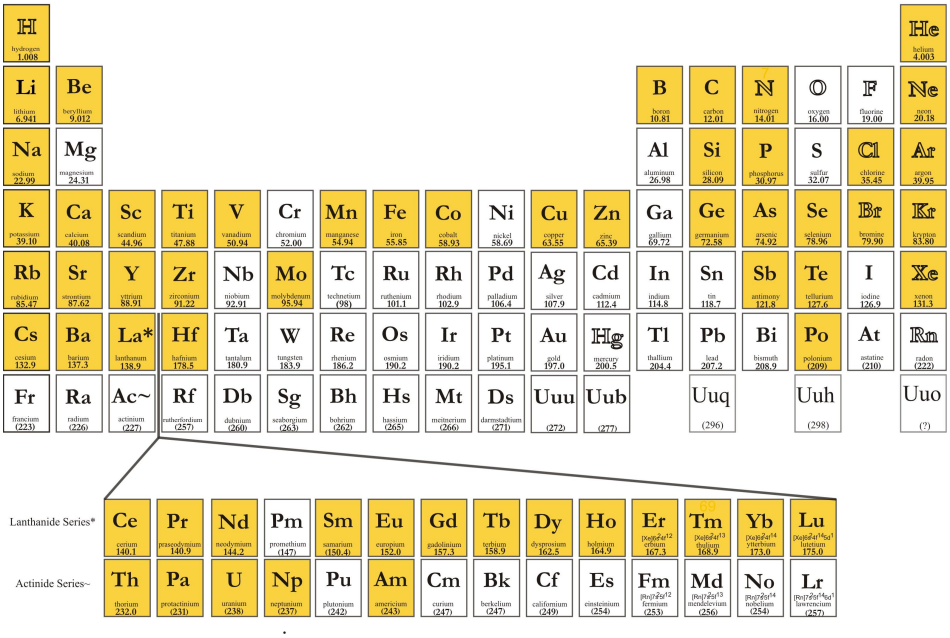

Figure 3.4: 'Periodic table' of elements captured in various carbon cages. The atoms experimentally reported to form endohedral fullerenes are colored. (Based mainly on [25, 30])

3.3 Production and purification of fullerenes

A standard way of synthesizing the fullerenes and metallufullerenes is a DC arc-discharge method. The method, first introduced in 1990 by Kraetschmer and Huffman [68], allowed the first production of fullerenes in macroscopic amounts. The main products of the fullerene synthesis are C_{60} and C_{70}, all other hollow fullerenes, as well as metallofullerenes, are produced in significantly smaller quantities (usually lower than 0.5%). Therefore, to obtain pure metallofullerene sample, the synthesis must be followed by extraction and purification stages. The fulllerene isolation procedure is in detail described in Refs. [25, 30].

The first isolation of a metallofullerene was accomplished by the Rice group, who in 1991 extracted the La@C_{82} [85]. Soon, purification of other species was reported, including the extraction of Ce@C_{82} and Ce_2@C_{80} metallofullerenes [86, 87, 88].

Fullerene synthesis

The DC arc discharge method involves the generation of carbon-rich vapor or plasma in He atmosphere [25, 30]. During the cooling process the fullerenes and metallofullerenes are formed by the collisions of carbon and helium atoms. The arc discharge generator consists of the production chamber and collection chamber. The crucial elements are the discharge electrodes. For the production of hollow fullerenes graphite

rods are used, to synthesize metallofullerenes one of the graphite rods is substituted by metal-oxide or metal-carbide composite. The discharge between the rods generates the carbon-rich vapor or plasma and metal carbides essential for the synthesis of metallofullerenes. The produced soot is collected in the collection chamber under anaerobic conditions.

Extraction and purification of metallofullerenes

The soot obtained in the synthesis process contains, apart from fullerenes, various impurity molecules. The most common method of separating the fullerenes from the raw soot is the solvent extraction. The efficiency of the solvation method depends on the solubility of the particular fullerenes. Usually, for hollow fullerenes toluen and carbon-disulfide CS_2 are used. For separation of metallofullerenes pyridine and 1,2,4-trichlorobenzene are more efficient. However, in this stage also other soluble impurities are extracted together with fullerenes. Therefore, the preparation of the highly pure samples requires futher chemical purification.

The main method used for the purification of metallofullerenes is the High Performance Liquid Chromatography (HPLC), a technique widely employed in wet-chemistry [89]. It allows the separation of the fullerenes according to their molecular weights, shape, size and other parameters [90]. A solution containing a mixture of the molecules (called the 'mobile phase') is forced through a column containing solid particles (called 'stationary phase'). The separation of the molecules occurs in the column: substances that interact weakly with the stationary phase pass rapidly through the column, whereas those which are adsorbed strongly by the stationary phase emerge after a relatively long time. A detector attached to the outlet of the column can be used to measure the concentration of the various components. The graph of detector output against retention time is known as a chromatogram. The identity of the separated fraction is verified by the mass spectrometry.

3.4 Structure and properties of rare earth metallofullerenes

The fullerene species doped with the rare earth atoms belong to the most stable endohedral compounds isolated so far. Almost all the atoms of the lanthanide series have been reported to form the endohedral species, most commonly in the form $M@C_{82}$, where one metal atom (denoted by M) is encapsulated in a C_{82} cage. To this class belongs also the first isolated metallofullerene, $La@C_{82}$ [85]. Another stable complex is $M_2@C_{80}$ formed by incorporating two metal atoms into C_{80} cage. In this section the main properties of the rare earth metallofullerenes based on the C_{82} and C_{80} cages are discussed.

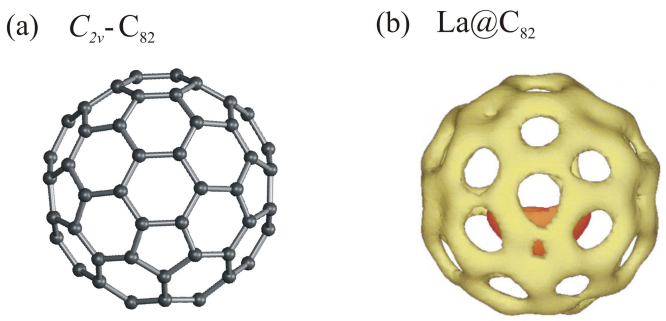

Figure 3.5: Structure of the M@C_{82}-type metallofullerenes. (a) Schematic picture of a C_{2v} isomer of C_{82}. C_{2v} cage structure is the most stable structure upon doping with following lanthanide atoms: (b) The equal-density contour surface of the charge density of La@C_{82} (obtained by MEM/Retvield analysis of x-ray diffraction data). La atom occupies an off-center position inside the cage [94].

3.4.1 Geometry of metallofullerenes

As already mentioned in Section 3.1.2, the hollow fullerenes higher than C_{70} exist in different isomers, i.e. there is more than one cage structure consistent with isolated pentagon rule. In case of the endohedral doping the stability and symmetry of the cage depends on the properties of encapsulated species, mostly on the amount of charge transfer. As a consequence, the isomer favored upon incorporation of an atom is usually different than the stable isomer of a hollow cage.

The C_{82} cage consists of 12 pentagonal faces and 31 hexagonal faces. Altogether nine different isomer structure satisfying the IPR-rule are present [77]: C_2(a), C_2(b), C_2(c), C_{2v}, C_s(a), C_s(b), C_s(c), C_{3v}(a) and $C_{3v}(b)$, the C_2 isomer being the most stable structure of the hollow cage. Recent theoretical calculations have shown that the most stable isomer upon encapsulation of one Ce atom is the C_{2v} [91]. The same symmetry is favored also for other rare-earth atoms, e.g. La, Pr, Gd and Dy. The schematic drawing of the C_{2v} isomer is shown in Fig. 3.5(a). The experimental results for Ce@C_{82} reveal also the presence of second stable isomers, C_s [92, 93]. The position of the encapsulated atom inside the C_{82} cage has been experimentally determined x-ray diffraction measurements and maximum entropy method MEM/Retvield analysis [80, 94]. The MEM electron density distribution for La@C_{82} molecule is presented in Fig. 3.5(b) [94]. The results clearly show that the trapped atom does not stay in the center but prefers a position close to the interior wall of the cage. Similar conclusions follow from the *ab-initio* modelling, revealing a specific bonding site of the metal atom inside the C_{82} [91, 95].

In case of C_{80}, its 12 pentagonal and 30 hexagonal faces of can be arranged in seven different structure consistent with the IPR-rule [77]. From the possible isomers: D_2, D_{5d}, C_{2v}, C'_{2v}, D_3, D_{5h} and I_h, the most stable structure of the hollow cage is D_2.

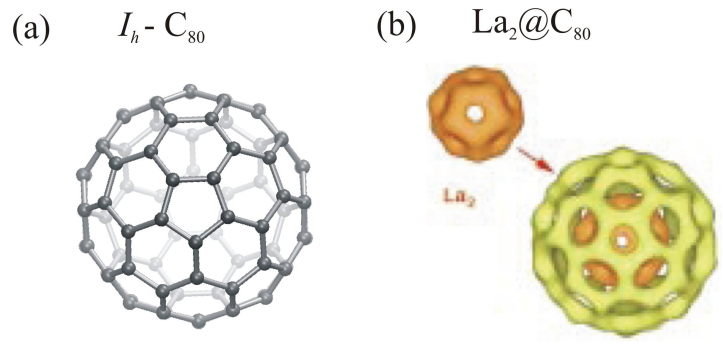

Figure 3.6: Structure of the $M_2@C_{80}$-type metallofullerenes. (a) Schematic drawing of a I_h isomer of C_{80}. I_h-C_{80} cage structure is stabilized by doping with two metal atoms. (b) The equal-density contour surface of MEM charge density of $La_2@C_{80}$. At room temperature two La atoms hop along the hexagonal rings of the I_h cage, forming a pentagonal dodecahedral. [97]

The encapsulation of two metal atoms stabilizes the otherwise unfavorable I_h isomer. The I_h-C_{80} was calculated to be the most stable structure upon doping with La, Ce and Pr atoms [96]. The MEM/Retvield analysis confirms the icosahedral symmetry of the $La_2@C_{80}$ fullerene and reveals pentagonal-dodecahedral distribution of the charge density of La atoms, indicating that at room temperature the two La atoms hop along the hexagonal rings of the I_h-C_{80} network [97]. The schematic structure of the I_h-C_{80} cage and MEM electron density distribution of $La_2@C_{80}$ are presented in Fig. 3.6.

3.4.2 Electronic properties

One of the key parameters that determine the electronic structure of the metallofullerenes is the amount of charge donated from the metal atom to the carbon cage. Theoretical calculations show that the electrostatic potential inside the carbon cage becomes highly negative when the fullerene accepts additional electrons [98]. Therefore a negatively charged cage is very suitable for accommodation of the cationic species and encapsulated atoms prefer a highly cationic state, instead of preserving a neutral state. The valence state of the lanthanide elements has been determined experimentally by ESR (Electron Spin Resonance), XPS (X-ray Photoemission Spectroscopy) and x-ray diffraction. The results for $M@C_{82}$ suggest a 3+ charge state of encapsulated atom when M = La, Ce, Pr, Nd, Gd, Tb, Dy, Ho, Er, and Lu [30, 93, 99, 100, 101, 102]. The charge state of Sm, Eu, Tm and Yb has been found to be 2+ [30, 99, 103].

The electron configuration of La, the first atom of the lanthanide series, is [Xe] $6s^2$ $5d^1$. The next elements start to fill the f-shell, giving the configuration of Ce: [Xe] $6s^2$ $5d^1$ $4f^1$. Upon encapsulation in the fullerene cage, three valence electrons of Ce (s and d) are donated to the carbon cage. The f electron does not participate in the atom-cage bonding. The structures of Ce endohedral complexes are therefore often referred to as $Ce^{3+}@C_{82}^{3-}$ and $(Ce^{3+})_2@C_{80}^{6-}$. Based only on the charge transfer consideration a basic

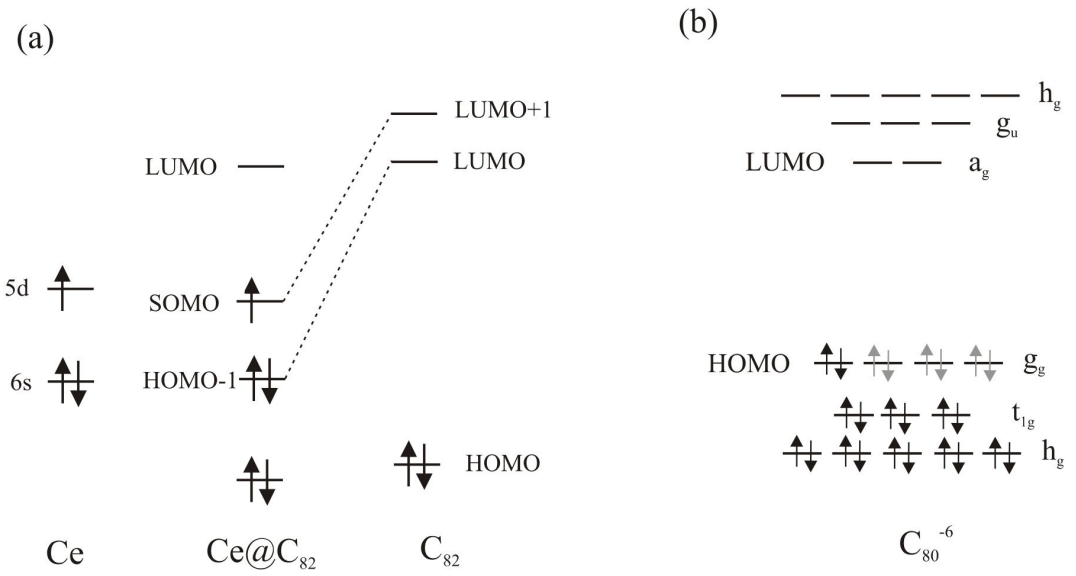

Figure 3.7: Simplified model of the electronic structure of $Ce@C_{82}$ and $Ce_2@C_{80}$ metallofullerenes based on the charge transfer consideration. (a) Energy levels of $Ce@C_{82}$ molecule. Three valence electrons of Ce are transferred to the C_{82} cage. The electronic structure of the formed complex exhibits a singly occupied molecular orbital (SOMO). (b) Molecular orbital levels of $C_{80}{}^{-6}$, a simplified model of C_{80}. h_g, g_u, etc.. denote the symmetries of the states [71]. The four-fold degenerate HOMO is occupied by the six electrons donated from the Ce atoms (indicated by grey arrows).

model of the electronic structure of $Ce@C_{82}$ and $Ce_2@C_{80}$ molecules can be derived. A simplified diagram of the orbital energy levels of $Ce@C_{82}$ molecule is presented in Fig. 3.7(a). The three electrons that take part in the charge transfer occupy the LUMO and LUMO+1 levels of the C_{82}. The HOMO level of the formed metallofullerene is only partially occupied and gives rise to a singly occupied molecular orbital (SOMO). Similar simplified model can be established for the $Ce_2@C_{80}$ molecule. The schematic electronic structure of this molecule is shown in Fig. 3.7(b). The I_h isomer of a hollow C_{80} is unstable, having a four-fold degenerate HOMO occupied only by two electrons. The transfer of the additional six electrons from the two Ce atoms stabilizes the I_h-C_{80} by complete filling of the HOMO orbital [96]. The whole complex has a stable closed shell structure and exhibit a large HOMO-LUMO gap.

At the end it must be stressed that the description of the metal-cage interaction only by charge transfer is a simplified picture. The actual bonding is more complex and involves also hybridization of the dopant-fullerene orbitals. The photoemission studies indicate that the electronic states of the endohedral complex are partially localized on the encapsulated species [104]. Theoretical calculations of the electronic structure of metallofullerenes predict that the charge transferred to the cage is not delocalized but stays in the vicinity of the bonding site of the metal [91]. Also a considerable back-donation of the electrons from the cage into the $5d$ orbitals of metal atom takes place

[96, 91].

3.4.3 Vibrational modes

The vibrational structure of various metallofullerenes has been studied by different spectroscopic techniques, including Raman and infrared spectroscopy (IR). Of the great interest is the dynamics of the encapsulated species. The vibrational modes involving the movement of the encapsulated species are a fingerprint of the interaction between the fullerene cage and the metal atom. Based on the modes frequencies, the experimental value of the metal-cage bond strength can be determined [105, 106]. It has been established, that the mode frequencies, and therefore also the bonding strength, are highly influenced by the amount of charge transfer from the dopant (the trivalent metal atoms bind stronger than the divalent ones), but only minor effect of the cage isomer has been observed [107].

The IR and Raman measurements for various M@C_{82} fullerenes show almost identical pattern for the frequencies between 200 cm^{-1} and 1600 cm^{-1}, what indicates that in this spectral range the internal vibrational modes of the cage are observed [105, 108]. Below 200 cm^{-1} two different vibrational bands have been detected, arising from the coupling of the motion of the metal atom and the fullerene cage. The higher band, with the frequencies 161 cm^{-1} for La@C_{82} and 160 cm^{-1} for Ce@C_{82}, can be assigned to the distinct metal-cage stretching mode. The lowest band, resolved by Raman spectroscopy at 45-50 cm^{-1} for La@C_{82}, is described as metal-cage deformation mode, where the metal atom moves parallel to the cage [105]. The experimental values of the metal-cage vibrational frequencies for different metallofullerenes are listed in Table 3.2.

Metallofullerene	Raman frequencies (cm^{-1})	IR frequencies (cm^{-1})
La@C_{82}	163	45-50, 161
Ce@C_{82}	162	160
Pr@C_{82}	168	not studied
Gd@C_{82}	155	not studied
Dy@C_{82}	140	not studied
Tm@C_{82}	118, 42	not studied

Table 3.2: Frequencies of the metal-cage vibration in M@C_{82}metallofullerenes measured by Raman and IR spectroscopies. The values are taken from Refs. [93, 105, 107, 109, 110]

.

The vibrational modes of M_2@C_{80} can be analyzed in terms of the symmetry representations. The I_h isomer of the C_{80} cage has altogether 62 different mode frequencies that group into following symmetries: $3A_g + 4F_{1g} + 5F_{2g} + 8G_g + 11H_g + 1A_u + 64F_{1u} + 7F_{2u} + 8G_u + 9H_u$. Upon the encapsulation of the atoms the symmetry of the whole molecule is reduced into D_{3d}, D_{2h} or C_2 which leads to the splitting of the cage vibrational modes into lower symmetries. According to Raman and IR studies,

the frequencies of the internal cage vibrations lay above 200 cm^{-1}, as in case of C_{82} [106, 111]. The Raman spectrum of $La_2@C_{80}$ resolves a low frequency vibration at 161 cm^{-1} [112]. Based on calculations, this peak is assigned to the A_{1g} mode that elongates the C_{80} cage and has a strong contribution from La atoms. Moriyama *et. al* calculated also two IR-active vibrational modes at 66 cm^{-1} and 72 cm^{-1}, corresponding to the vibrations of the La-La unit in directions perpendicular to the La-locating axis [111]. For $Ce_2@C_{80}$ no spectroscopic measurements are available so far. However, the low frequency modes involving the dopant movement are supposed to follow the mass scaling law. For the species of the same ionization state, the wave numbers of the modes are inversely proportional to the square root of the mass of the metal atom [105, 108]. Therefore, the frequencies expected for the modes of $Ce_2@C_{80}$ should be close to the frequencies already measured for $La_2@C_{80}$.

Chapter 4

Experimental

4.1 Synthesis and purification of cerium metallofullerenes

The cerium doped endohedral fullerenes used in this work were produced by the group of H. Shinohara at Nagoya University in Japan [113]. For the synthesis of the fullerenes the contact arc technique, as described in Section 3.3, was used. The composition of the metal/graphite composite rods was optimized to obtain the high production yields of the Ce-containing fullerenes and thus the 0.8 wt-% Ce/graphite rod was used as anode and pure graphite rod as cathode. The soot containing metallofullerenes, hollow fullerenes and amorphous carbons was collected under anaerobic conditions. The fullerenes were then solvent-extracted. A two stage extraction method was employed: first o-xylen was used to extract the hollow and endohedral fullerenes from the soot, subsequently the *N,N*'-dimethylformadine (DMF) was used to separate the metallofullerenes from the fullerene mixture.

The purification stage was accomplished in the group of T. J. Dennis *et al.* at the Queen Mary University of London in United Kingdom. The metallofullerenes-enriched solution was injected into the preparative recycling HPLC system (Japan Analytical Industry LC-908-C60) with a Nacalai Tesque Cosmosil 5PYE column. Mono- and dimetallofullerenes were then separated using the HPLC technique. The species involved in the analyte were identified by the mass spectrometry. The matrix-assisted laser desorption ionization time of flight (MALDI-TOF) mass spectrometry was employed, a technique developed by Tanaka *et al.* [114] which is widely used to determine the molar masses of the macromolecules.

For the HPLC purification the DMF metallofullerene-enriched extracts were dissolved in toluen. Subsequently, the concentrated toluen solution of fullerenes was injected in the HPLC system using toluen as eluent. A single-pass HPLC chromatogram of the sample containing Ce-doped fullerenes is shown in Fig. 4.1(a). As seen in the graph, the retention times for some fullerenes are too close to be separated in the single-pass stage and therefore the recycling mode was employed. In the recycling stage the eluent is forced back through the column repeatedly so that the peak-to-peak sep-

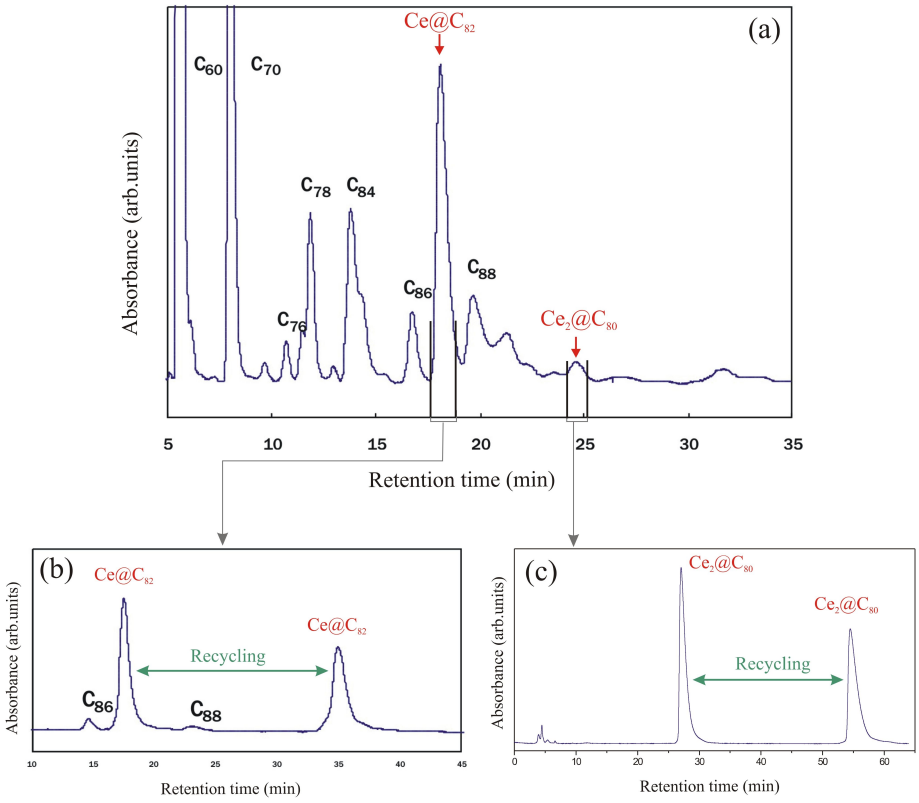

Figure 4.1: The HPLC chromatograms of the sample containing cerium-doped fullerenes. (a) A single pass HPLC profile, showing the identity of the species involved in each fraction. (b) HPLC profile of the recycling stage of the fraction containing $Ce@C_{82}$. The C_{86} and C_{88} peaks were removed after the first cycle. (c) HPLC chromatogram of the recycling mode isolation of $Ce_2@C_{80}$.

aration increases with the number of cycles through the column. The recycling HPLC profiles for the separation of $Ce@C_{82}$ and $Ce_2@C_{80}$ metallofullerenes are presented in Fig. 4.1(b) and (c). The recycling process was continued until pure metallofullerene fractions were obtained. The purity of the samples was then confirmed by the MALDI-TOF mass spectrometry. Spectra measured for $Ce@C_{82}$and $Ce_2@C_{80}$ are presented in Fig 4.2

4.2 Experimental set-up and sample preparation

All the measurements presented in this thesis have been preformed on a commercial low temperature STM operated at temperature $T = 7\,\mathrm{K}$. A detailed description of the apparatus can be found in Ref.[115]. The system consists of two ultra-high vacuum (UHV) chambers: preparation chamber and STM chamber, with the base pressure $p < 8 \times 10^{-11}$ mbar. The beetle-type STM is mounted on the bottom of the cryostat

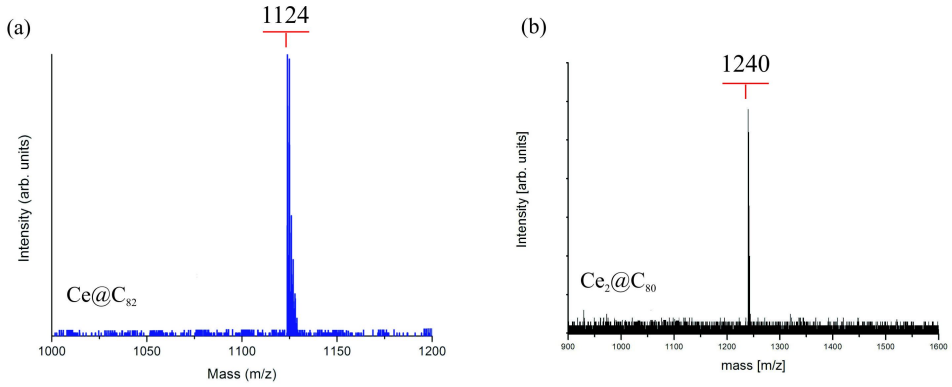

Figure 4.2: The MALDI-TOF mass spectra of purified $Ce@C_{82}$ and $Ce_2@C_{80}$ samples. The peaks corresponding to $Ce@C_{82}$and $Ce_2@C_{80}$endohedral fullerene are resolved in the spectra at 1124 amu and 1240 amu resoectively.

and is cooled to the temperature $T = 7\,\mathrm{K}$ by liquid helium. The apparatus is equipped with standard UHV preparation tools: sputter ion-gun, Knudsen-cell evaporators and quartz crystal balance.

For the experiments described in this thesis the Cu(111), Ag(100) and Au(111) metal single crystals have been used. The samples were cleaned under UHV conditions by sequential cycles of Ne^+ ion sputtering at 300K. One sputtering cycle typically lasted for 30 min. Subsequently the samples were annealed at the temperature 600°C for Cu(111), 550°C for Ag(100) and 550°C for Au(111). The usual time of the annealing step was 10 min.

Commercially available C_{60} molecules were thermally sublimed on the Cu(111) or Ag(100) surface from a Knudsen-cell evaporator. Prior to the deposition the material was thoroughly degassed at the temperature $\sim$ 480°C. During the deposition the Knudsen-cell was operating at $T = 420$°C and the evaporation rate was controlled by the quartz crystal balance. The metal sample were cooled to the temperature 77 K or 25 K, by liquid nitrogen or liquid helium, respectively.

Cerium metallofullerenes were stored in toluen solutions. The toluen was allowed to evaporate off at the ambient pressure before mounting the Knudsen-cell in the UHV system. $Ce@C_{82}$ molecules were degassed for 20 hours at $T = 200$°C and afterwards sublimed on a clean Cu(111) surface. The typical evaporation temperature was 500°C, the sample was kept at room temperature. The $Ce_2@C_{80}$ metallofullerenes were firstly degassed for 36 hours at 150°C and 12 hours at 270° and later evaporated on Cu(111) and Au(111) surfaces. Similarly as in the case of $Ce@C_{82}$, the deposition took place at room temperature, from the Knudsen-cell operating at 550°C. The procedure was followed by short annealing of the sample at 250°C.

After the preparation stage, the ready sample was transferred from the preparation chamber into the STM chamber and cooled down to the temperature 7 K.

The tips used in the experiments were prepared from the tungsten wire using the standard procedure of electrochemical etching in NaOH solution. Before installation in the STM, the tip was heated in order to remove the oxide layer.

The scanning tunneling spectra, i.e. dI/dV as a function of voltage V, were recorded with lock-in technique under the open feedback loop condition. A small AC modulation, V_{mod}, was added to the bias voltage. The tunneling current was fed into the lock-in amplifier and the output was recorded while the bias voltage was linearly ramped over a desired range. The typical amplitude and frequency used for the modulation signal were $V_{mod} = 10\,\mathrm{mV}$ (rms) and $f = 300 - 600$ Hz. The spectra were measure in a variable tip-sample separation mode, i.e. the tip-sample distance z was altered during ramping the voltage V in order to amplify the signal near the Fermi level [42]. The typically used separation contour was defined by

$$z(v) - z_0 = -a|V|, \tag{4.1}$$

where parameter a determines the slope of the ramp. The starting position z_0 was defined by the tunneling parameters before switching off the feedback. The usual maximal displacement in z during the spectroscopic measurements was $1 - 1.5\,\text{Å}$. The spectra measured by this procedure were subsequently normalized by the total conductance I/V (for details see Section 2.3).

The d^2I/dV^2 signal was recorded simultaneously with the dI/dV spectrum by using a separate lock-in amplifier. Again small bias modulation was applied but this time the amplitude of the in-phase modulation of the current was measured at the double frequency $2f$. The frequency of the voltage ac signal was carefully chosen, so that both f or $2f$ frequency occurred in the low noise region of the power spectrum of the tunneling current. Typical amplitude of the modulation signal was in the range of $V_{mod} = 3 - 6\,\mathrm{mV}$ (rms). During acquiring d^2I/dV^2 spectrum, the tip-sample distance was kept constant and the bias voltage was ramped. The detailed description of the inelastic tunneling spectroscopy can be found in Section 2.4.

The spectroscopic imaging was accomplished by recording the $dI/dV(x,y)|_V$ and $d^2I/dV^2(x,y)|_V$ signals by lock-in amplifiers, during slow acquisition of a constant current image. The feedback speed was chosen in a way that the the modulation frequency was above the bandwidth of the feedback.

Chapter 5

Electronic and vibrational properties of C_{60} molecule

The STM gives a unique opportunity to study the properties of the nanoobjects on the atomic scale. The bonding conformation of the molecules can be determined and their electronic and vibrational properties can be investigated with submolecular resolution. First reports on the STM imaging of C_{60} molecule were published soon after it became possible to produce the fullerenes in macroscopic amounts [116]. The early studies were focused on the structure of C_{60}monolayer or thin film on metal and semiconductor surfaces [117, 118]. Later, the development of the scanning tunneling spectroscopy and low temperature scanning probe techniques has enabled a detailed study of electronic and vibrational structure of C_{60} [119, 120, 121, 122, 123, 124, 125, 126].

This chapter summarizes the results of the study of C_{60} adsorbed on the Cu(111). The STM images of C_{60} resolve the intramolecular structure of the molecule and allow to determined the preferred orientation of the carbon cage on the substrate. It will be also shown that the chemisorption process affects the electronic structure of the molecules and the fingerprint of this interaction can be found in the STS spectrum. Also the vibrational structure of C_{60} will be discussed, based on the STM-IETS results. Futhermore, it will be demonstrated the single C_{60} molecules can be controllably manipulated by the STM and small artificial molecular structures can be assembled.

5.1 Electronic structure of Cu(111) surface

Most of the experiments described in this thesis have been performed on Cu(111) surface. Copper has a face-centered-cubic (fcc) crystal structure, with a unit-cell size of 3.61Å[127]. The (111) surface is a hexagonal closed-pack surface with a simple (1×1) reconstruction and interatomic distance equal to 2.55Å.

The electronic structure of Cu(111) exhibits a Shockley-type surface state, that appears at the Γ-point of the projected band structure [128]. Its existence is due to the breaking of the translational symmetry perpendicular to the surface [129]. The surface state electrons form a free two-dimensional (2D) electron gas with a parabolic

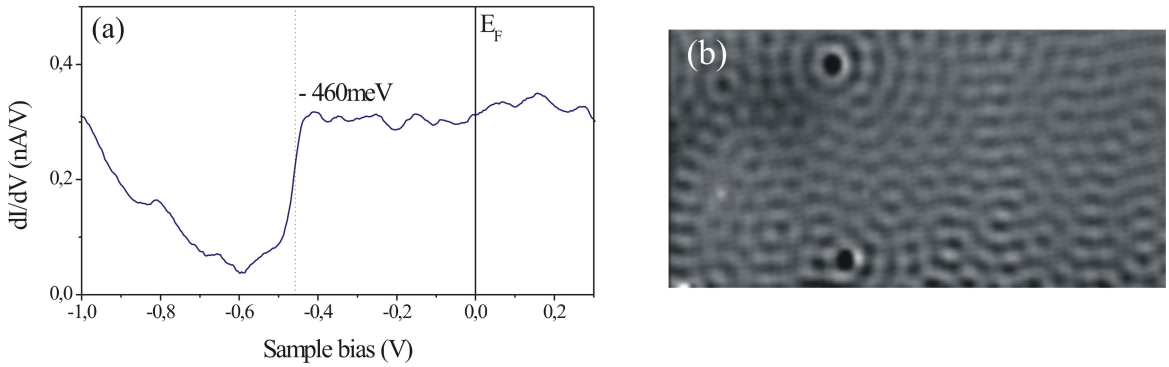

Figure 5.1: (a) STS spectrum taken on the clean Cu(111) terrace. The onset of the surface state is resolved as a clear step-like increase in the LDOS at the bias voltage -460mV. (b) Constant current STM image of the electron standing waves formed around the impurities (single CO molecules).

and isotropic dispersion. The energy momentum relation can be described as:

$$E(\overrightarrow{k}) = \frac{\hbar^2 \overrightarrow{k}^2}{2m^*} - E_{\overline{\Gamma}}, \tag{5.1}$$

with the effective electron mass $m^* = 0.38\, m_e$ and surface-state band edge energy lying below the Fermi level $E_{\overline{\Gamma}} = 440\,\text{meV}$ [130, 131].

The STM has been frequently used to investigate the noble metals surface states [130, 131, 132]. The onset of the surface-state can be detected by STS. On Cu(111) a step-like increase in the differential conductance can be observed at the energy corresponding to the surface band-edge, as presented in the Fig.5.1(a). The 2D electron gas is subjected to the scattering at surface imperfections such as steps and point defects leading to periodic spatial oscillations of the electronic local density of states. The resulting quantum interference patterns can be spatially resolved by STM [131]. The constant current image of the electron wave formed around the CO molecule is shown in Fig.5.1(b). The similar pattern is formed around the adsorbed fullerenes, indicating that the molecules serve as the scattering centers for the surface electrons.

5.2 Chemisorption of C_{60} on metal surfaces

Adsorption of the molecules on metal surfaces is a complex process that still requires deeper understanding. The exact nature of the bonding depends on the details of the species involved, but the simple classification distinguishes two different basic processes: chemisorption and physisorption [129].

Chemisorption is characterized by the creation of the chemical bond between the molecule and the metal surface. The interaction may have either complete ionic or

covalent character, but usually it involves both processes. The ionic bonding is accompanied by the charge transfer between the two species, whereas the covalent mechanisms is driven by the hybridization of the molecular orbitals and the metal bands [129, 133]. Chemisorption strongly affects the structure and properties of the adsorbate and leads to substantial rearrangement of the electron density.

In contrast, the physisorption process induces no significant redistribution of electron density in neither the molecule nor the substrate surface. A bonding is established due to the weak van der Waals forces, based on the interaction between the fluctuating dipole of the adsorbate and the induced dipole moment in the metal. The physisorption mechanism is typical for the rare gas atoms, whose exhibit a completely filled valence shell well below metallic Fermi level.

The adsorption of the fullerene molecules on metals is a chemisorption process, that involves, depending on the substrate, different amounts of charge transfer and hybridization of electronic states [134, 135]. The bonding between C_{60} and copper is believed to be predominately ionic, with only little degree of hybridization [136, 137]. Recent theoretical investigations predict that the Cu substrate donates charge to the fullerene, $0.8\,e^-$ in total [137]. Photoemission and photoabsorption studies of electronic structure of C_{60} on Cu(111) suggest charge transfer from the substrate to the carbon cage between 1.5-2 electrons per molecule [136]. In comparison, the amount of the charge transfer to single C_{60} determined by photoemission studies for other metal surfaces is $0.8\,e^-$ on Au(111) [138] and $0.73\,e^-$ on Ag(111) [139]. The results indicate strong interaction between C_{60} and Cu(111) surface, contrary to rather weak bonding on Au(111) and Ag(111).

5.3 Adsorption geometry on Cu(111)

In early STM studies of C_{60} on metal surfaces it was observed that growth of C_{60} monolayers at room temperature, followed by annealing, results in a formation of well-ordered (4x4) structure [117]. Deposition of the molecules at lower temperature ($T = 77\,\mathrm{K}$) limits the diffusion on the substrate and leads to nucleation of small islands on the terraces [140]. Decreasing the substrate temperature even more, down to $T = 25\,\mathrm{K}$, favors the adsorption of single molecules. Figure 5.2 shows the constant current STM images of C_{60} deposited on Cu(111) at different temperatures. The intramolecular structure of the fullerene molecules was clearly resolved for molecule adsorbed both in islands (Fig. 5.2(a)) and as single species (Fig. 5.2(b)). The empty states STM image of the island, presented in Fig. 5.3, shows C_{60} molecules as three-lobed or two-lobed protrusions. The dI/dV mapping of the electronic states of C_{60} indicates that the observed pattern is related to the pentagonal rings of the carbon cage [126, 141]. Based on this fact, the orientation of the cage with respect to the Cu(111) substrate can be easily established. The three-fold molecular symmetry indicates the C_{60} is adsorbed with a hexagon ring facing up, whereas the molecules that exhibit two-fold symmetry bind to Cu with a 6-6 bond (bond between the two hexagons). The schematic representations of the two configurations are shown in Fig. 5.3(b) and (c). The same two

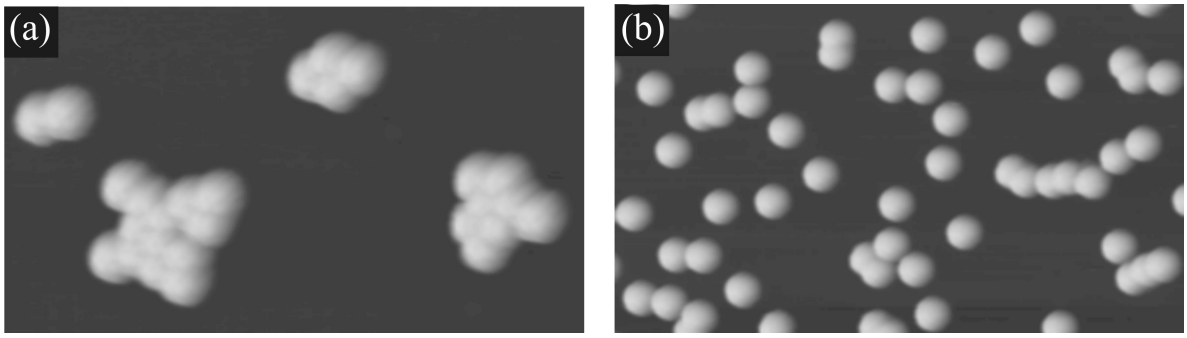

Figure 5.2: Constant current STM images of C_{60} on Cu(111). ($V = 1.5\,\mathrm{V}$, $I = 0.1\,\mathrm{nA}$) (a) STM image of C_{60} islands grown on the terrace of Cu(111) after deposition at $T = 77\,\mathrm{K}$ ($12 \times 20\,\mathrm{nm}^2$). (b) Single C_{60} species on Cu(111) can be obtained by lowering the deposition temperature to 25 K. ($20 \times 35\,\mathrm{nm}^2$)

characteristic adsorption geometries are favored also for single species, with predominance of three-fold symmetry. The three-fold symmetry has been also found for C_{60} monolayers and large two dimensional islands [117, 120]. The analysis of the STM images reveals that the molecules bounded with the hexagonal face parallel to the surface exhibit additionally two different azimuthal orientations, differing by 60°. The two azimuthal orientations are indicated in Fig. 5.4. These two bonding conformations, observed also for single C_{60} on Cu(111), and are extensively discussed in Ref. [142].

5.4 Influence of chemisorption on electronic structure

The photoemission studies of the electronic structure of C_{60} on different metal surfaces reveal that the molecular resonances lay in the range of several eV away from the Fermi level [136, 138, 143, 144]. Tsuei *et al.* in Ref. [136] measured the valence band spectra for C_{60} monolayers on Cu(111) and have resolved a peak corresponding to the HOMO orbital of the molecule at 1.7 eV binding energy. They report also observation of the small feature just below the Fermi level at -0.14 eV. A similar feature appears as well in valence band spectrum of C_{60} on Ag(111) [143] and is treated as a fingerprint of the charge donation from the underlying substrate.

The local density of states measured by STS for C_{60} on Cu(111) is shown in Fig. 5.5. Four main features are observed in the spectrum: a peak at -1.7 V (HOMO), small peak at -0.15 V (LUMO(I)), peaks at 0.55 V (LUMO(II)) and 1.8 V (LUMO+1). The assignment of the peaks to particular molecular resonances is based on the data from photoemission and inverse photoemission spectroscopy (PES and IEPS) [136, 144]. It is also in qualitative agreement with other STM studies on metal surfaces: Cu(111) [120, 142], Au(111) [124, 125], Ag(001) [141] and Ag(100) [126]. The origin of the feature resolved in the spectrum at $-0.7\,\mathrm{V}$ is not clear. A similar peak has been observed also

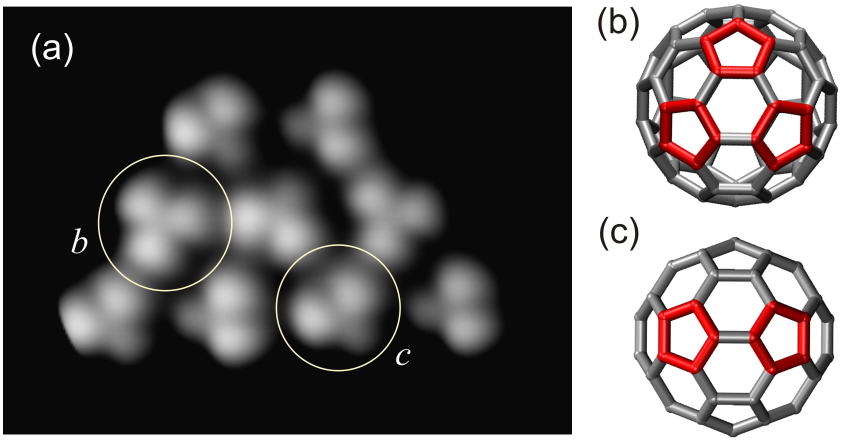

Figure 5.3: (a) Constant current STM image of a C_{60}island on Cu(111), with clearly resolved intermolecular structure. Molecules showing two different orientations are indicated by the circles. ($5\times7\,\mathrm{nm}^2$, $V = 0.1\,\mathrm{V}$, $I = 0.5\,\mathrm{nA}$) (b)-(c) Schematics of the two adsorption geometries (top view). Molecules adsorbed with 6-6 bond appear on the STM image as two-lobed protrusions (b). Molecules adsorbed with hexagon parallel to the surface appear as three-lobed protrusions (c).

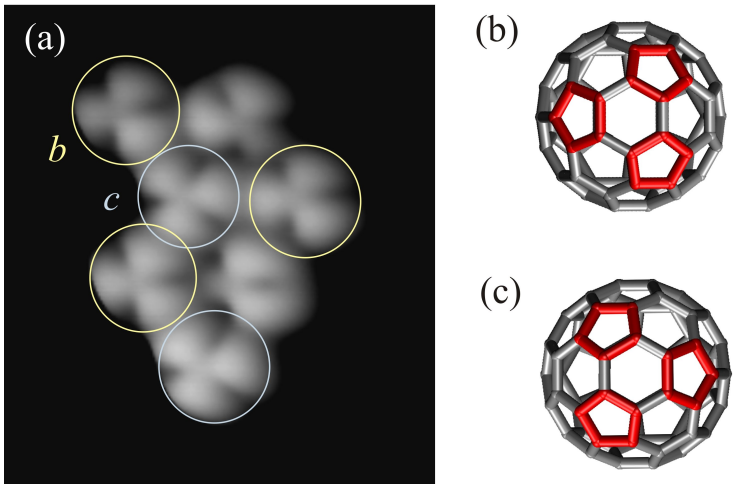

Figure 5.4: (a) STM image of a C_{60} island on Cu(111). Molecules adsorbed with hexagonal ring parallel to the surface show two azimuthal orientations, differing by 60°. (b) and (c) Schematic representations of the two azimuthal orientations indicated in the image. ($5\times4\,\mathrm{nm}^2$, $V = 0.1\,\mathrm{V}$, $I = 0.5\,\mathrm{nA}$)

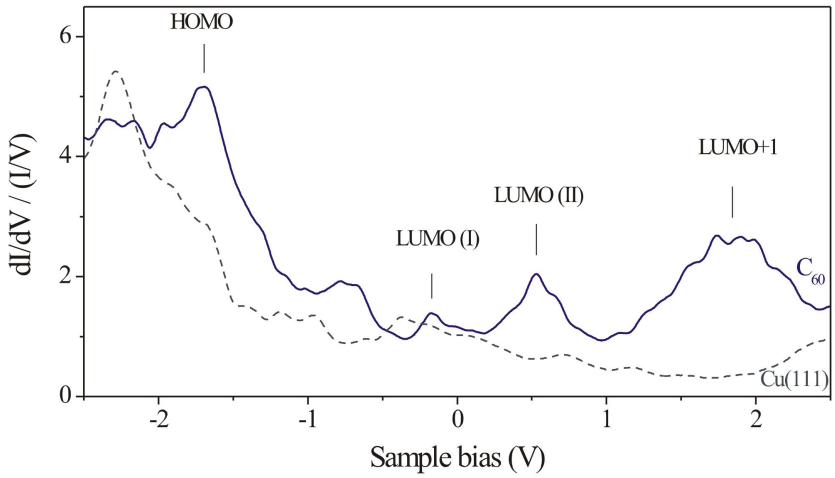

Figure 5.5: Normalized STS spectrum of a C_{60} molecule on Cu(111), measured for the molecule adsorbed with the hexagonal ring parallel to the substrate. The peaks in the spectrum correspond to the specific molecular orbitals (indicated in the figure). The grey spectrum was recorded on the bare Cu(111) surface. (Tunneling parameters: $I = 50\,\text{pA}$ and $V = 2.5\,\text{V}$, $V_{mod} = 10\,\text{meV}$ (rms))

on Au(111) [124], but so far it has not been determined whether it is related to the substrate or to the molecule. However, recent calculations of the electronic structure of C_{60} absorbed on Cu(111) suggest that the feature arises from the splitting of the HOMO orbital of a free molecule due to the interaction with the substrate [142].

The significant broadening of the molecular resonances, as well as the presence of a small LUMO-derived feature at -0.15 eV, are the indicators of a strong interaction between the C_{60} molecule and Cu(111) substrate. The observed splitting of the LUMO into two peaks LUMO(I) and LUMO(II) can be explained by the charge transfer from the substrate to the carbon cage. The additional charge is accumulated on the LUMO level, which, in result, splits into two states. One of them is partially filled (LUMO(I)) and therefore observed in the occupied part of the spectrum. Similar small LUMO-derived feature in the vicinity of Fermi level (E_F) was already observed by STS for C_{60} on Cu(111) [120] and Ag(100) [126, 141]. It appears also in the PES data for C_{60} on Cu(111) [136]. Interestingly, no such feature was reported for C_{60} on Au(111) [124, 125], in agreement with the fact that charge transfer between C_{60} and Au(111) is considerably smaller than in case of other metal surfaces (see Section 5.2).

The splitting of the LUMO level for C_{60} on Cu(111) has been confirmed also by the density functional theory (DFT) calculations for this system [142]. Chemisorption breaks the I_h symmetry of the molecule and lifts the degeneracy of the molecular orbitals. The interaction of the three-fold degenerate molecular LUMO of t_{1u} symmetry with the states of the Cu(111) gives rise to the filled e state in the vicinity of E_F.

The STS electronic spectra of C_{60} on Cu(111) did not show any systematic depen-

dence on the molecular orientation. However, it was observed that the position and intensity of the LUMO(I) peak varies from molecule to molecule. This suggests strong dependence of this feature on the local adsorption properties.

5.5 Vibrational spectroscopy

The vibrational structure of an isolated C_{60} molecule exhibits 46 different mode frequencies, listed in Table 3.1. The vibrational modes are highly degenerate, as already discussed in Section (3.1.1). Interaction with the substrate can shift the energies of the modes and lift the degeneracy. The electron energy loss spectroscopy (EELS) study of C_{60} on Cu(111) shows that the charge transfer from the substrate induces a softening of the vibrational modes [145]. The downward frequency shift on Cu(111), compared to the IR and Raman studies for the C_{60} mulitlayers, varies between $23\,cm^{-1}$ and $78\,cm^{-1}$, what corresponds to values $\sim 3 - 8$ meV.

The vibrational spectrum of C_{60} measured using the STM-IETS technique is presented in Fig. 5.6. The spectrum has been recorded over a two-lobed molecule adsorbed in a dimer on Cu(111). Two features in the plot can be attributed to the molecular vibrations: peak (and corresponding dip) at $\pm\,53\,(\pm 2)$ meV and peak (and dip) at $\pm\,138\,(\pm 3)$ meV. To assign these features to specific modes of the C_{60} cage, we have considered the vibrational structure of an isolated molecule, discussed in the section (3.1.1). Only one of the 46 intramolecular modes has energy close to observed 53 meV, therefore we attribute this vibration to $H_g(\omega_2)$ mode with energy 56 meV. Second of the peaks appearing in the spectrum, with energy 138 meV, can be most likely assigned to the $H_g(\omega_5)$ mode, which for an isolated molecule has energy 141 meV. The $H_g(\omega_2)$ mode corresponds to the 'gerade' breathing of the carbon cage and involves the displacement of the pentagonal rings of the molecule, along the C_5 symmetry axes, whereas the $H_g(\omega_5)$ is a tangential modes. Both modes are Raman active so their energies has been well established from the experiment [72, 146]. The observed shift of the modes towards the lower energies is an effect of the charge transfer and has been confirmed by the EELS studies [135, 145].

As already discussed in Section 2.4 the enhancement or lack of the signal from vibrations in STM-IETS is closely related to the coupling between tunneling electrons and vibrational states. The excitation of vibrational modes is then determined by the electronic structure around E_F. Previous STM-IETS study for C_{60} on Ag(110) suggested an active role of the LUMO-derived resonance in the vibrational excitation [122]. For LUMO state especially strong coupling to $H_g(\omega)$ and $A_g(\omega)$ vibrational modes is expected [119], what can explain why $H_g(\omega)$ modes occur in the spectrum. The inelastic tunneling spectrum on Ag(110) reveals the $H_g(\omega_2)$ mode at 53 meV, but the second mode observed on Cu(111) has not been resolved [122]. However, the character of molecular resonance at E_F is strongly affected by the charge transfer from the substrate, which is expected to be different on Ag(110) and Cu(111). This may give rise to the differences observed in IETS spectra. Interestingly, the $H_g(\omega_5)$ mode has been detected by STM for C_{60} adsorbed on Al_2O_3 film on NiAl(110) [119]. The increase in the number

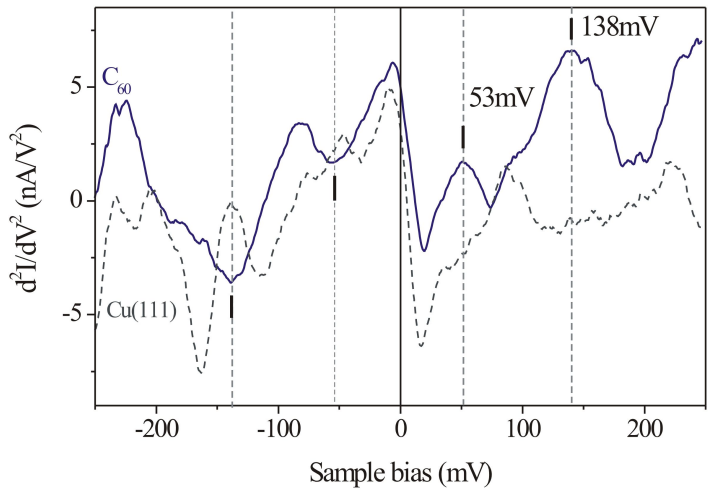

Figure 5.6: STM-IETS spectrum of a C_{60} molecule on Cu(111). The grey spectrum was measured on the bare Cu(111) surface. Ticks in the plot indicate the peaks corresponding to vibrational modes of C_{60}. The spectrum is an average of 50 d^2I/dV^2 curves. ($I = 0.1\,\mathrm{nA}$, $V = 250\,\mathrm{mV}$, $V_{ac} = 6\,\mathrm{mV}\,(\mathrm{rms})$)

of active modes in the study of Liu *at al.* is related to the decoupling of the molecular states from the underlying metal substrate due to the presence of the insulating layer. The extended lifetime of the transient negative ion allows to resolve the vibronic states, that are normally not detected by conventional STM-IETS on metals [121].

5.6 Lateral manipulation of single C_{60}

The lateral manipulation of C_{60} has been demonstrated for various surfaces [60, 147, 148, 149]. Cuberes *et al.* [147] reported the room temperature manipulation of C_{60} on Cu(111) substrate. The molecules could be repositioned along the Cu(111) step or detached from the step and placed into the Cu vacancies on the terrace.

The manipulation of the C_{60} at low temperature allows the controlled positioning of the molecule combined with the analysis of the manipulation mechanism. The experiments have been performed on the samples prepared by the low temperature deposition ($T = 25\,\mathrm{K}$) of C_{60} on Cu(111) or Ag(100) substrates, so that the molecules reside as single species on the surface terraces. The repositioning of the molecules was accomplished using the constant current lateral manipulation technique, described in Section 2.5.

Following feedback parameters have been used to move a C_{60} on Cu(111): I_{man}=20 nA and V_{man}=10 mV, so that the resistance of the tunnelling junction has been decreased to 0.5 MΩ. The example of the manipulation is shown in Fig. 5.7. During the manipulation process the plot of tip height versus the tip lateral position has been recorded. As explained in Section 2.5, the analysis of the characteristic tip trajectories can be

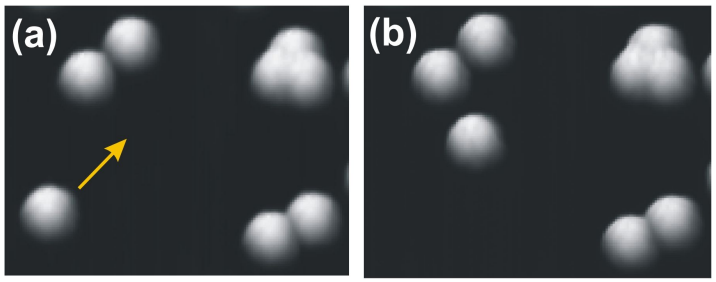

Figure 5.7: Single C_{60} manipulation on Cu(111). Displacement of the molecule is indicated by an arrow. Manipulation has been performed in constant current mode using feedback parameters $I_{man} = 20\,\text{nA}$ and $V_{man} = 10\,\text{mV}$.

used to gain more information about the involved manipulation mechanism. The tip height plots observed for C_{60} manipulated in two different directions on Cu(111) are shown in Fig. 5.8. From the shape of the curves it can be deduced that C_{60} has been pushed along the substrate via the repulsive interaction with the tip. Both plots exhibit a characteristic structure that reflects the periodicity of the Cu(111) surface. For the curve presented in Fig.5.8(a) the average distance between the single jumps is equal to 2.5 Å, which corresponds to the nearest neighbor distance on Cu(111) (a_0=2.55 Å). The shape of the plot and the hopping distance are typical for the manipulation of the species along the closed-pack rows of the (111) surface [62]. Therefore it seems likely that in this case the molecule has been moved along the [110] direction of the substrate (Fig. 5.8(c)). The tip trajectory shown in Fig.5.8(b) has been observed when the molecule has been manipulated along the line 30° away from the direction discussed in (a). From the assumption of the [110] direction in example (a) follows that in case (b) C_{60} has been moved along the [211] surface direction (shown in Fig.5.8(c)). The distance between two equivalent adsorption positions of Cu(111) along the [211] is ≈ 4.42 Å. This value is in good agreement with the average hopping distance for C_{60} in example (b), which is equal to 4.3 Å.

The lateral manipulation procedure discussed above has been used to assemble an artificial nanostructure from C_{60} molecules on Ag(100) substrate. The molecules have been deposited on Ag(100) at the $T = 25\,\text{K}$, in order to obtain single species on the surface. The controllable repositioning of C_{60} was possible using the feedback parameters $I = 20\,\text{nA}$ and $V = -30\,\text{mV}$, giving the resistance of the tunneling junction 1.5 MΩ. The process of building the structure NANO is shown in Fig.5.9. Each letter is $\approx 16\,\text{nm}$ high and has been assembled from single C_{60} molecules.

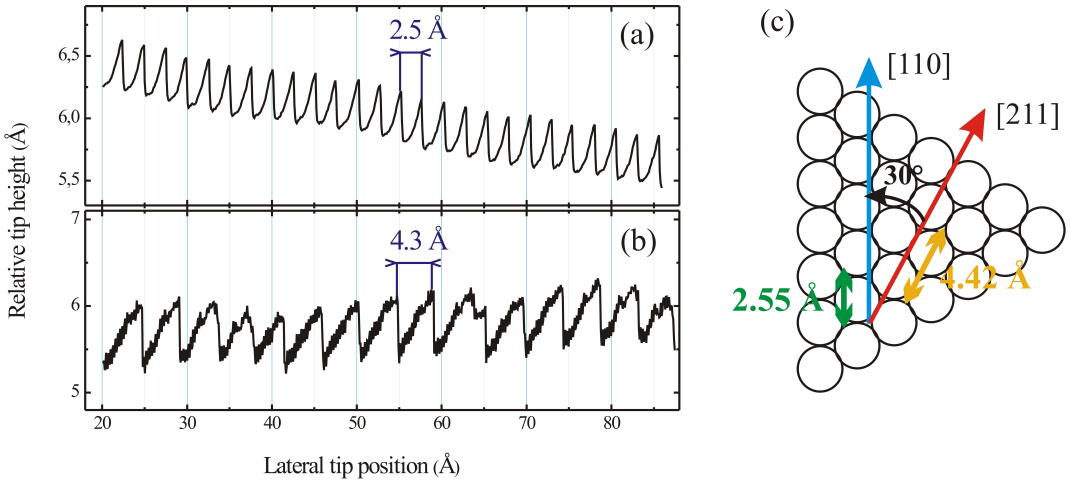

Figure 5.8: Traces of the tip height recorded during the manipulation of C_{60} on Cu(111). The characteristic shape of the curves indicates that the molecule has been manipulated in the pushing mode. (a) Tip height plot during repositioning the fullerene along the presumed [110] direction of Cu(111) substrate. The length of the single jump (2.5 Å) is equal to the nearest neighbor distance on Cu(111). (b) Tip trajectory during manipulation along the presumed [211] direction. The average hopping distance corresponds to the distance between to equivalent adsorption site along [211] direction. (c) The model of Cu(111) surface with represented crystal directions. The distances between equal adsorption sites along [110] and [211] are indicated in the image.

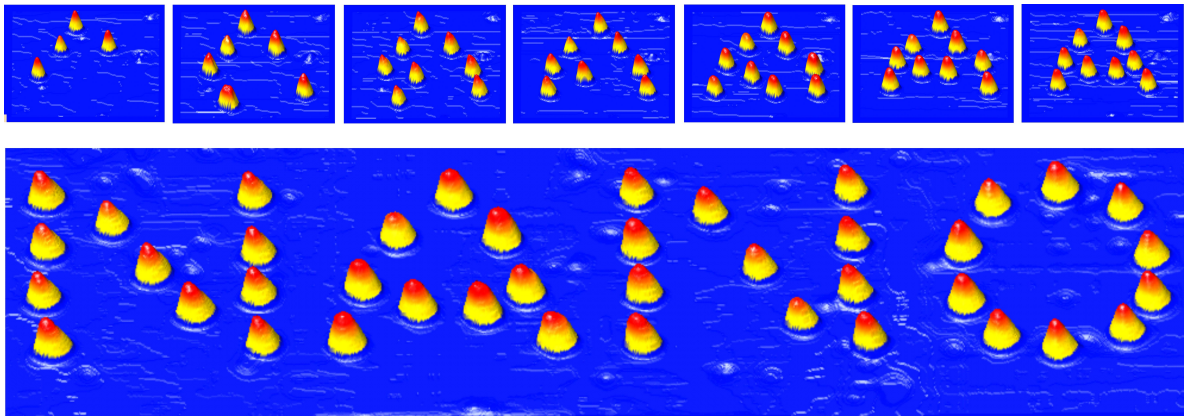

Figure 5.9: Assembly of the artificial structure using the lateral manipulation technique. The structure 'NANO' built by control repositioning of C_{60} molecules on Ag(100). The size of each letter is around $16 \times 16\,\mathrm{nm}^2$.

5.7 Conclusions

The C_{60} molecule is the most common and extensively studied representative of the fullerene family. The study of its adsorption on metal surfaces reveals the most important features of the chemisorbed fullerenes, which may provide an important reference for the later study of metallofulerenes. Due to the high symmetry of the cage, interpretation of the data obtained for C_{60} is relatively straightforward. The STM images show a characteristic pattern which corresponds directly to the symmetry of the molecular orbitals and allows to determine the preferential orientation of the molecule with respect to the substrate. The spectroscopic data clearly show that the electronic structure of the C_{60} is modified by the chemisorption. The broadening of the peaks in the STS spectrum is related to the hybridization of the substrate-C_{60} states. The results indicate also that a considerable amount of charge is donated from the substrate to the fullerene. The charge transfer leads to a partial filling of the LUMO of the molecule, which gives rise to an additional LUMO-derived feature in the vicinity of the Fermi level. The results indicate that the interaction with the substrate can strongly influence the density of states of fullerene and similar effects may also modify the observed spectra of metallofullerenes.

The identification of the origin of the vibrational features resolved in by IETS spectra for fullerenes is a difficult task, because normally only few out of the many distinct modes are detected. The fact that the frequencies of the modes may shift upon the chemisorption additionally complicated the assignment. In case of C_{60} two vibrational modes have been observed, corresponding most probably to $H_g(\omega_2)$ and $H_g(\omega_5)$.

Finally, it has been also demonstrated that C_{60} molecules can be repositioned by the STM tip. The tip height traces recorded during the manipulation indicate that C_{60} has been pushed along the surface. By using the lateral manipulation technique, the artificial molecular nanostructures can be assembled.

Chapter 6

Electronic and vibrational properties of $Ce@C_{82}$ metallofullerene

Small production yields of metallofullerenes and their lower stability contribute to the fact that endohedral complexes have received significantly less attention in STM studies than the rigid C_{60}. Among the few STM reports on the endohedral fullerenes, most are focused on multilayer structures of the lathanide complexes, $M@C_{82}$ [150, 151, 152, 153], especially $La@C_{82}$[150, 151]. D.F. Leigh *et al.* [153] and K. Wang *et al.* [154] have demonstrated a good agreement between the STM images and theoretical models of $Nd@C_{82}$ and $Dy@C_{82}$. Based on the combined theoretical and experimental approach they have tried to determine the orientation of the C_{82} cage on the substrate. Several groups have also discussed the STS electronic spectra of $La@C_{82}$ and $Ce@C_{82}$ [150, 151, 152], showing a small HOMO-LUMO gap and position of SOMO orbital in agreement with the photoemission valence band spectra. Recently, M. Grobis *et al.* presented a detailed study of elastic and inelastic tunneling through a single metallofullere, $Gd@C_{82}$[155]. The results reveal a high localization of the spectroscopic signal within the fullerene molecule.

In this chapter the structure and properties of $Ce@C_{82}$ molecules adsorbed on Cu(111) are discussed. As it will be shown in the next sections, the interpretation of the data is not straightforward. However, the comparison of the experimental results with the density functional theory (DFT) model of the molecule allows to determine the orientation of the molecule with respect to the substrate and establish the origin of the features resolved by scanning tunneling spectroscopy.

6.1 Calculated geometry of $Ce@C_{82}$

The theoretical results presented in this Chapter have been obtained by Kaliappan Muthukumar and J. Andreas Larsson at the Tyndall National Institute, Cork, Ireland [91]. The geometry and properties of the molecule have been calculated using the

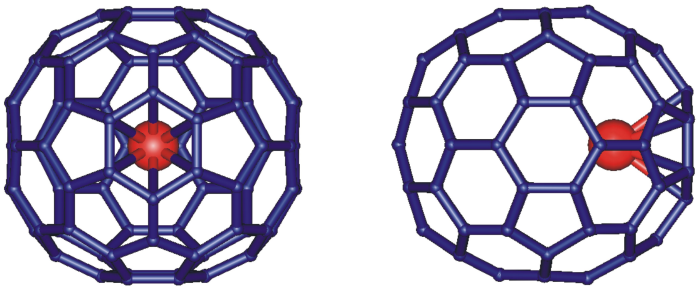

Figure 6.1: The geometry of Ce@C_{82} molecule calculated by DFT. The Ce atom occupies a preferential chemisorption site inside the C_{2v} isomer of C_{82} cage.

density functional theory (DFT). The generalized gradient approximation (GGA) has been applied [156] with the PBE exchange-correlation functional. The carbon atoms have been described by the polarized valence triple zeta basis set (TZVP) [157]. For the cerium atom a standard 28 electron effective core potential (ECP-28-MWB) has been employed [158], leaving 30 electrons within the computations. All calculations have been performed using Turbomole program system [159]. The fullerene was isolated in vacuum and the interaction with the substrate was not considered.

The geometric structure of M@C_{82} metallofullerenes has been shortly introduced in Chapter 3.4. The calculations by K. Muthukumar *et al.* reveal that the geometry of the Ce@C_{82} is similar to other fullerenes of this family. The optimized structure of the Ce@C_{82} is presented in Fig. 6.1. Upon doping with a cerium atom, the most favored isomer of C_{82} has C_{2v} symmetry. The metal atom resides on the C_2-axis and binds to the hexagon ring lying on the symmetry axis. This preferential position has been found to be much more stable than any other configuration. The preference of the chemisorption site can be explained by the interaction between d orbitals of cerium and the carbon cage. According to the calculations, the hybridization between d states of the metal and π states of C_{82} is especially favored for this particular hexagon ring. The model predicts also that the presence of cerium leads to a local distortion of the C_{82} cage.

The DFT results confirm 3+ oxidation state of Ce. However, the charge is not delocalized over all carbons but remains in the chemical bonds between Ce and the cage, and on the neighboring atoms. Also a considerable back-donation of the charge takes place, into $5d$ and $6p$ orbitals of the metal. The $4f$ electron is found to be mostly localized on the cerium atom.

6.2 Adsorption geometry on Cu(111)

The room temperature deposition of Ce@C_{82} molecules on Cu(111) leads to formation of islands on the substrate. STM image of the surface with a submonolayer coverage of metallofullerenes is shown in Fig. 6.2. Small molecules or single atoms

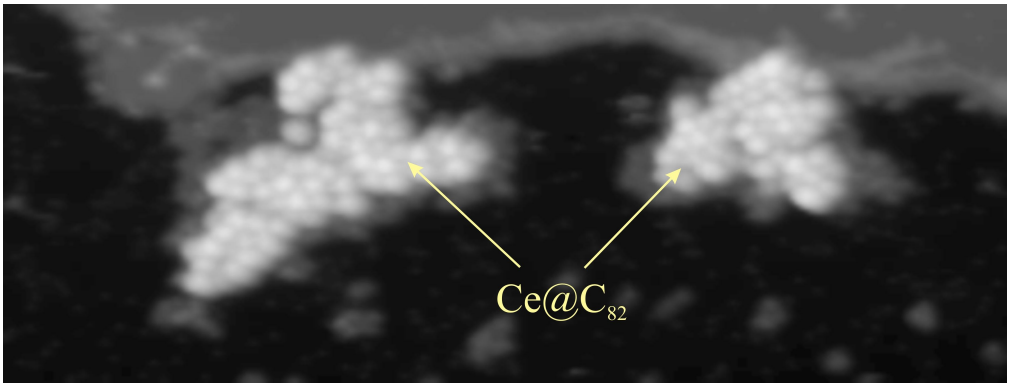

Figure 6.2: STM image of Cu(111) surface after submonolayer deposition of $Ce@C_{82}$. The molecules arrange in disordered islands growing at the step edges. ($6 \times 25\,nm^2$, $V = 2\,V$, $I = 0.1\,nA$)

present on the surface next to the fullerenes are probably rests of the toluen solution used as a solvent. The growth of $Ce@C_{82}$ starts at the step edges and the resulting islands are disordered. The internal structure of the molecules is clearly resolved in STM images, as shown in Fig. 6.3(a) and (b). A number of different patterns is seen in the images. A clear striped structure is resolved for some molecules, other show more complex shapes. The variety of observed patterns indicate that there is no preferential adsorption configuration for the molecules on the substrate and the orientation of the cage is random. Images of the same island at different bias voltages reveal that each molecular pattern is bias dependent, which is visualized in Fig. 6.3(c)-(f). The changes of the internal structure are due to the fact that, depending on the applied voltage, different molecular orbitals contribute to the tunneling. The complex striped patterns resolved at low bias ($V = -0.2\,V$, Fig. 6.3(a) and (d)) typically evolve into ring-like shapes, present in empty states image ($V = 2\,V$, Fig. 6.3(b) and (f)). The characteristic rings resemble the structure of the unoccupied orbitals of C_{60} molecule, where the density of states is localized on the cage pentagons [126]. However, compared to C_{60} the internal patterns of $Ce@C_{82}$ are much more complex, due to the lower symmetry of the molecule. Therefore, the relation between the internal structure and the cage orientation cannot be easily established without help of theoretical modelling.

In order to determine the orientation of the molecules, a DFT model of an isolated $Ce@C_{82}$ molecule has been considered. The calculations of the electronic structure of the molecule yield in particular the Kohn-Sham electron densities of the molecular orbitals. To simulate the constant current STM images, one has to account for the fact that the topograph of a molecule is determined not only by the LDOS arising from a single energy level, but by all the orbitals lying within the bias window. Accordingly, the images corresponding to STM topographs have been generated by summing over all the relevant states contributing to the tunneling at the given bias voltage. The simulations have been done for two different voltages: $V = -0.2\,V$, corresponding to the occupied states of $Ce@C_{82}$ and $V = 2\,V$, corresponding to the empty states. The

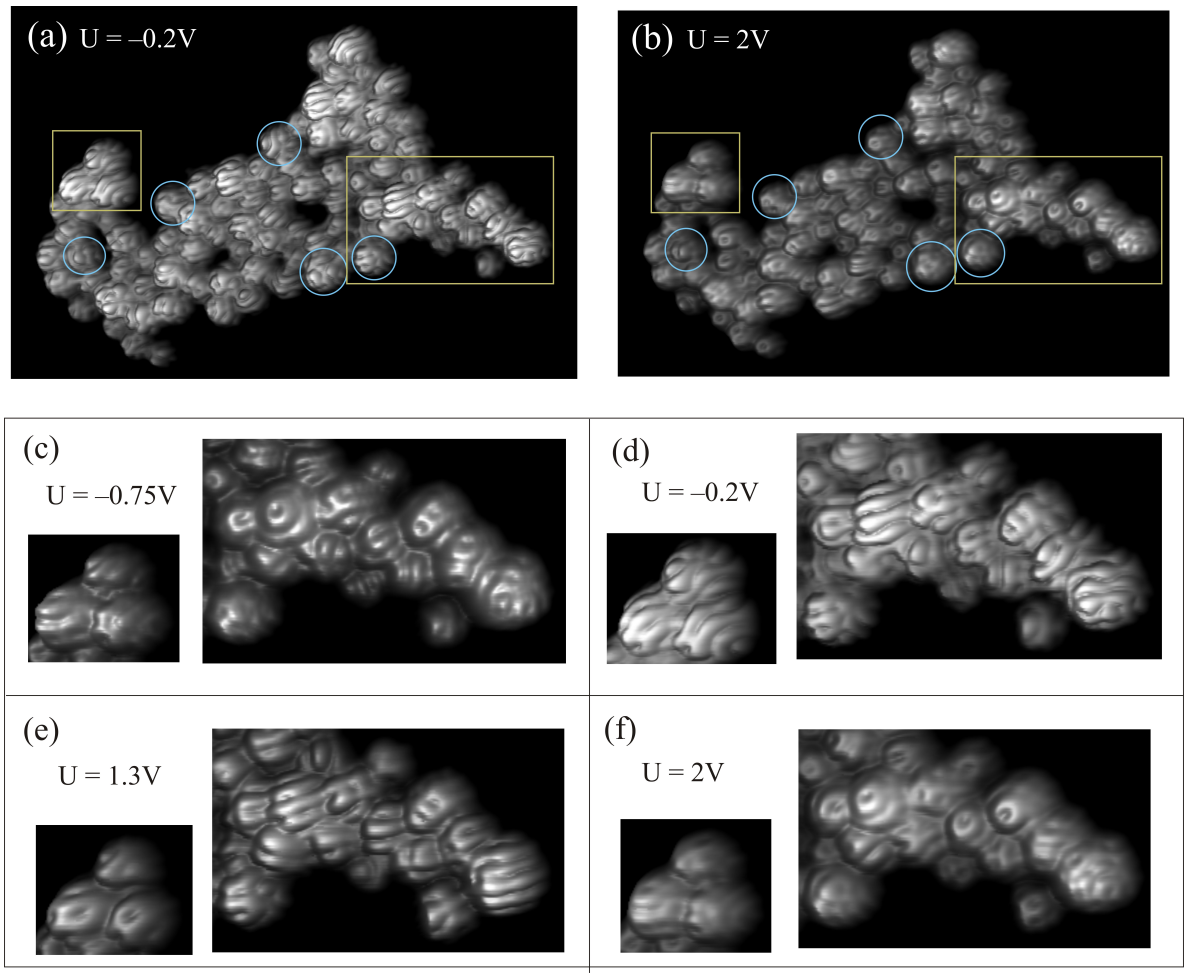

Figure 6.3: Constant current images of a $Ce@C_{82}$ island, revealing the internal structure of the molecules. The pattern is bias dependent. The boxes indicate the areas of the island presented in images (c)-(f). The circles denote the orientations modelled by DFT in Fig. 6.4. (a) Occupied states STM image of the $Ce@C_{82}$ island at $V = -0.2\,\mathrm{V}$ (b) Empty states STM image of the same island at $V = 2\,\mathrm{V}$. The striped patterns resolved in (a) change into ring-like structures in (b). (c)-(f) The images of the cutouts of the island acquired at different bias voltages: (c) -0.75 V, (d) -0.2 V, (e) 1.3 V and (f) 2.0 V. All images have been acquired at the tunneling current $I = 0.2\,\mathrm{nA}$.

empty states topograph has been generated by summing over the electronic states of $Ce@C_{82}$ above E_F up to 2 V (for details on electronic structure see Section 6.3.3). To simulate the STM images at $V = -0.2$ V, it has been assumed that the transport near the Fermi level is dominated by half-filled SOMO and lying next to it HOMO-1 (see Section 6.3.3 for details).

The orientation-dependent images of $Ce@C_{82}$ have been then generated in this work by plotting the isosurface of the calculated sum of the Kohn-Sham electron densities. The simulated images have been compared to the STM topographs shown in 6.3(a) and (b). The orientation of the molecule in the DFT model has been adjusted to obtain for each fullerene a satisfactory fit at two voltages simultaneously. Such consistent matching of empty and occupied states gives more confidence in determining the bonding configuration of the molecules than fitting only one bias polarity [153].

Several characteristic patterns resolved in Fig. 6.3(a) and (b) have been reproduced. The results are presented in Fig. 6.4. First two columns refer to the occupied states images, next two to the unoccupied states images. The last column shows the corresponding orientation of the carbon cage. The calculated distribution of the empty states electron density reproduces very well the ring-like structures observed in STM. The calculated density is localized on the cage pentagons and some of the C-C bonds between the two hexagons, leading to the conclusion that the rings resolved by STM indeed reproduce the pentagon/hexagon structure of the C_{82} cage. The calculated Kohn-Sham density for the occupied states shows more complex structure and gives variety of completely different patterns depending on the viewing angle.

However, not for all molecules a satisfactory match could be found. This may be due to the presence of another cage isomer in the metallofullerene sample, probably C_s [92, 93]. To reproduce more internal patterns the calculations for both cage isomeric structures would be necessary, as reported for $Nd@C_{82}$ in Ref. [153]. The theoretical model also does not account for the interaction of the molecules with Cu(111) substrate. As already shown for C_{60} in Chapter 5, chemisorption affects the electronic properties of the molecule and may therefore alter the spatial distribution the the molecular orbitals.

6.3 Electronic spectroscopy

6.3.1 Photoemission spectroscopy

The electronic structure of $Ce@C_{82}$ thin films has been studied by photoemission and x-ray absorption spectroscopies. Results have been obtained by Karina Schulte *et al.* (Nottingham Univeristy, UK) at Synchrotron Radiation Source, Daresbury Laboratory, UK and MaxLAB, Sweden [160, 161, 162]. The valence-band spectrum of a $Ce@C_{82}$ film on Ag:Si(111)$(\sqrt{3} \times \sqrt{3})$ is presented in Fig. 6.5. The spectrum of hollow C_{82} is given for reference. The comparison of the two spectra is not straightforward because of different geometric structure (isomer) of the doped and empty cage. However, it is clear that significant differences between the two spectra appear for the low binding energies (within a few volts from the Fermi level). The spectral onset of the valence band spectrum of $Ce@C_{82}$ is located at 0.3 eV below the Fermi level, indicating that

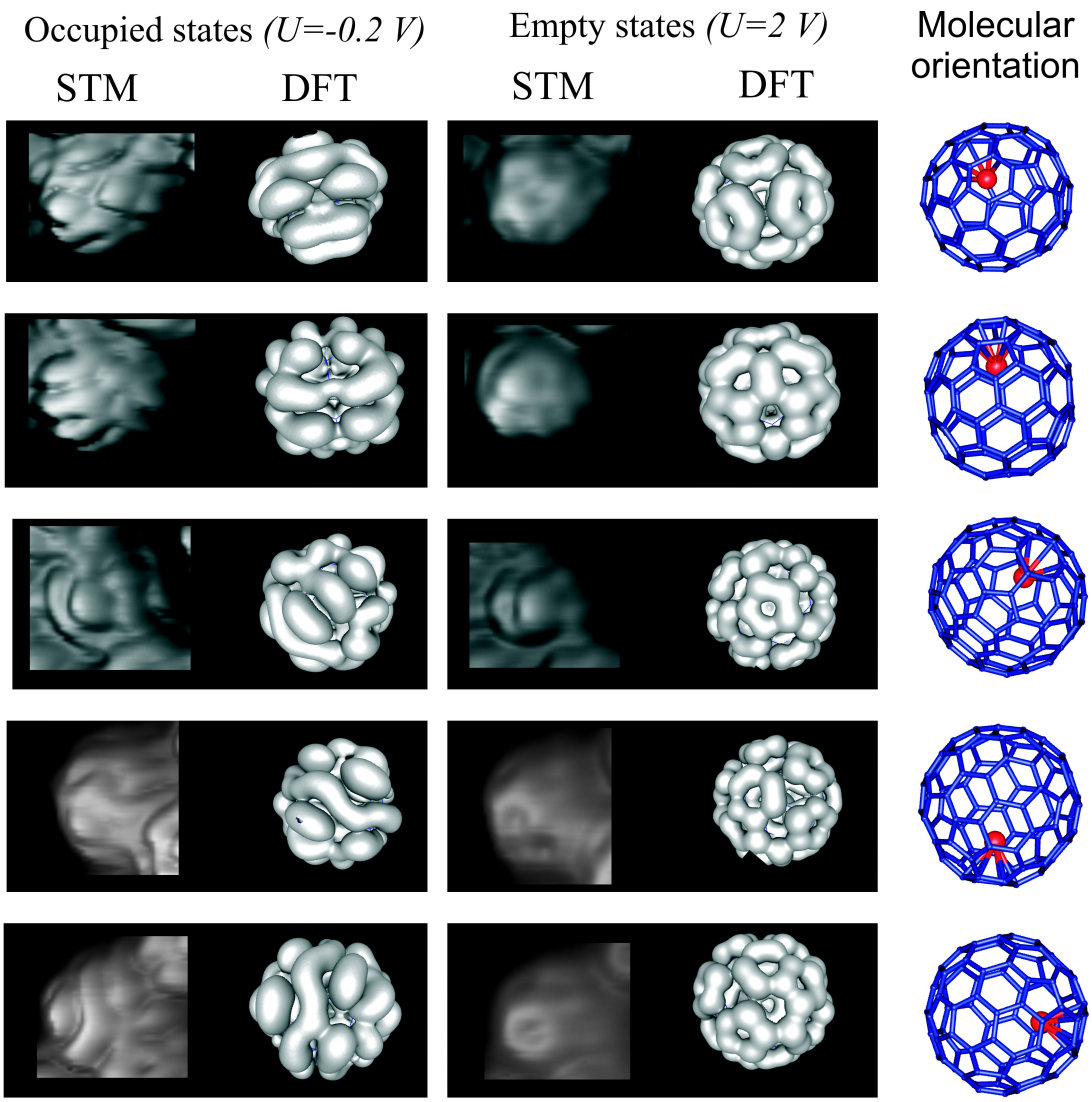

Figure 6.4: Comparison of the experimental STM images of $Ce@C_{82}$ (first and second column) and calculated isosurfaces of Kohn-Sham densities (second and forth column), for different orientations of the cage. STM images of occupied (first column) and empty states (third column) have been cut from the images of the island presented in Fig. 6.3(a) and (b). Orientation of molecule in the DFT model has been chosen to optimally match the characteristic features resolved by STM at two bias polarities. The corresponding geometry of the molecule is presented in the last column.

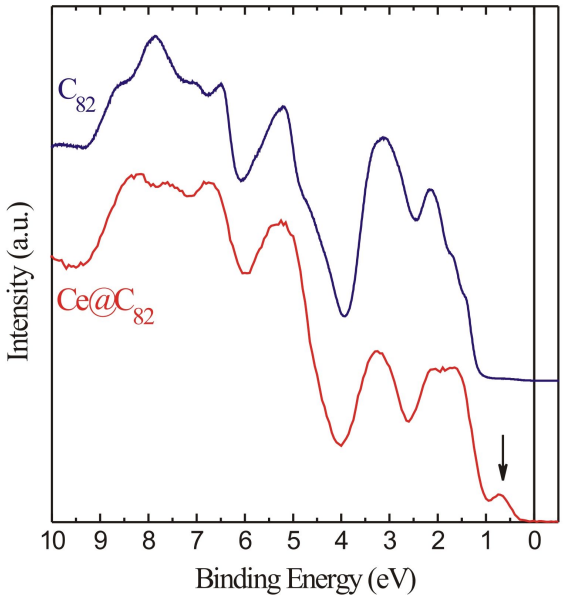

Figure 6.5: The valence band spectra of the ordered films of $Ce@C_{82}$ (a) and C_{82} (b). SOMO-derived feature is indicated by an arrow. (The incident photon energy was 60 eV.) (K. Schulte *et al.*, Nottingham, UK)

$Ce@C_{82}$ film is semiconducting with a band gap of at least 0.3 eV. Futhermore, the low energy peak present for $Ce@C_{82}$ is absent in C_{82} spectrum and the overall shape of the band centered at 1.65 eV is different in both plots. As already mentioned in Section 3.4 and illustrated in Fig. 3.7(a), electronic structure of $Ce@C_{82}$ in the vicinity of the Fermi level is determined by the charge donation from the encapsulated atom. Accordingly, the peak located at -0.73 eV for $Ce@C_{82}$ can be assigned to a SOMO-derived band (singly occupied molecular orbital). Similar feature was also identified in the valence-band spectra of $La@C_{82}$ [163].

6.3.2 Dependence of electronic properties on molecular adsorption geometry

The previous section has demonstrated that $Ce@C_{82}$ molecules deposited on Cu(111) form disordered islands and exhibit a random orientation with respect to the substrate. The local tunneling spectroscopy measurements have been performed in order to determine how the adsorption geometry influences the electronic properties of the fullerene. The STS spectra have been recorded over the center of differently oriented molecules. Based on the results, a specific electronic spectrum could be correlated with a particular molecular orientation. Several different types of spectra have been observed. Figure 6.6 shows the characteristic STS curves together with the corresponding STM images of a specific molecular orientations. The results exhibit a strong dependence on the position of the carbon cage on the substrate, suggesting that molecular orbitals are

highly localized within the fullerene.

The variations in the electronic structure within the fullerene island become even more evident when one looks at the spatial localization of the STS signal. The differential conductance maps of the island discussed in Section 6.2 are shown in Fig. 6.7. The maps show the spatial distribution of dI/dV for two distinct bias voltages $V = 1.6\,\mathrm{V}$ and $V = 0.75\,\mathrm{V}$, corresponding to the spectroscopic features resolved in the STS spectra (Fig. 6.7(a) and (b)). The two images show almost reversed pattern: the molecules highlighted in image (a) (red, indicated by arrows) i.e. exhibiting a high density of states at bias voltage $V = 2\,\mathrm{V}$, become 'dark' in (b), i.e. their density of states at $V = 0.75\,\mathrm{V}$ is significantly lower compared to other molecules. However, no special periodic pattern in the maps is observed, what is consistent with the fact that molecules are randomly oriented on the substrate. The contrast between the molecules becomes clear only in the spectroscopic images and is not present in the constant current images. Therefore, it must be due to the differences in the electronic properties.

The tunneling spectroscopy reveals also that electronic spectra may alter at different measurement points within the same molecule. The data show that STS spectrum measured at the edge of the molecule is often different than the one measure in the middle. However, the observed dependence has not been so strong to affect the data presented in this section. The intramolecular spatial dependence of the electronic states has not been investigated in detail, but the preliminary results are in qualitative agreement with the recent report on $Gd@C_{82}$ [155].

The exact identification of the STS features is not trivial, due to the complex electronic structure of the endohedral fullerenes. However, comparison with the photoemission spectroscopy and density of states calculated by DFT provides a better understanding of the STS results. The detailed analysis and interpretation of the data is presented in the next section.

6.3.3 Comparison of experimental and theoretical results

In order to get a better insight into the electronic structure of $Ce@C_{82}$, characteristic STS spectra have been plotted in the same graph (Fig. 6.8(a)) and compared with the theoretical calculations (Fig. 6.8 (b)). Let us first focus on the STS results summarized in Fig. 6.8 (a). Both edges of the occupied and empty states approach the Fermi level and a small energy gap is present in each spectrum. The gap width is in the range of $0.3\,(\pm 0.1)\,\mathrm{V}$, what well agrees with the UPS results. The significant differences between the spectra appear in the empty states part of the plot (positive voltages). In the occupied states (negative voltages) two peaks located at -1.25 $(\pm 0.1)\,\mathrm{V}$ (*II*) and -1.7 $(\pm 0.1)\,\mathrm{V}$ (*III*) are resolved in each plot. In several spectra also a characteristic feature centered at around -0.65 $(\pm 0.1)\,\mathrm{V}$ appears (*I*).

Fig. 6.8 shows the calculated density of states of $Ce@C_{82}$, modelled by DFT. Each electronic state of the molecule is represented by a vertical line. The green lines denote the orbitals with considerably high contribution from the encapsulated Ce atom (mixed Ce-cage orbitals). The states with no Ce contribution, i.e. localized only on the carbons, are marked black. The density of states, obtained by gaussian broadening with a full

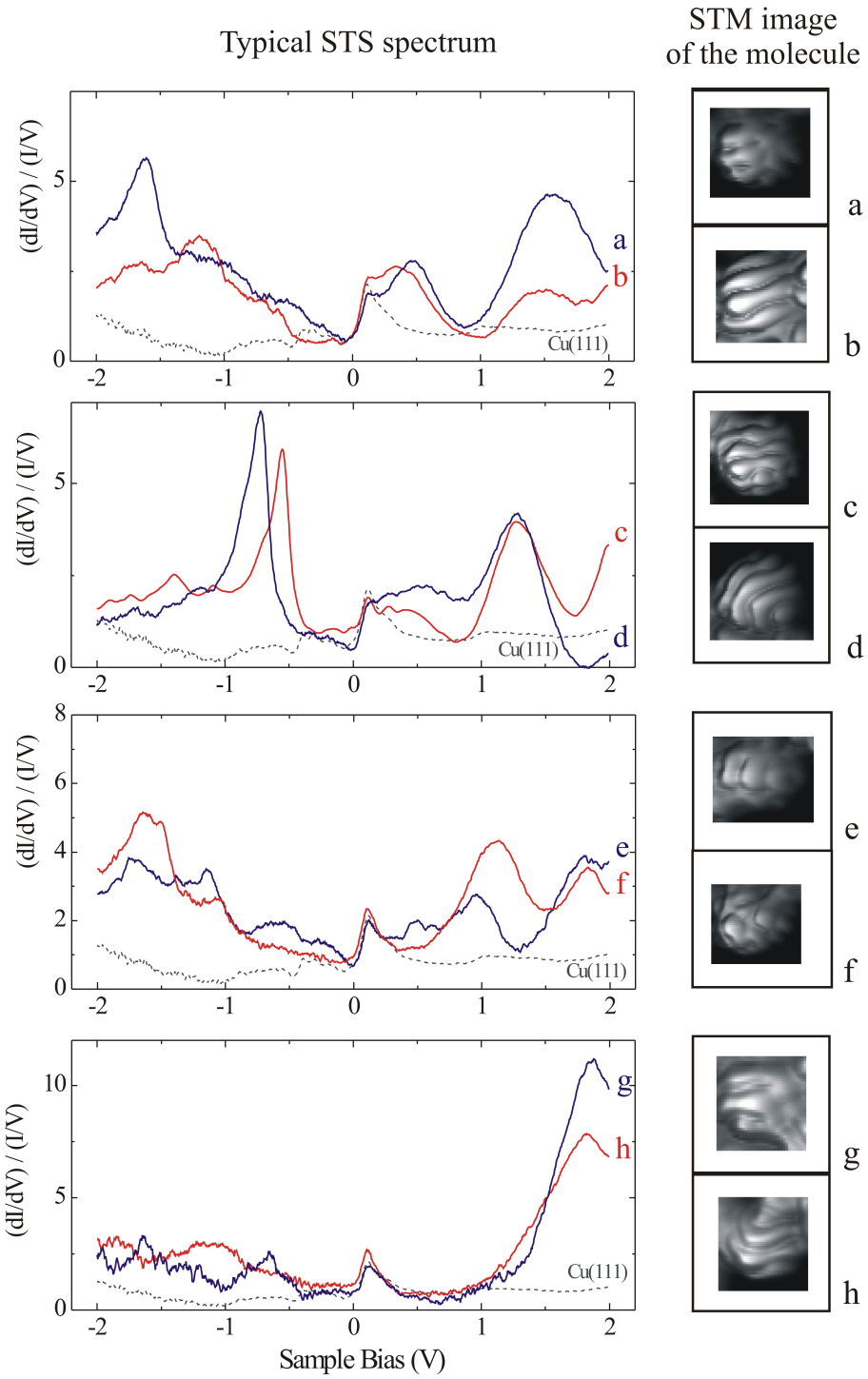

Figure 6.6: STS electronic spectra obtained for different Ce@C_{82} molecules within the island imaged in Fig. 6.3. The spectra depend strongly on the adsorption geometry of the molecule. For each curve a corresponding STM image of specific orientation is presented ($V = -0.2\,\mathrm{V}$, $I = 0.2\,\mathrm{nA}$). (Tunneling parameters $V = 2\,\mathrm{V}$, $I = 0.1\,\mathrm{nA}$, $V_{ac} = 10\,\mathrm{mV}$ (rms))

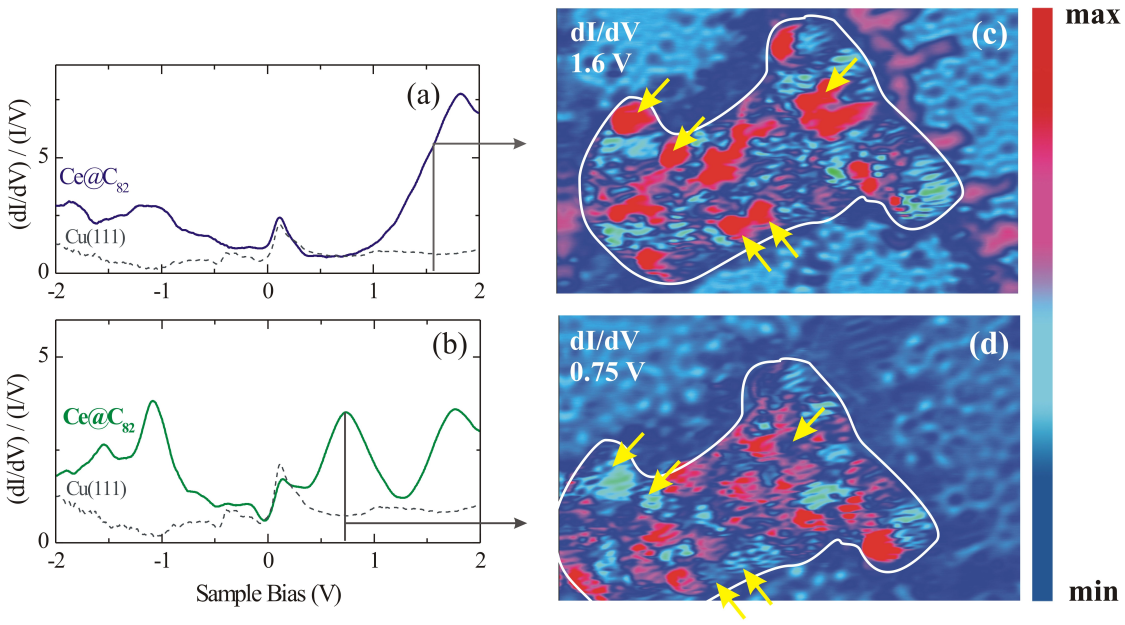

Figure 6.7: Differential conductance maps of $Ce@C_{82}$ island at two different bias voltages, referring to the features resolved by STS. (a) and (b) Two characteristic STS spectra measured on differently oriented molecules. (c) and (d) Spatial distributions of dI/dV at $V = 1.6\,\mathrm{V}$ and $V = 0.75\,\mathrm{V}$, respectively ($I = 0.1\,\mathrm{nA}$). Corresponding features in the STS spectra are indicated in the graphs. For easier comparison, the arrows denote the examples of the same molecules in two images.

width at half maximum (FWHM) equal to 0.2eV, is shown as a continuous curve above. The Fermi level is aligned to the HOMO orbital of the molecule. Calculations predict that the ground state of $Ce@C_{82}$ is a triplet, i.e. HOMO is only half occupied, giving rise to a singly occupied molecular orbital SOMO (I'). The SOMO state has a partial Ce-character and is dominated by the $4f$ orbital of cerium. This result is consistent with the experimental study of Kessler *et al.* [104], who determined a strong La contribution to the SOMO-derived feature of $La@C_{82}$. The calculated distribution of the SOMO orbital of $Ce@C_{82}$ is visualized in Fig. 6.9. The electron density localized on metal reflects the shape of the $4f$ orbital.

According to the theoretical model, empty orbitals of $Ce@C_{82}$ exhibit a significant cerium character. The hybridized states are partially located on the encapsulated metal atom, as illustrated on the example of SOMO in Fig. 6.9. The remaining part of the orbital is localized on the cage, predominately on the carbon atoms close to the metal-C_{82} chemical bond. The hybrid states can be detected by the STS measurements only if the fraction of the orbital localized on the cage is accessible for the electrons tunneling from the tip. Since this condition is fulfilled only for limited number of molecular orientations, the variation of the bonding geometry yields significant changes in the structure of the empty states DOS in the electron tunneling spectra of $Ce@C_{82}$.

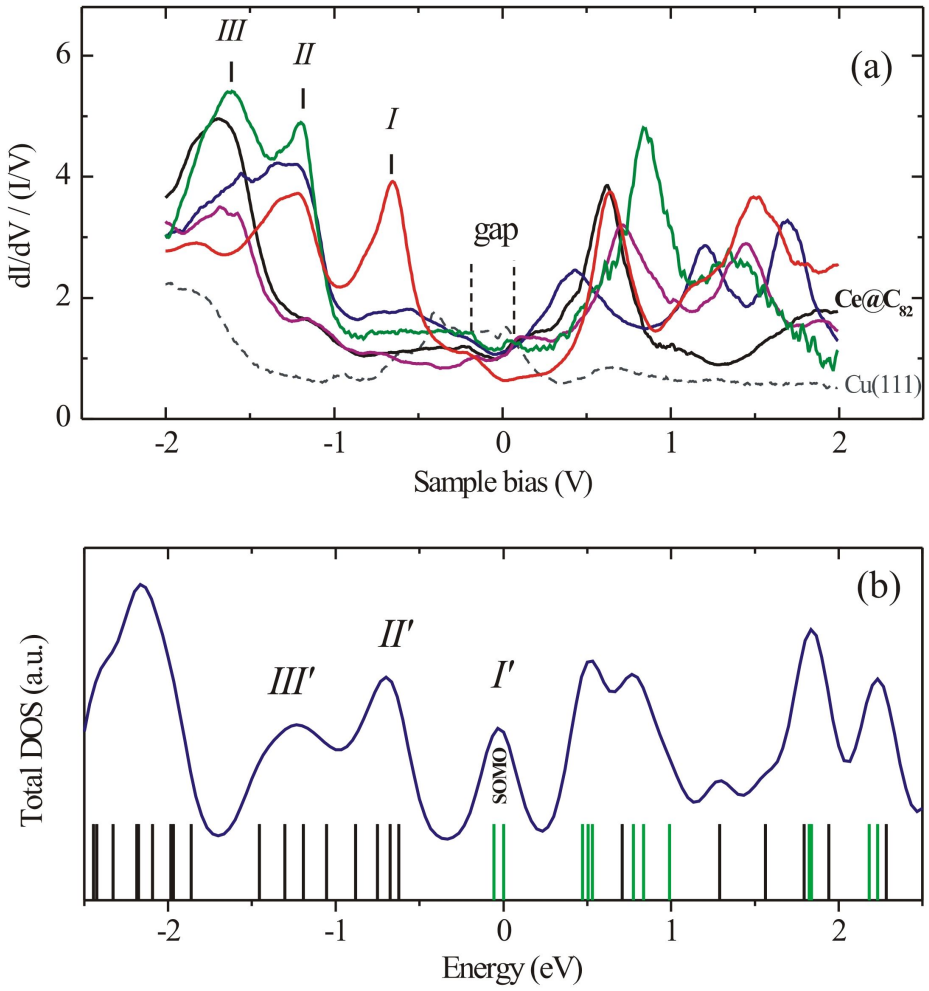

Figure 6.8: Electronic structure of $Ce@C_{82}$ measured by STS and modelled by DFT. (a) STS spectra measured for differently oriented molecules. The features referred to in the text are indicated by *I-III*. (Tunneling parameters before taking the spectra were $V = -2\,\mathrm{V}$, $I = 0.1\,\mathrm{nA}$.) (b) Density of states of $Ce@C_{82}$ calculated by DFT. Green vertical lines denoted the molecular orbitals with contribution from the Ce atom (hybrid metal-cage states). The Fermi level has been aligned with the SOMO orbital of the molecule. Continuous line is the gaussian-broadened DOS. The features identified in the STS spectra are indicated by *I'-III'*.

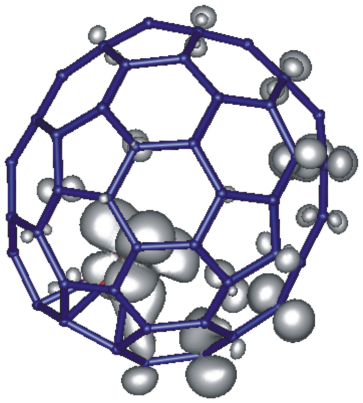

Figure 6.9: Isosurface of electron density of singly occupied orbital (SOMO) of Ce@C_{82}, as calculated by DFT. The orbital is partially localized on the encapsulated metal atom and dominated by the $4f$ state.

In contrast to the metal-C_{82} hybrid states, the orbitals with no Ce contribution are delocalized over the whole carbon cage. Calculations predict that in the occupied part of DOS, apart from the SOMO and HOMO-1, only cage states are present. The delocalized states can be observed by tunneling spectroscopy regardless of the molecular orientation. Consequently, no significant changes are present in STS for the negative sample bias, below $\sim -1\,\mathrm{V}$. The theoretical broadened DOS reveals a characteristic two peak structure corresponding to the delocalized carbon orbitals (*II'* and *III'*). A similar structure resolved by STS (peaks *II* and *III*) can be therefore identified with a band arising from the delocalized C_{82} cage states.

The last feature, whose origin was not discussed so far, is the sharp peak resolved in the occupied part of the STS spectrum at -0.65($\pm$0.1) V (*I*). The fact that its presence is strongly dependent on the orientation of the molecule suggests that this feature is probably related to one of the hybridized metal-cage states. Its position with respect to peaks *II* and *III* correlates well with the energy difference between the calculated SOMO (*I'*) and structure *II'* and *III'*. Consequently, we attribute feature *I* to a SOMO-derived state. Such assignment is also in agreement with the photoemission studies, where such feature was identified at -0.73 eV binding energy.

The final issue that requires explanation is the energy scale of STS measurements and DFT model. It is clear that the shape of theoretical DOS resembles the structure resolved for occupied states by STS, but the calculated energy levels have to be lowered by approximately 0.65 V/eV. It would be logical to expect the feature corresponding to SOMO, i.e. the half-filled orbital, directly at or close to the Fermi level. However, charge transfer or presence of the Coulomb repulsion energy may account for the shift of the peaks in the STS spectrum [19, 125]. Generally, following issues can be considered to explain the shift of the SOMO orbital and the energy difference between the experimental and theoretical spectrum of Ce@C_{82}:

- The eigenvalues of the DFT orbitals typically do not correspond to the energies measured by photoemission or tunneling spectroscopy. The position of the Fermi level has to be chosen independently. The DFT eigenvalues reproduce well the energy-level spacings, but underestimates the energy gap between occupied and unoccupied states, i.e. the HOMO-LUMO distance. This well known problem

is due effects arising from electron-electron interactions, that are not very well described by DFT.

- The energies of the molecular states measured by STS may substantially change when the molecule is chemisorbed (discussed for C_{60} in Sec. 5.2). The hybridization with the substrate band states usually alters the electronic structure of the molecule and leads to the splitting of the degenerate levels. Also the additional charge transfer can shift the position of molecular orbitals. When the HOMO of the molecule is only partially filled (as in case of SOMO) the additional charge donation from the substrate may fill the orbital. The change in the occupation of the molecular states would in consequence cause a downshift of the energy levels. Such assumption is justified in case of $Ce@C_{82}$, because the metal substrates are known to donate electrons to the fullerenes [155] (see also Sec. 5.2). The charge transfer has been also proposed as the explanation of differences between theoretical and experimental results for $La_2@C_{72}$ [164].

- The tunneling spectrum may be affected by the charging energy arising from Coulomb repulsion between two electrons in a molecule. The Coulomb repulsion increases the energy required to add or remove electron from the orbital and changes the observed HOMO-LUMO gap. The effects of charging energy have been already observed in STS measurements for C_{60} on metal surfaces [125] and may be also present in case of metallofullerenes.

The discussed shift of the calculated DOS reproduces also remarkably well UPS valence band spectra of $Ce@C_{82}$, presented in Section 6.3.1. The final Figure 6.10 shows the comparison of the electronic spectra obtained by STS, UPS and shifted DFT. A good agreement between all three approaches is achieved.

Given the above interpretation of the STS spectra, a remark is necessary regarding the simulation of the STM images discussed in the previous section (Fig. 6.4). It has been demonstrated that the internal structure of the molecules imaged at the bias voltage $V = -0.2\,\mathrm{V}$ can be satisfactory matched by taking into account the SOMO and HOMO-1 orbitals. This statement is not obvious, considering the fact that the main peak corresponding to SOMO appears in the STS spectra at the bias voltage $\approx -0.65\,\mathrm{V}$. However, upon chemisorption a strong interaction between the half-filled SOMO and the Cu(111) substrate can be expected, due to a charge donation from the metal surface. This process can account for the presence of HOMO-1- and SOMO-derived states in the vicinity of the Fermi level, through the splitting and broadening of the molecular resonances.

6.4 Vibrational modes of $Ce@C_{82}$

The vibrational properties of the molecules have been studied by inelastic tunneling spectroscopy (STM-IETS). The spectrum acquired over $Ce@C_{82}$ adsorbed on Cu(111) is shown in Fig. 6.11. Two clear peaks resolved for $Ce@C_{82}$ at 60 mV and 88 mV are

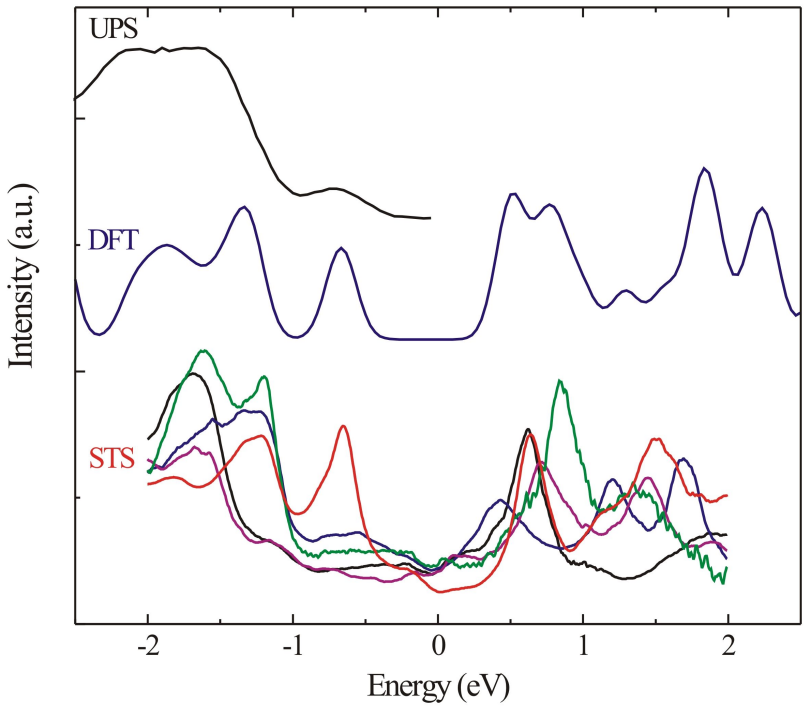

Figure 6.10: Comparison of tunneling spectra, UPS valence band spectrum and DFT calculations of $Ce@C_{82}$ molecule. Lowering the occupied energy levels in DFT by -0.65 eV gives good agreements with UPS and STS spectra. The features *I-III*, described in the text, can be identified in all three curves.

not present in the spectra recorded over bare Cu(111) substrate. Since the peaks have their counterparts as dips in the opposite bias polarity, they can be attributed to the vibrational excitations of the molecule. The modes lead to a total increase in differential conductance of approximately 10-15% and 5%, respectively.

The origin of the observed vibrational modes is not clear. The theoretical calculations of the vibrational structure of $Ce@C_{82}$ reveal that there are over 200 distinct vibrational frequencies present, in the energy range up to ∼220 meV. Out of these modes, only three involve the movement of the encapsulated metal atom. Those modes, however, exhibit low energies: 4 meV , 4.5 meV and 18 meV, in agreement with Raman and IR reports [93, 105]. None of these modes is been detected by STM-IETS. In the spectrum in Fig. 6.11 the low energy region is dominated by the feature arising from the tip. We can exclude the possibility that the two modes observed at 60 mV and 88 mV have any contribution from Ce atom and assign them to purely internal C_{82}-cage vibrations. The mode resolved in the spectrum at 60 mV is most probably the same mode that has been measured by STM-IETS for $Gd@C_{82}$ on Ag(001) [155]. The dominance of this mode in the vibrational spectrum of endohedral fullerene has been explained by strong coupling of a specific cage mode to the electronic state of the C_{82} cage at the Fermi

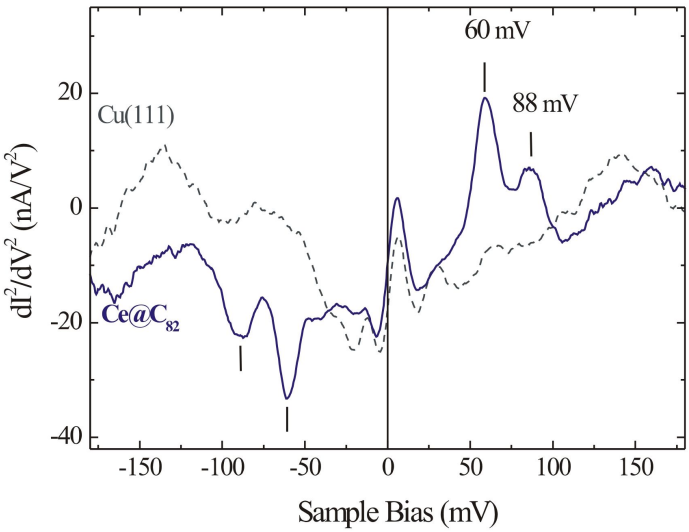

Figure 6.11: Typical STM-IETS spectrum measured for $Ce@C_{82}$ on Cu(111). Two pronounced features resolved at 60 mV and 88 mV can be identified as intramolecular cage vibrational modes. The dashed curve corresponds to the reference spectra recorded on bare Cu(111). (Tunneling parameters: $V = 250\,\mathrm{mV}$, $I = 0.5\,\mathrm{nA}$, $V_{ac} = 6\,\mathrm{mV}$ (rms))

level.

The effect of the $Ce@C_{82}$ adsorption geometry on the STM-IETS spectra has been investigated as well, but in contrast to electronic spectra, no significant changes in the vibrational spectra have been observed. The same two modes are resolved for each molecule, regardless of its orientation on the substrate. However, there is a clear increase in the inelastic signal for some molecular orientations, whereas other fullerenes show only faint features or a flat spectrum. The inelastic spectra obtained for different $Ce@C_{82}$ molecules are shown in Fig. 6.12, illustrating the modification of the d^2I/dV^2 intensity for different bonding configurations. To explain the observed enhancement or lack of the signal, the fundamentals of the inelastic tunneling must be considered, especially the influence of the adsorbate electronic structure on the vibrational excitation. Recently, M. Grobis *et al.* in Ref. [155] predicted a strong localization of the inelastic signal for $Gd@C_{82}$. The calculations in Ref. [155] account for the presence of the metal atom only by considering the charge transfer to the bare cage. Since the the same amount of charge ($3\,e^-$) is donated in case of Ce and Gd, a similar strong localization of the vibrational signal can be expected for $Ce@C_{82}$. This process is probably responsible for the changes in the intensity of the inelastic signal, depending on the orientation of the molecule.

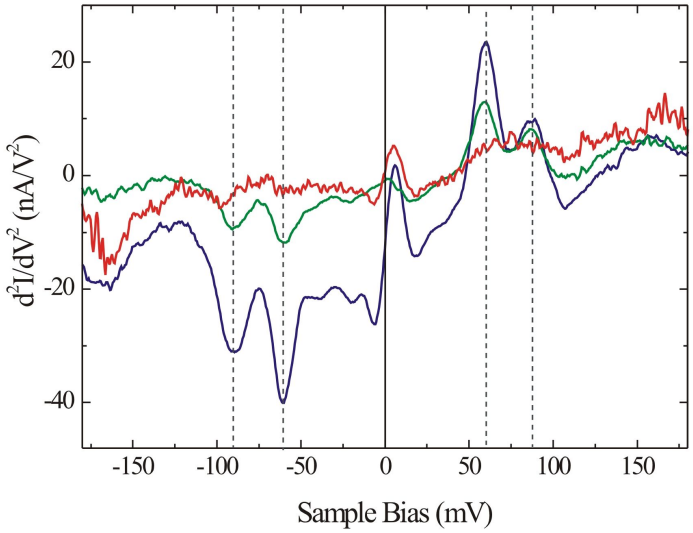

Figure 6.12: Vibrational spectra of Ce@C_{82} recorded over differently oriented molecules. The variations in the intensity of the inelastic signal are observed. For some molecules no vibrational modes have been detected (red curve).

6.5 Conclusions

The discussion presented in this chapter clearly illustrates the difficulties that occur during analyzing the results obtained for adsorbed metallofullerenes. In the previous Chapter regarding the properties of C_{60} fullerene (Chap. 5), the analysis of the data has been based on the high icosahedral symmetry of the molecule. The geometry and therefore also electronic structure of metallofullerenes is much more complicated and the results cannot be always well understood in their complexity. The accurate interpretation of the data is possible only based on the theoretical calculations.

The comparison of experimental and simulated constant current topographs of Ce@C_{82} on Cu(111) has allowed to identify the characteristic intramolecular patterns resolved in the STM images. The internal structure of the molecule could be correlated with a specific orientation of the cage with respect to the substrate. However, the origin of several patterns still remain unclear, suggesting the presence of other geometric isomer or modifications due to the fullerene-substrate interaction.

The spectroscopic results reveal a strong dependence of the electronic spectra of Ce@C_{82} on the molecular orientation. The calculations suggest that this behavior is a consequence of the tunneling into the hybridized cerium-cage states. The hybrid states are partially located on the encapsulated atom and this localization affects the STS spectra. In the vibrational spectra two features corresponding to the internal C_{82} cage phonons have been identified. It has been found that the intensity of the peaks depends on the bonding configuration of the molecule, most probably due to the localization of the inelastic signal.

The presented experiments indicate that even though the encapsulated atom cannot be directly observed by STM, its presence strongly influences the properties of the molecule. To accurately analyze the spectroscopic results obtained for metallofullerenes one has to be aware of two important facts: firstly, in contrast to C_{60} some of the molecular orbitals of the endohedral fullerenes are only partially located on the cage due to the contribution from the metal atom, which may strongly affect the STS spectra; secondly also the molecule-substrate interaction may modify the electronic and vibrational structure. As we will see in the next Chapter, these two aspects will play an important role also in interpretation of the results obtained for $Ce_2@C_{80}$.

Chapter 7

Electronic and vibrational properties of $Ce_2@C_{80}$ metallofullerene

Out of the few experimental and theoretical studies devoted to the characterization of different dimetallofullerenes, hardly any refer to the $Ce_2@C_{80}$ molecule. The greatest attention has been paid to $La_2@C_{80}$ and other group II complexes [96, 106, 111, 112, 165]. The geometry of $La_2@C_{80}$ has been extensively studied and its intermolecular dynamics has been investigated [106, 111, 112]. In principle, it can be expected that the main electronic and vibrational properties of $Ce_2@C_{80}$ are similar to the properties of the La complex [96]. However, compared to La, Ce has an additional $4f$ electron which may give rise to new effects.

Interestingly, STM has been so far only rarely used to study dimetallofullerenes [151, 164]. A. Taninaka *et al.* in Ref. [151] have studied the properties of $La@C_{82}$ and $La_2@C_{80}$ on H:Si(111)2×1. STS results indicate that there is a difference in the electronic structure of the two endohedral fullerenes, in agreement with the theoretical calculations. However, a low temperature STM has been so far not used to investigate the properties of dimetallofullerenes and no high resolution spectroscopy data are available.

The previous Chapter (Chap. 6) has been focused on the $Ce@C_{82}$ metallofullerene. We have been able to determine that the electronic structure of this molecule is characterized by the presence of a singly occupied molecular orbital. In Section 3.4 it has been already explained, that substantial differences are found between $M_2@C_{80}$ and $M@C_{82}$ fullerenes. The formation mechanism of dimetallofullerenes involves the stabilization of the carbon cage by complete filling of the highest unoccupied orbital HOMO. It may be than expected, that $Ce_2@C_{80}$ is a highly stable molecule and has, in contrast to $Ce@C_{82}$, a closed shell electronic structure.

In the following part of the thesis, the properties of $Ce_2@C_{80}$ will be analyzed in detail. The elastic and inelastic spectroscopy results give insight into the electronic and vibrational structure of this complex. It will be shown that near the Fermi energy unusually large changes are observed in the differential conductance of the molecule, which

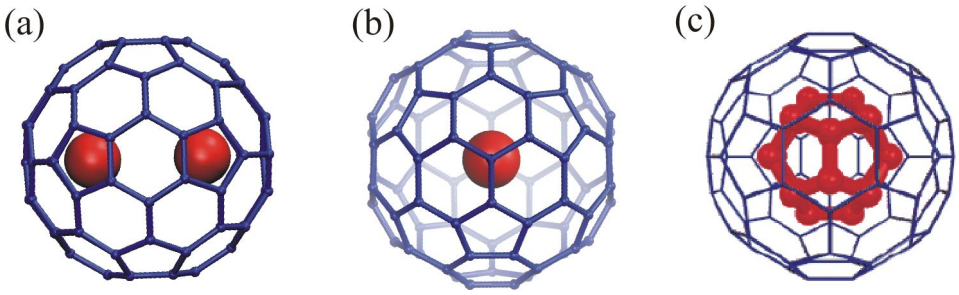

Figure 7.1: The geometry of $Ce_2@C_{80}$ molecule calculated by DFT. Cerium atoms are encapsulated on the I_h isomer of C_{80} cage and occupy D_{3d} sites. (a) and (b) Two different views of the molecule, from the main axis (a) and six-membered rings perpendicular to the main axis (b). (c) In case of $La_2@C_{80}$ the metal atoms can move freely at room temperature. The same may be expected for the cerium atoms in $Ce_2@C_{80}$. The red spheres denote the equivalent positions of the metal atoms and red bars indicate the path trough the D_{2h} saddle point.

leads to appearance of a striking feature in the dI/dV spectrum. Possible processes that may give rise to this behavior will be considered, based on the electron-phonon coupling and Kondo scattering.

7.1 Calculated geometry of $Ce_2@C_{80}$

The theoretical DFT calculations of the structure of $Ce_2@C_{80}$ are currently carried out by K. Muthukumar and J. A. Larsson at Tyndall National Institute, Cork, Ireland (for details on calculation parameters see Section 6.1). The results indicate, that the two cerium atoms are encapsulated in the I_h isomer of C_{80} carbon cage, similarly to other dimetallofullerenes [96, 112]. The most stable configuration has D_{3d} symmetry, in which the two metal atoms are located under the carbon atoms shared by the three hexagonal rings of C_{80}, as schematically shown in Fig. 7.1(a) and (b). Ten equivalent D_{3d} positions of the ceriums which are found inside the I_h-C_{80} cage can be connected along the valley of potential energy surface through the D_{2h} saddle points, which lie on the C_2 axis. The calculations predict that the potential inside the cage is very smooth and the energy difference between the D_{3d} and D_{2h} is small, in the range of ~ 50 meV. Therefore, the metal atoms can move freely around the cage at room temperature, going from one D_{3d} point to another one. As illustrated in Fig. 7.1(c), the averaged path of the atoms forms a pentagonal dodecahedron, which is also in very good agreement with x-ray diffraction data for $La_2@C_{80}$ (see Section 3.4, Fig. 3.6). This finding is in contrast to the result for $Ce@C_{82}$ metallofullerene, where the cerium atom strongly binds to the specific site inside the C_{82} cage [91].

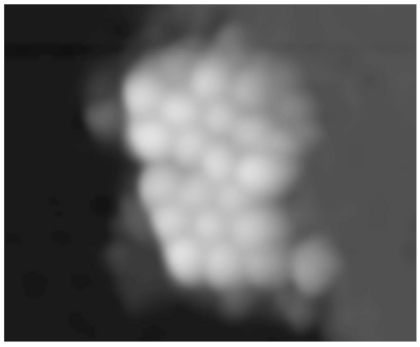

Figure 7.2: Constant current STM image of $Ce_2@C_{80}$ island on Cu(111), grown at room temperature. ($10 \times 12\,nm^2$,$I = 0.2\,nA$, $V = 0.2\,V$).

7.2 Adsorption of $Ce_2@C_{80}$ on metal surfaces

$Ce_2@C_{80}$ on Cu(111)

Deposition of $Ce_2@C_{80}$ molecules on Cu(111) at room temperature leads to the formation of islands. Similarly as in case of $Ce@C_{82}$ (see Section 6.2), the growth starts at the step edges and the arrangement of the molecules within the island is disordered. Fig. 7.2 presents a constant current STM image of $Ce_2@C_{80}$ island on Cu(111) grown at room temperature. No pronounced internal structure of the molecules has been resolved, so direct determination of orientation of the molecules with respect to the substrate has not been possible. However, the lack of order within the island suggests that, analogously to $Ce@C_{82}$, the position of $Ce_2@C_{80}$ is probably random.

Well-organized structures of dimetallofullerenes can be obtained by post-deposition annealing. Fig. 7.3(a) shows a STM image of $Ce_2@C_{80}$ on Cu(111) after short annealing at 250°C. Fullerenes bind to the step edges and form chains along the steps. The typical length of the rows have varied between four and fifteen molecules. The dimetallofullerene chains investigated in this study consist of two parallel rows, one of the them adsorbed on the narrow terrace of the width $\sim 5 - 10\,nm$. For the low submonolayer coverages used in this work no single fullerene chains have been found. The adsorption site of the molecules has been determined by measuring the linescans and comparing the apparent hight of the molecules in the chain (with respect to a particular terrace) to the apparent height of the fullerenes in the island. It has been established that the molecules are located on the lower terrace of the step edge, i.e. one fullerene row is adsorbed on the narrow terrace and another on the lowermost terrace below. Such adsorption configuration is not clear from the STM images (see Fig. 7.3(b)), where the apparent position of the step edge coincides with the apparent location of the molecules. Similar contradiction between the real adsorption side and the STM image has been observed also for C_{60} adsorbed along the steps of vicinal Au surface and has been explained by the effect of a finite tip size on the imaging of asymmetric structures [166].

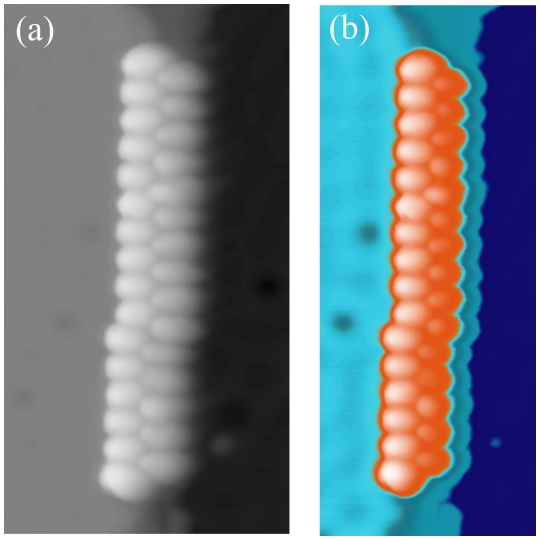

Figure 7.3: (a) Constant current STM images of $Ce_2@C_{80}$ on Cu(111) after annealing of the sample at 250°C. The fullerenes form chains along the step edges. ($19 \times 20\,nm^2$, $I = 0.5\,nA$, $V = -0.15\,V$) (b) False color representation of the same image, showing the apparent position of the step edges relative to apparent position of the molecules.

$Ce_2@C_{80}$ on Au(111)

It is well established that the interaction of fullerenes with Au(111) is weaker than on Cu(111). Therefore, in order to later investigate the influence of the substrate on the frequencies of the vibrational modes of $Ce_2@C_{80}$, the fullerenes have been evaporated on Au(111) surface. After deposition the sample has been shortly annealed (up to 250°C) so that the molecules arrange in well-ordered structures. STM images in Fig. 7.4 reveal that $Ce_2@C_{80}$ forms close-packed islands of well-ordered hexagonal structure. At low bias voltages a characteristic internal structure of the molecules has been resolved. Most of the molecules show similar patterns, which indicates the existence of a preferential bonding configuration.

7.3 Electronic spectroscopy of $Ce_2@C_{80}$

7.3.1 Photoemission spectroscopy

The electronic structure of $Ce_2@C_{80}$ has been investigated by K. Schulte *et al.* (University of Nottingham, UK) by photoemission spectroscopy. The valence band spectrum of $Ce_2@C_{80}$ thin films adsorbed on Ag:Si(111)($\sqrt{3} \times \sqrt{3}$) is presented in Fig. 7.5. The spectrum of $Ce@C_{82}$ discussed in Section 6.3.1 is given as well for comparison. The results obtained for dimetallofullerene are quite different from those obtained for $Ce@C_{82}$. The onset of the valence band for $Ce_2@C_{80}$ is located at ≈0.8 eV and no characteristic feature is present in the spectrum for the binding energies below 1 eV. In contrast, the

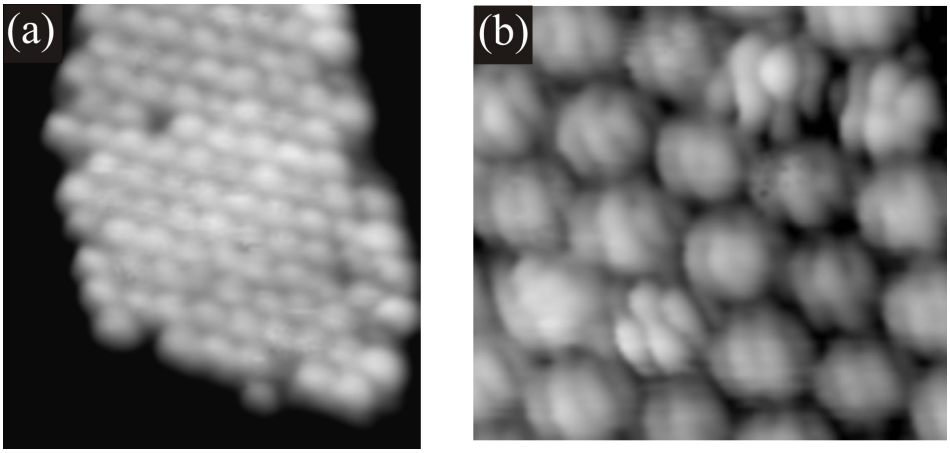

Figure 7.4: Constant current STM images of $Ce_2@C_{80}$ island on Au(111). (a) After short annealing $Ce_2@C_{80}$ on Au(111) forms close-packed hexagonal islands. ($15 \times 15\,nm^2$, $I = 0.1\,nA$, $V = -2\,V$) (b) Internal structure of the fullerenes has been resolved at low bias voltages ($V = 0.25\,V$). Similar patterns suggest that most of the molecules exhibit a preferential adsorption configuration.($5 \times 5\,nm^2$, $V = -0.25\,V$, $I = 0.1\,nA$)

spectral onset for $Ce@C_{82}$ appears at smaller binding energies ($\approx$0.3 eV) and the region near the Fermi level is dominated by the SOMO-derived band, confirming the open-shell electronic structure. The absence of the SOMO feature in the spectrum of $Ce_2@C_{80}$, as well as a deep lying onset on the valence band, indicate that dimetallofullerene has a closed-shell structure and exhibits a relatively large gap between empty and occupied states.

7.3.2 Density functional theory calculations

In order to accurately interpret the experimental STS spectra, theoretical calculations of the electronic structure of the $Ce_2@C_{80}$ molecule have been performed.

Firstly, an approximated model of the molecule has been evaluated in this work. Since it is known that valence state of cerium inside the fullerene cages is 3+, the $Ce_2@C_{80}$ molecule can be represented by the icosahedral C_{80} cage with six additional electrons. Such a model does not explicitly include the presence of Ce but can to some extent reproduce the most important features of the molecule [151, 155]. The calculations have been done on the Supercomputer JUMP (IBM p690-Cluster) in Research Center in Jülich. The density functional theory (DFT) calculations employing the PBE exchange-correlation functional have been performed, as implemented in the Turbomole system [159]. Split valence plus polarization (SVP) basis has been used for carbon atoms [167]. The influence of the substrate has not been included.

The calculated electronic structure of $C_{80}{}^{-6}$ is presented in Fig. 7.6(a). The states of the molecule are denoted by the horizontal lines. The corresponding symmetries of the

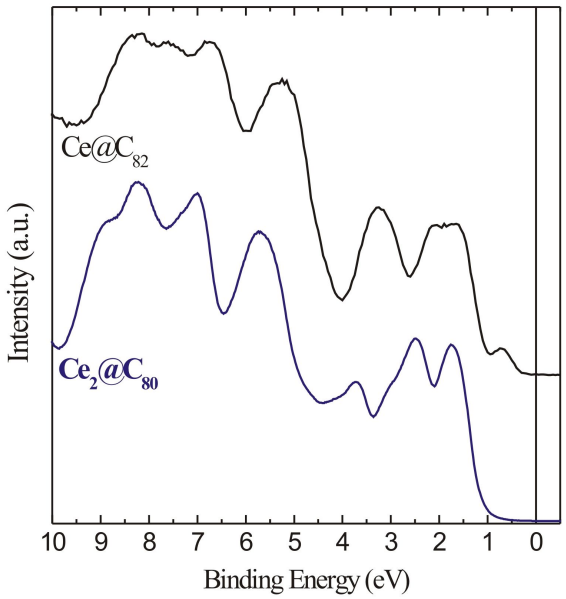

Figure 7.5: The valence band spectrum of the ordered films of $Ce_2@C_{80}$ on Ag:Si(111)($\sqrt{3} \times \sqrt{3}$) (blue line). The spectrum of $Ce@C_{82}$ is given for comparison (black line). The spectral onset for $Ce_2@C_{80}$ is observed at higher binding energies than in case of $Ce@C_{82}$, indicating a bigger HOMO-LUMO gap of dimetallofullerene. (The incident photon energy was 60 eV.) (K. Schulte *et al.*, Nottingham, UK)

states given in the plot refer to the irreducible representations of I_h group. Within this approximation the orbitals of the molecule are degenerate (the degeneracy is given in the brackets). The HOMO orbital of the $C_{80}{}^{-6}$, of g_g symmetry, is fourfold degenerate and completely occupied by the six electrons donated from the cerium atoms. The LUMO is singly-degenerate and has a_g symmetry. The results indicate that $Ce_2@C_{80}$ is a stable molecule and should exhibit a large HOMO-LUMO gap in the experiments.

However, the $C_{80}{}^{-6}$ model accounts only for the charge transfer in endohedral complexes, which is a very simplified approximation of the metal-cage interaction. In reality, the electronic properties of metallofullerenes are determined as well by the hybridization of the metal-cage orbitals. Describing the presence of cerium only by adding electrons to the cage neglects some important effects arising from cerium-cage chemical bonding. In such a simple model the extra electrons are delocalized over the whole molecule, whereas more complex calculations for the endohedral fullerenes predict localization of the charge in the vicinity of the chemisorption site [91]. Therefore, DFT results obtained for $C_{80}{}^{-6}$ cannot explain all the features resolved by STS spectroscopy (see Section 7.3.3 and 7.3.4), which indicates that the observed properties are not determined by the carbon cage but may be directly related to the presence of encapsulated atoms. For the exact interpretation of the data a complex electronic structure of $Ce_2@C_{80}$ should be considered.

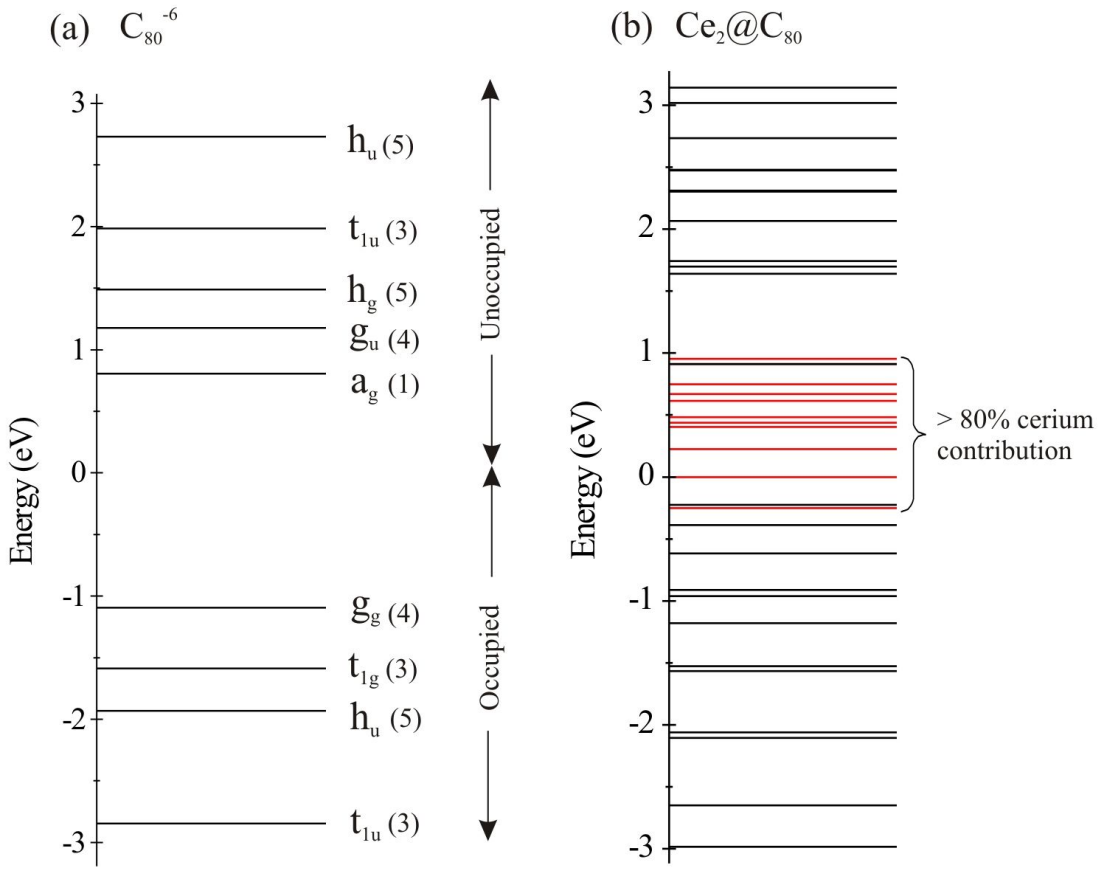

Figure 7.6: (a) Electronic structure of $C_{80}{}^{-6}$ and $Ce_2@C_{80}$ predicted by DFT calculations. (a) Electronic energy level of $C_{80}{}^{-6}$ a simplified model of the $Ce_2@C_{80}$ molecule. The h_u, t_{1g}, g_g *etc.* indicate the symmetries of the corresponding states, in term of irreducible representations of I_h point group. The degeneracy of the orbitals is given in brackets. The model predicts a closed shell structure of the molecule and a relatively big HOMO-LUMO gap. (b) Electron energy levels of $Ce_2@C_{80}$ molecule (model by K. Muthukumar *et al.*). Degeneracy of the electronic states predicted in (a) is lifted. The spectrum is dominated by the hybridized Ce-cage orbitals. The states with highest cerium contribution (mostly $> 80\%$) are marked red.

First results of the DFT calculations[1] performed for complete molecule reveal that the electronic structure of $Ce_2@C_{80}$ is much more complicated than that obtained for the $C_{80}{}^{-6}$ model. First of all, the presence of two cerium atoms reduces the I_h symmetry of the C_{80} cage to D_{3d}. In result, the degeneracy of the electronic states predicted for $C_{80}{}^{-6}$ system is lifted. Secondly, the hybridization of the metal and cage orbitals takes place, resulting in a partial Ce character of the molecular states. The energy levels of the molecule are shown in Fig. 7.6(b). The Fermi level has been aligned to the HOMO orbital. The states lying close to the Fermi level exhibit a very high cerium contribution (mostly >80%) and are dominated by the $4f$ states of the metal atoms (indicated by red bars in figure (b)). Other orbitals presented in the image are localized mostly on the C_{80} cage (black bars), however also for them a minor Ce contribution has been predicted (typically < 20%).

7.3.3 Scanning tunneling spectroscopy of $Ce_2@C_{80}$ on Cu(111)

In order to study the local electronic properties of $Ce_2@C_{80}$ on Cu(111), scanning tunneling spectroscopy measurements have been performed. Reliable and reproducible STS data have been obtained for the well-ordered fullerene rows adsorbed along the steps (see Fig. 7.3(b)). STS spectrum measured over a $Ce_2@C_{80}$ chain is presented in Fig. 7.7(a). Clear peaks that appear in the spectrum can be attributed to the molecular resonances. Two features dominate the occupied part of the spectrum: a peak located at -1 ($\pm$0.1) V (H_0) and a peak centered at -1.6 ($\pm$0.1) V (H_1). In the empty states part of the spectrum three features are resolved, centered at 0.7 ($\pm$0.1) V, 1.6 ($\pm$0.1) V and 2.3 ($\pm$0.2) V. In the following, these features will be referred to as L_0, L_1 and L_2, respectively.

The HOMO-LUMO gap determined from the measurements, defined as a energy distance between the peaks H_0 and L_0, is of the order of $1.5 - 1.7$ eV. This relatively large value, compared to $Ce@C_{82}$ (see Section 6.3.3) is due to the high stabilization of C_{80} cage by the charge transfer from cerium atoms. The results are also in qualitative agreement with the STM study of $La_2@C_{80}$ [151].

In order to establish the origin of the STS features the calculated electronic structure of $Ce_2@C_{80}$ (Fig. 7.6(b)) has been considered. The DOS of the molecule obtained by DFT is presented in Fig. 7.7(b). As discussed in the previous section, the electronic states of $Ce_2@C_{80}$ are partially localized on cerium atoms. The calculations predict that the energy region near the Fermi level, in particular the first unoccupied states, is dominated by the highly localized $4f$ orbitals of the cerium atoms (red bars in Fig. 7.7(b) and Fig. 7.6(b)). It may be expected that, since only minor part of the orbital is located on the carbon cage (less than 20%), these states are difficult to detect experimentally by tunneling spectroscopy. The density of states spectrum (continuous line in the plot) has been generated by gaussian broadening with $FWHM = 0.2eV$, however the states with high Ce contribution, mentioned above, have been excluded. The comparison with the tunneling spectrum in (a) confirms that such model reproduces relatively

[1] K. Muthukumar and J.A. Larsson, Tyndall National Institute, Cork, Ireland

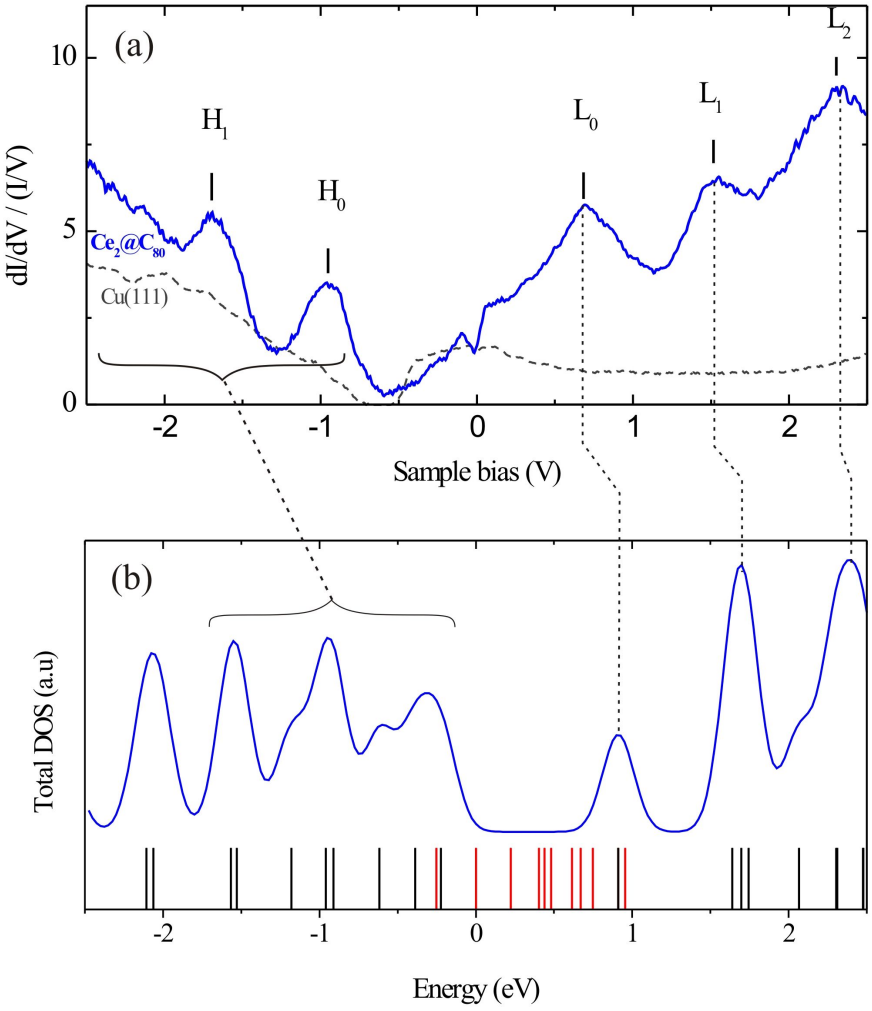

Figure 7.7: (a) Electronic structure of $Ce_2@C_{80}$ of a fullerene chain measured by STS. The features referred to in the text are indicated by H_0, H_1 and L_0 - L_2. (Tunneling parameters: $V = 2.5\,\mathrm{V}$, $I = 0.4\,\mathrm{nA}$, $V_{mod} = 10\,\mathrm{mV}\,(\mathrm{rms})$) (b) Density of states of $Ce_2@C_{80}$ calculated by DFT (calculations by K. Muthukumar *et al.*). Vertical lines denote the molecular orbitals, the colored bars correspond to the states with high Ce contribution (red bars in Fig. 7.6(b)). The DOS spectrum has been generated by gaussian broadening. Only the states with minor Ce contribution have been considered (marked black in Fig. 7.6(b)). The proposed correspondence between the STS and DFT spectra is indicated by dotted lines.

well the features resolved by STS. The proposed assignment of the peaks is indicated in the figure. DFT calculations underestimate the spacing between the occupied and unoccupied states and the calculated distance between the features corresponding to H_0 and L_0 is lower then that measured experimentally.

Feature L_0 resolved in the STS spectrum is characteristically broadened on one side and its edge crosses the Fermi level. Two effects may be responsible for the observed broadening. Firstly, it is possible that the states derived from the $4f$-orbitals of Ce still contribute to the tunneling, however, with much lower tunneling rate than the cage-related states. This contribution may modify the STS spectrum of $Ce_2@C_{80}$ and give rise to a non-zero dI/dV signal near the Fermi level. Secondly, the broadening may be caused also by the charge transfer into the empty orbitals of the molecule. The fact that the interaction with the substrate may alter the STS spectrum near E_F has been discussed for C_{60} molecule, for which broadening and splitting of the LUMO has been observed (see Section 5.4).

One more striking feature appears in the STS spectrum: the sharp dip directly at the Fermi level. The calculations of the electronic structure do no provide any explanation regarding the origin of this feature. As we will see later, its presence is correlated with the excitation of the molecular vibrational modes. The detailed discussion of the effects that may account for the presence of the dip at E_F will be discussed in Section 7.5.

7.3.4 Mapping of electronic states of $Ce_2@C_{80}$

The analysis of the STS data obtained for different fullerenes within one chain reveals that for particular molecules modifications in the unoccupied states are observed. The two types of electronic spectra are compared in Fig. 7.8. The difference between the curves appears in the unoccupied states, in the bias range $\sim 0.5-1.2\,\mathrm{V}$. In spectrum B, similar to the one discussed above, one feature L_0 is resolved in the mentioned voltage range. In contrast, spectrum A exhibits two peaks, L' and L'', at $0.5\,(\pm 0.06)\,\mathrm{V}$ and $1\,(\pm 0.1)\,\mathrm{V}$, respectively. The remaining peaks are similar for both plots and are located at almost the same positions as features H_0, H_1 and L_1, L_2, analyzed in previous section. The characteristic dip at E_F is also observed in both spectra. The only additional difference appears for the features denoted as H_1 and H_1'. The detailed analysis of the STS spectra obtained with different tips has shown that sometimes a double peak appears in this region, which suggests the features H_1 and H_1' correspond to different electronic states.

Observation of two characteristic STS spectra is most probably related to the presence of two different bonding configurations of $Ce_2@C_{80}$. In the following text, the metallofullerenes which exhibit a particular kind of spectrum will be referred to as molecules of type A and B. Remarkably, in constant current STM images all molecules look exactly the same, as featureless protrusion (Fig. 7.9(b)). The internal structure and the differences between the molecules becomes clear only in the spectroscopic imaging mode. Differential conductivity maps have been acquired for all spectral features resolved by STS. The results are presented in Fig. 7.9. Image (b) shows a constant current topograph of a double fullerene chain. Colored dots denote the A-type (red) and

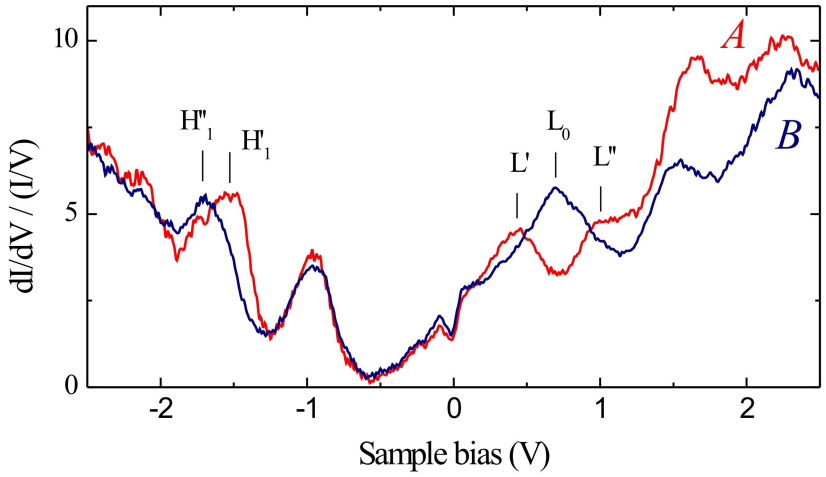

Figure 7.8: Two types of STS spectra measured for different $Ce_2@C_{80}$ molecules within one chain. The difference occurs in the unoccupied part of the spectrum, the related states are marked in the graph. The spectrum showing features L' and L'' is denoted as A, the spectrum exhibiting peak L_0 is marked as B. (Tunneling parameters: $V = 2.5\,\mathrm{V}$, $I = 0.4\,\mathrm{nA}$, $V_{mod} = 10\,\mathrm{mV}\,(\mathrm{rms})$)

B-type (blue) molecules, distinguished according to the spectroscopic signal. Images (c)-(f) correspond to the dI/dV maps of the same chain at the energies corresponding to the features H_1/H_1', H_0, L_0/L' and L_1, respectively. The related peaks are marked in the STS spectrum in (a).

Each map shows two different molecular patterns, confirming the presence of two kinds of species within the chain. Spectral map of the states H_1 and H_1' (image (c)) reveals a characteristic nodal plane, present for all the fullerenes. However, the maximum of the electron density is localized either in the left side side of the image (type A) or is shifted to the right (type B) (indicated by arrows in the image). The differences between the A- and B-type fullerenes can be observed as well in the dI/dV images of states H_0 (map (d)), L_0/L' (map (e)) and L_2 (map (f)). Spatial distribution of the feature H_0 (map (d)) is characterized by the presence of two dark spots within the molecule. For the fullerenes of type B the two spots can be easily distinguished, one observed on the right side and one on the left. In case of the molecules of type A, both spots can be seen in the left part of the molecule: one of them seen clearly, the second hardly visible at the edge of the cage. Surprisingly, the spectral map of the resonances L_0 and L' (map (e)) is not significantly different from H_0. The two dark spots are still observed, superimposed on the bright-dim structure. Finally, most of the bright features in the map of L_0 (map (e)) appear dark in L_1 (map (f)).

To summarize the discussion, the STS results and energy-resolved maps of the elec-

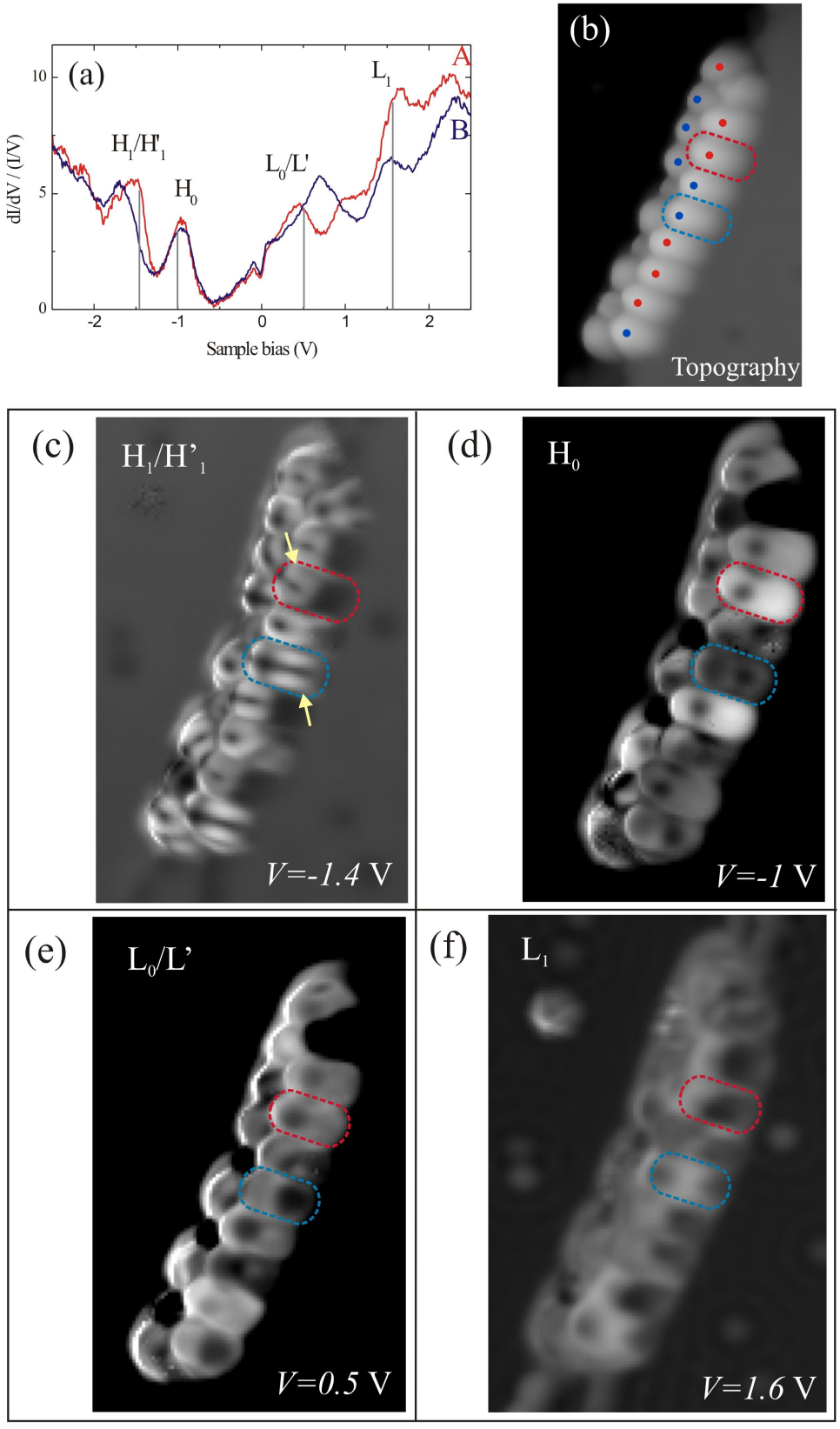
(a)
A
B
L_1
H_1/H'_1
L_0/L'
H_0
dI/dV / (I/V)
Sample bias (V)
(b)
Topography
(c)
H_1/H'_1
V=-1.4 V
(d)
H_0
V=-1 V
(e)
L_0/L'
V=0.5 V
(f)
L_1
V=1.6 V

tronic states allow to distinguish between two different bonding geometries of $Ce_2@C_{80}$. The bonding site, i.e. the fact whether the fullerene is adsorbed on the narrow terrace or the wide terrace, seems to have no influence on the electronic spectra, since both A and B molecules are observed in each row. The most obvious conclusion is then that two preferential orientations of the $Ce_2@C_{80}$ molecule are present within the chain. It is remarkable that the changes in the STS spectra appear in the energy region where also highly localized cerium-derived orbitals are expected. The differences in electronic structure may be then related to a different positions of encapsulated cerium atoms with respect to the substrate. Interestingly, the differential conductivity maps of $Ce_2@C_{80}$ do not show typical characteristic features of the cage orbitals. Especially striking observation is the presence of the two dark spots in the spectroscopic images of H_0 and L_0/L' (Fig. 7.9(d) and (e)). It is tempting to correlate these spots with the encapsulated ceriums. According to the calculations, all the molecular states in the considered energy window exhibit a partial cerium character. Therefore, the cerium atoms may directly affect the observed spatial distribution of the dI/dV maps. However, it is so far not clear why the presence of the metal atoms would manifest itself as dark spots and such correlation cannot be satisfactory proved.

7.4 Vibrational spectroscopy

The dip-shaped feature resolved by STS spectra near the Fermi level appears in the bias region where usually also vibrational excitations of the molecule are observed. The careful analysis of the spectroscopic data reveals that there exists a correlation between the dip in dI/dV and the vibrational peaks resolved by IETS spectroscopy. This suggests that some interesting effects may occur in case of inelastic tunneling through $Ce_2@C_{80}$. Therefore, the vibrational properties of the molecule have been studied in detail for different adsorption conditions. The inelastic spectra have been measured for molecules adsorbed on Cu(111) and Au(111) and the influence of the bonding properties on the vibrational modes has been investigated.

Figure 7.9 *(on the next page)*: (a) STS spectra of type A and B recorded for the molecules of the chain. The relevant features are indicated in the graph. (b) Constant current topograph of the fullerene chain. ($12 \times 7\,\mathrm{nm}^2$). (c)-(f) Energy-resolved dI/dV maps of the chain. The maps have been acquired at bias voltages $V = -1.4\,\mathrm{V}$ (e), $V = -1\,\mathrm{V}$ (d), $V = 0.5\,\mathrm{V}$ (e) and $V = 1.6\,\mathrm{V}$ (f), and correspond to the STS features denoted as H_1'/H_1'', H_0, L_0/L' and L_2, respectively. For convenience, the examples of the molecules of type A (red) and B (blue) has been indicated by circles. The arrows in image (c) denote the characteristic feature discussed in the text.

7.4.1 Inelastic tunneling spectra of $Ce_2@C_{80}$

$Ce_2@C_{80}$ on Cu(111)

STM images of $Ce_2@C_{80}$ adsorbed on Cu(111) show that, depending on the deposition conditions, molecules form on the surface disordered islands or double chains along the step edges (see Figs. 7.2 and 7.3). STM-IETS spectra of $Ce_2@C_{80}$ have been measured for metallofullerenes of both structures.

Let us first focus on the results obtained for the islands. Fig. 7.10 presents vibrational spectra obtained for different molecules within one island. The curves reveal several vibrational excitations of $Ce_2@C_{80}$. The spectrum observed most commonly is shown in Fig. 7.10(a). It exhibits two pronounced peaks in the positive voltage, with the counterpart dips in the opposite polarity. The features, located at $6\,(\pm1)$ mV and $60\,(\pm1)$ mV, are repeatedly observed in the vibrational spectra of most of the molecules. Both features indicate excitation of a vibrational mode of $Ce_2@C_{80}$. In the remaining part of the text they will be referred to as modes ν_1 and ν_2, respectively. Peak ν_2 is clearly distorted from the expected gaussian shape and is broadened on one side. The broadening suggests the presence of additional vibrational modes, which are not resolved from each other due to too low resolution. Indeed, inelastic spectra on several molecules confirm that apart from ν_1 and ν_2 also other vibrations of $Ce_2@C_{80}$ are excited. The curves in Fig. 7.10(b) resolve additional peaks located at $23\,(\pm1)$ mV and $37\,(\pm1)$ mV. For a limited number of molecules also a mode at $51\,(\pm2)$ mV has been detected, however then the characteristic strong peak at 60 mV has not been present (Fig. 7.10(c)). Altogether, vibrational modes of five different frequencies have been observed. The number of detected modes is relatively high, compared to the IETS data reported so far for other fullerenes [122, 140, 155]. It is also remarkable, that particular molecules exhibit so different spectra. In contrast, for differently oriented $Ce@C_{82}$ only change in the intensity of the peaks has been observed (see Section 6.4). However, there seems to be no direct correspondence between the differences inelastic spectra and modifications in the electronic structure, discussed in the previous section.

The spectra measured for the disordered $Ce_2@C_{80}$ islands have been compared to the IETS results obtained for the fullerenes adsorbed in the chains along the step edges. Typical spectra recorded over a fullerene chain are shown in Fig. 7.11. Similarly as in case of the islands, all of the curves exhibit two pronounced peaks, however this time the features are located at $9\,(\pm1)$ mV, and $66\,(\pm1)$ mV. For some molecules also features at $28\,(\pm2)$ mV (spectra (b) and (c)), $37\,(\pm2)$ mV (spectrum (b)) and $49\,(\pm2)$ mV (spectrum (c)) have been detected. All these peaks exhibit a correlated dip in the opposite polarity and can be assigned to vibrational modes of $Ce_2@C_{80}$.

The fact that the spectral patterns of molecules of the chains and the molecules of the island are almost identical suggests that probably the same vibrations are excited in both cases. The series of spectra presented in Figs. 7.10 and 7.11 are dominated by two peaks (denoted as ν_1 and ν_2 in Fig. 7.10(a)), only the frequencies measured for fullerene chain are shifted, compared to the results obtained for the islands. Based on the similarity of the curves we can correlate the features resolved for $Ce_2@C_{80}$ chains at

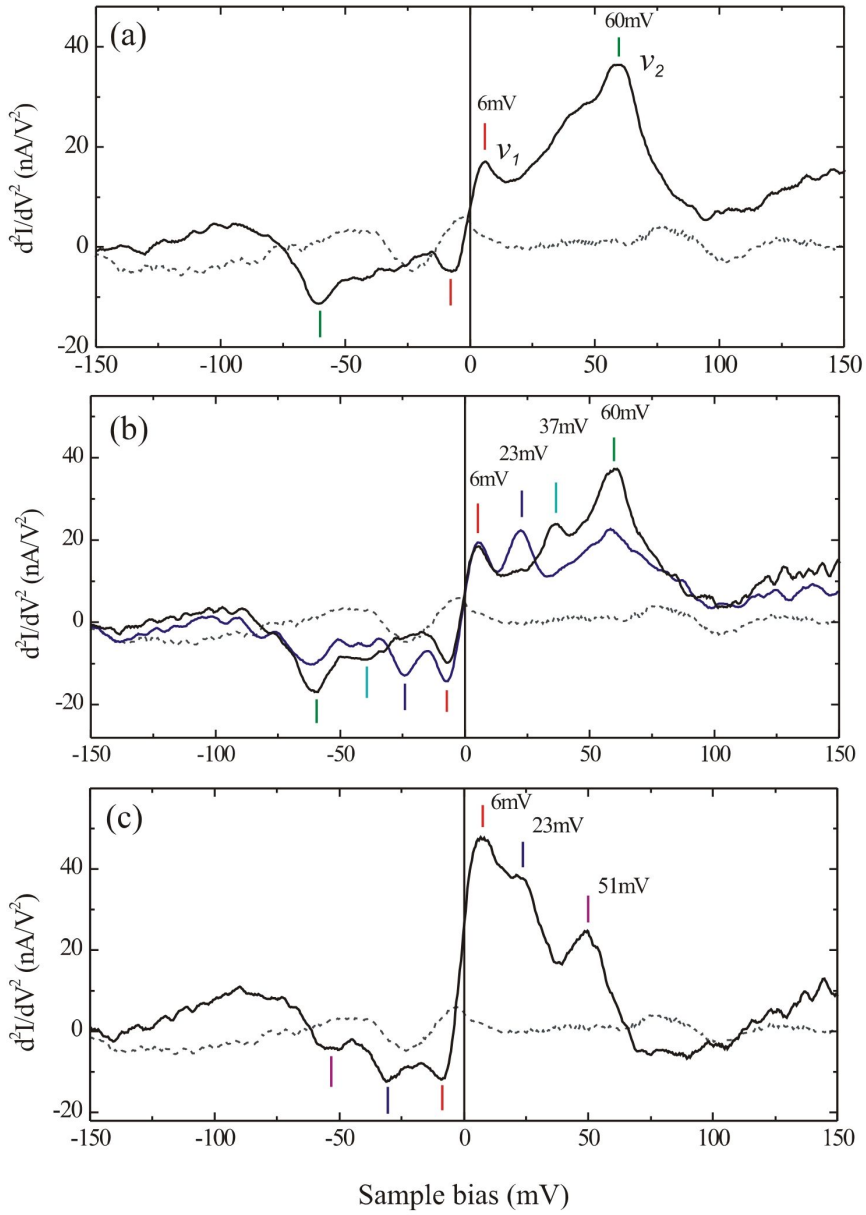

Figure 7.10: STM-IETS spectra measured for disordered islands of $Ce_2@C_{80}$ on Cu(111). Different vibrational modes have been resolved for different molecules. Altogether five modes have been detected, at bias voltages 6 mV, 23 mV, 37 mV, 51 mV and 60 mV, as marked in the graphs. (Tunneling parameters: V =200 mV, I =0.5 nA, V_{ac} =6 mV (rms))

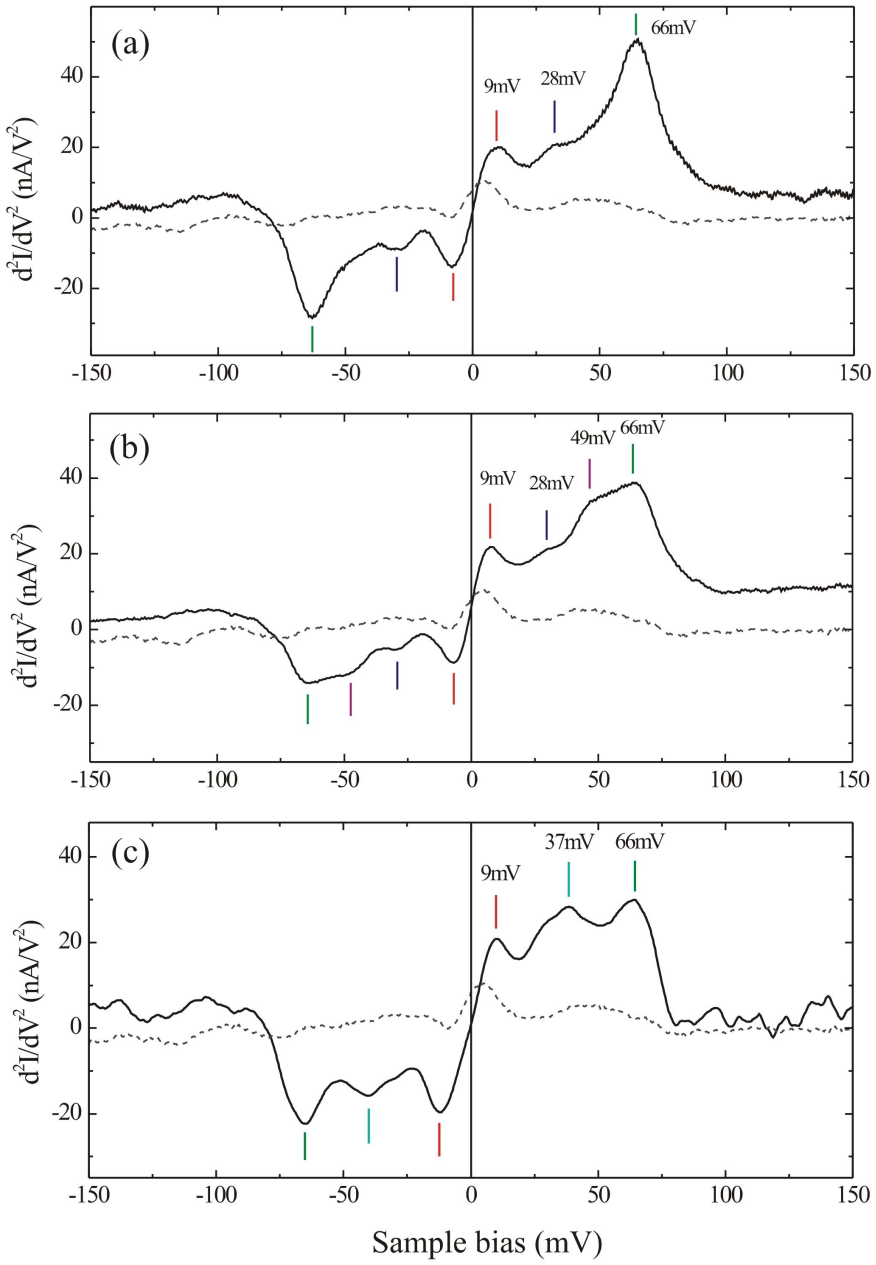

Figure 7.11: STM-IETS spectra measured for ordered $Ce_2@C_{80}$ chains on Cu(111). Five different peaks at bias voltages 9 mV, 28 mV, 37 mV, 49 mV and 66 mV (indicated in the plots) correspond to the vibrational modes of $Ce_2@C_{80}$. Compared to the spectra of disordered islands, most of the modes are shifted to higher energies. (Tunneling parameters: $V = 150\,\mathrm{mV}$, $I = 0.5\,\mathrm{nA}$, $V_{ac} = 6\,\mathrm{mV}$ (rms))

9 mV and 66 mV with the modes ν_1 and ν_2 resolved at 6 mV and 60 mV for the fullerene islands. Upon annealing the modes move to higher energies, mode ν_1 shifts by ∼3 mV and mode ν_2 by ∼6 mV. It is also probable that other peaks detected for the chain (Fig. 7.11) can be related to the features resolved for the island (Fig. 7.10), namely feature at 37 mV (island) corresponds to 37 mV (chain) and peak at 51 mV (island) to one at 49 mV (chain). The frequency shift is most likely due to different bonding properties of the fullerenes, because annealing of the sample modifies the molecule-substrate interaction. It is well known that the vibrational frequencies shift upon chemisorption and such effect can be expected also in case of fullerenes [135, 145].

$Ce_2@C_{80}$ on Au(111)

The results presented above indicate that bonding properties of the molecule can strongly affect the vibrational frequencies. The substrate-molecule interaction is also one of the factors that determines the selectivity of vibrational modes in STM-IETS. It has been observed in case of C_{60} that different modes are resolved by STM depending on the substrate [121, 122, 140] (see also discussion in Section 5.5).

In order to determine the influence of the substrate on vibrational spectrum of $Ce_2@C_{80}$, the measurements have been performed additionally on Au(111). In case of gold, the fullerene-surface bond is expected to be weaker than on copper (see Section 5.2). IETS spectra for $Ce_2@C_{80}$ on Au(111) have been recorded over close-packed metallofullerene islands, described in Section 7.2. The inelastic spectrum, presented in Fig. 7.12, shows no significant differences compared to the results obtained on Cu(111). The overall shape of the curve is similar to the one presented before (see Fig. 7.10(a) and Fig. 7.11(a)), which means that most probably the same vibrational modes are active on both substrates. The peaks corresponding to vibrational excitations ν_1 and ν_2 are on Au(111) located at 8 (±1) mV and 64 (±1) mV, respectively. Feature ν_2 is broadened on one side and exhibits two small 'kinks' on the shoulder, indicating that at least two additional vibrational modes are present. The 'kinks' are located at 35 (±2) mV and 50 (±2) mV, which closely corresponds to the energies of the modes resolved on Cu(111) (e.g. see Fig. 7.11(b) and (c)). Relative to the results obtained for $Ce_2@C_{80}$ chain on Cu(111) (Fig. 7.11), the features on Au(111) are slightly downshifted (apart from the 50 mV mode). The frequency shift indicates the modification of the fullerene-substrate bonding.

7.4.2 Interpretation of the spectral features

The assignment of the features resolved in the vibrational spectra to the particular modes of $Ce_2@C_{80}$ is a difficult task, because no experimental reports on vibrational properties of this molecule have been published so far. The origin of the IETS feature will be then discussed based on the DFT calculations [2]. It is also reasonable to assume that the vibrational structure of $Ce_2@C_{80}$ should not be significantly different from

[2] K. Muthukumar and J.A. Larsson, Tyndall National Institute, Cork, Ireland

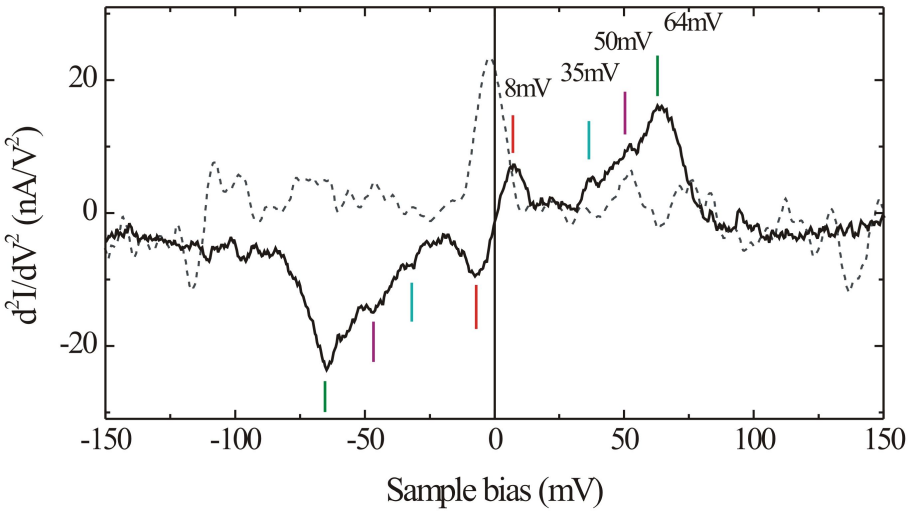

Figure 7.12: STM-IETS spectrum measured for close-packed $Ce_2@C_{80}$ islands on Au(111). Features located at 8 mV, 35 mV, 50 mV and 64 mV have been assigned to molecular vibrations. Compared to the spectra of the fullerene chains of Cu(111), the modes are slightly downshifted. (Tunneling parameters: $V = 200$ mV, $I = 0.5$ nA, $V_{ac} = 6$ mV (rms))

$La_2@C_{80}$ [106, 111], since the vibrational modes of metallofullerenes follow the mass scaling law [105, 108].

According to the calculations, $Ce_2@C_{80}$ exhibits 160 distinct vibrational frequencies, lying between $10 - 200$ meV. The symmetries of the vibrational modes are following: A_{1g}, A_{1u}, A_{2g}, A_{2u}, E_u and E_g. The modes of symmetries $E_{g/u}$ are doubly degenerate, whereas the modes of symmetries $A_{1/2}$ are singly degenerate. The model predicts that the internal vibrations of C_{80} cage have energies above 27 meV. This value is in agreement with the IR and Raman studies of $La_2@C_{82}$ and $Ti_2@C_{80}$, which resolve the internal phonons of C_{80} cage above 20 meV [106, 111]. Out of the 160 modes of $Ce_2@C_{80}$, six involve the movement of the cerium atoms. The expected energies and symmetries of these modes are listed in Table 7.1. Modes f_1 and f_2 (11 meV and 12 meV) correspond to the vibrations of the Ce-Ce unit in directions perpendicular to the Ce-locating axis. Modes f_3 and f_4 (19 meV and 23 meV) involve the movement of Ce parallel to the axis.

Based on the calculations, the IETS feature ν_2 can undoubtedly attributed to one of the internal vibrations of the C_{80} cage. The calculations predict several cage phonons in this energy range, two of them with high IR intensity, one involving also strong stretching of Ce-C bonds. The peaks resolved between 30 meV and 50 meV probably correspond as well to the cage mode but may possibly involve the Ce-C bond stretching. The origin of the experimental features below 30 meV is not clear. Since the calculations predict also cerium vibrations in this energy range, they may correspond to either to

No.	f_1	f_2	f_3	f_4
Energy (meV)	11	12	19	23
Symmetry	E_g	E_u	A_{1g}	A_{2u}
Degeneracy	2	2	1	1

Table 7.1: List of the calculated vibrational modes of $Ce_2@C_{80}$ involving the movement of the cerium atoms.

one of the cage phonons or to the vibrations of the metal atoms. The mode resolved by IETS at 23 mV has actually lower energy than the calculations predict for lowest cage mode, but it may still correspond to a pure C_{80} phonon redshifted due to adsorption. One also has to remember that DFT typically overestimates the vibrational frequencies. However, even taking into account a reasonable frequency shift, the position of the mode ν_1 is still much too low to be explained by the cage vibrations and it is clear that this mode must have some other origin.

The first obvious assumption is that mode ν_1 involves the movement of cerium atoms. The calculated energies of the vibrations f_1 and f_2 of the metal atoms (11 meV and 12 meV) agree very well with the position of the feature ν_1 (6-9 mV, depending on the system). The slight difference in energy may be due to the chemisorption effects or the overestimation of the calculated frequencies. Also another possibility has to be taken into account. In the low frequency part of the spectrum also a molecule-substrate vibrational mode can be expected. Such mode would involve the movement of whole fullerene against the metal surface. Park *et al.* have reported a strong coupling of the fullerene-surface oscillations to the tunneling electrons in a single C_{60} molecular transistor [168]. The energy of the mode, determined to be ≈ 5 meV, lies in a similar energy range as the feature ν_1. However, the molecule against the substrate vibration has not been so far observed by STM-IETS in case of fullerenes. No such feature has also appeared in the vibrational spectra of C_{60} and $Ce@C_{82}$ measured in this work. The substantial feature that distinguishes $Ce_2@C_{80}$ from the other considered fullerenes is the encapsulation of two metal atoms. It is therefore reasonable to relate the appearence/absence of the peak ν_1 to the presence of two ceriums. However, it should be stressed that based on the measurements a definite determination of the origin of this feature is not possible and both explanations should be considered.

7.4.3 Mapping of the inelastic signal

More information about the mechanism of vibrational excitation can be gained from the energy-resolved mapping of the inelastic signal. The d^2I/dV^2 spectroscopic images have been frequently used to study the nature of the excitation mechanism [7, 54, 122, 155]. The maps often reflect the shapes of particular molecular orbitals and point out the resonance that actively contributes to the vibrational excitation. Pascual *et al.* in Ref. [122] have shown that d^2I/dV^2 map of C_{60} on Ag(110) acquired at bias voltage corresponding to the vibrational mode resembles the spatial distribution of

LUMO orbital, which reveals active role of this resonance in the excitation mechanism. Localization of the inelastic signal has been reported also for $Gd@C_{82}$ metallofullerene [155], originating from the strong spatial localization of molecular electron-phonon coupling.

To study the origin of the excitation process in $Ce_2@C_{80}$, the dI/dV and d^2I/dV^2 maps have been simultaneously acquired using the lock-in technique. Fig. 7.13 shows the results obtained for one of the fullerene chains on Cu(111). For all the molecules a similar IETS spectrum has been measured (Fig. 7.13(a)), showing the pronounced ν_1 and ν_2 modes, plus additional vibrational feature at $\approx 28\,\mathrm{mV}$. In the constant current topograph (image (b)) all the molecules look like smooth protrusions. The internal pattern becomes clear in the dI/dV and d^2I/dV^2 spectroscopic images. The dI/dV map presented in (c), acquired at the bias voltage corresponding to mode ν_2, reveals that the signal is localized in the middle and at the edges of the cage, forming a characteristic stripped structure. The pattern however does not correspond to the spatial dependence of any of the electronic features imaged in Fig. 7.9. Images in (d)-(f) reflect the spatial distribution of the inelastic signal. Let us first consider the d^2I/dV^2 map acquired at 65 mV (image (e)), corresponding to feature ν_2. The presence of a clear pattern indicates that the excitation process is localized. It is striking that the regions of the strong inelastic signal correspond almost exactly to the areas of high dI/dV signal (map (b)). Similar effect can be observed also for the d^2I/dV^2 map of mode ν_1 (map (d)), recorded at 8 mV. The resemblance is not as clear as in case of map (e), however the localizations of the dI/dV and inelastic signals are undoubtedly correlated. The structure is not present in the reference image (f), acquired away from the vibrational peaks at bias voltage 120 mV.

Usually, the dI/dV map is referred to as a spatial distribution of the local density of states. Such interpretation may be not completely justified in case of the map acquired at 65 mV (map (c)), given a strong contribution from the inelastic channel at this bias voltage. However, the same dI/dV pattern has been observed at the bias voltage away from the vibrational excitations (120 mV), therefore, we will still assume that the map (c) is related to the electronic structure of the molecule near the Fermi level. The d^2I/dV^2 maps (images (d) and (e)) reveal that the vibrational signal of $Ce_2@C_{80}$ is localized. However, the recent study of M. Grobis *et al.* has shown that the localization of the inelastic signal does not necessarily correspond to the atomic displacement characteristic for the given mode but rather reflects the spatial dependence of the electron-phonon coupling [155]. The similarities between the dI/dV and d^2I/dV^2 maps indicate then that the molecular phonons of $Ce_2@C_{80}$ strongly couple to the electronic state of the molecule near E_F. The strong correlation between the excitation of vibration and differential conductance of $Ce_2@C_{80}$ is also the topic of the next section.

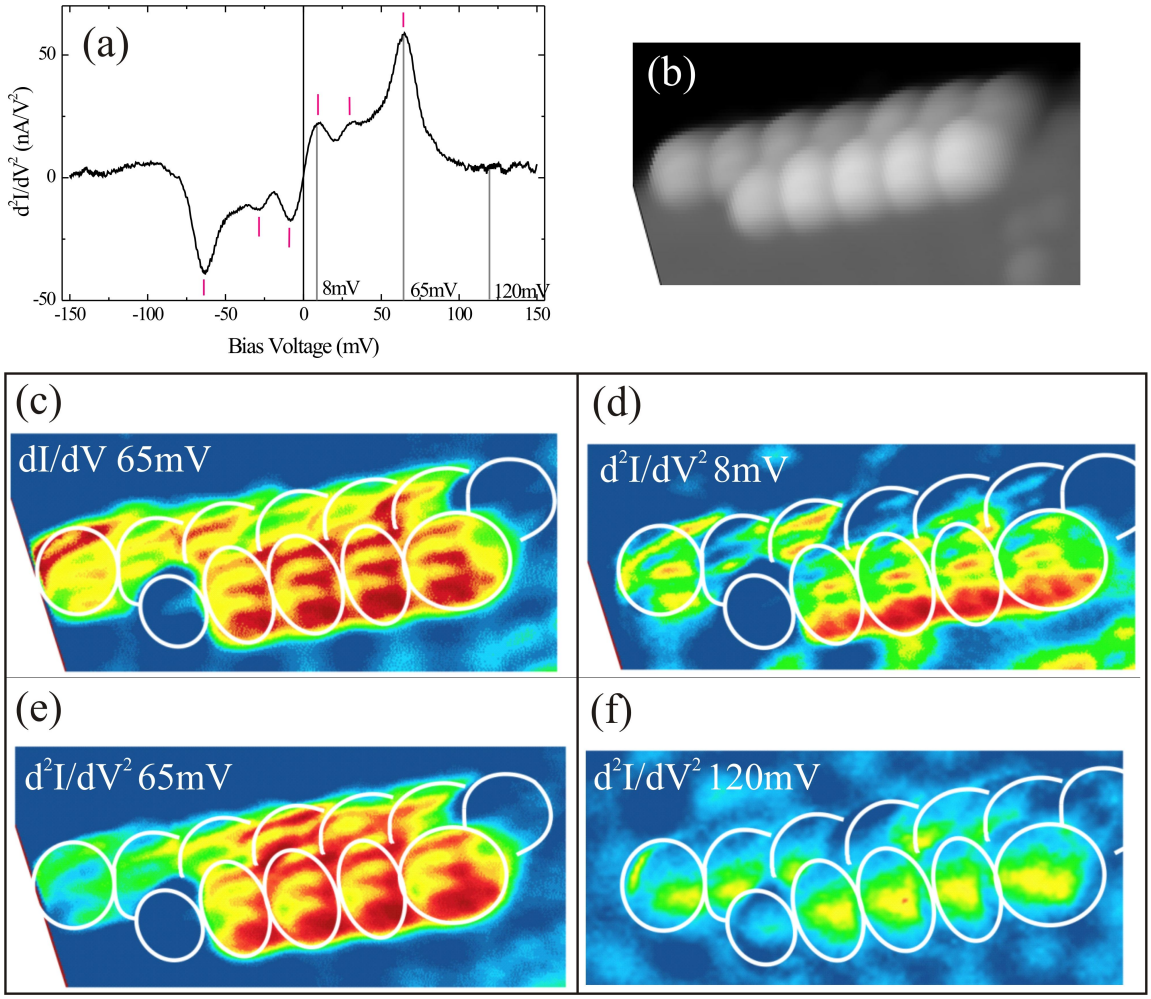

Figure 7.13: Spatial maps of d^2I/dV^2 signal for $Ce_2@C_{80}$ chain on Cu(111). (a) IETS spectrum of the molecules. The bias voltages used for spectroscopic imaging are indicated by grey lines. (b) Constant current topograph of the fullerene chain. ($5 \times 10\,\mathrm{nm}^2$, $V = 65\,\mathrm{mV}$, $I = 0.5\,\mathrm{nA}$). (c) Spatial map of dI/dV signal of the same area, at bias voltage $V = 65\,\mathrm{mV}$. (d)-(e) Maps of the inelastic signal. Maps have been acquired at bias voltages $V = 8\,\mathrm{mV}$ (d) and $V = 65\,\mathrm{mV}$ (e) corresponding to the pronounced vibrational features in spectrum (a). (f) Reference map of d^2I/dV^2 signal at $V = 120\,\mathrm{mV}$. In images (c)-(f) individual molecules are highlighted by circles.

7.5 Differential conductance of $Ce_2@C_{80}$ near the Fermi level

7.5.1 Intramolecular electron-phonon coupling

It has been already mentioned before that the sharp dip resolved by STS in Figs. 7.7(a) and 7.8 corresponds to the region where also vibrational features are observed. In the following part the influence of the excitation of vibrations on the differential conductance of the molecule will be discussed in detail.

The dI/dV and d^2I/dV^2 spectra of $Ce_2@C_{80}$ are plotted together in Fig. 7.14. The signals have been acquired simultaneously using the lock-in technique. In the dI/dV spectrum the striking dip feature around E_F is resolved. The comparison of the two curves clearly shows that the dip is occurs in exactly the same bias window in which also inelastic excitations are observed. In the region where no modes are excited, also no significant changes in the differential conductance are measured. Such correspondence between the two spectra has been observed for both Cu(111) and Au(111) substrates, regardless of the number and energies of modes observed in the inelastic spectrum.

It can be easily noticed that the excitation of vibrations of $Ce_2@C_{80}$ is accompanied by a huge increase in the differential conductance. The cross section for inelastic excitation can be estimated by calculating the normalized change in the differential conductance, defined as $\Delta\sigma/\sigma$, where $\sigma = dI/dV$ [51]. This value can be determined by integrating the area of the peak corresponding to a particular vibrational mode and dividing it by the value of conductance before the excitation. Typically, the modification of the conductance is small, of max 5-10%. However, calculation of $\Delta\sigma/\sigma$ for $Ce_2@C_{80}$ yields unusually high values. For the features ν_1 and ν_2 it gives $\Delta\sigma/\sigma(\nu_1) = 15 - 20\%$ and $\Delta\sigma/\sigma(\nu_2) = 30 - 40\%$. For other modes resolved in the spectrum, the typical values are in the usual range $\Delta\sigma/\sigma = 5 - 15\%$. It should be also noted that over the whole voltage range, for which the inelastic excitations occur, the differential conductance increases by the factor of two. This drastic change in conductance is rather puzzling, taking into account the fact that such high values have not been reported so far for any molecules.

From Fig. 7.14 it is clear that the dip observed in the dI/dV spectrum of $Ce_2@C_{80}$ has some peculiar shape. In order to demonstrate that the vibrational excitations can be indeed responsible for the characteristic structure of the dip, the data have been fitted with the IETS equations, derived in Section 2.4. The IETS equations describe the influence of the excitation of vibration on the current-voltage characteristic of the tunneling junction. In Section 2.4 it has been shown that the opening of the inelastic channel induces a step-like increase in the differential conductance curve and leads to the occurrence of peak and dip in the d^2I/dV^2 signal. The thermal broadening and position of these features can be explained by considering the Fermi-Dirac distributions of tip and sample, treating electron-molecule interaction as a parameter. The dI/dV curve can be then described by Eq. (2.16) and (2.17).

The formula (2.17) has been modified to describe the excitation of three different

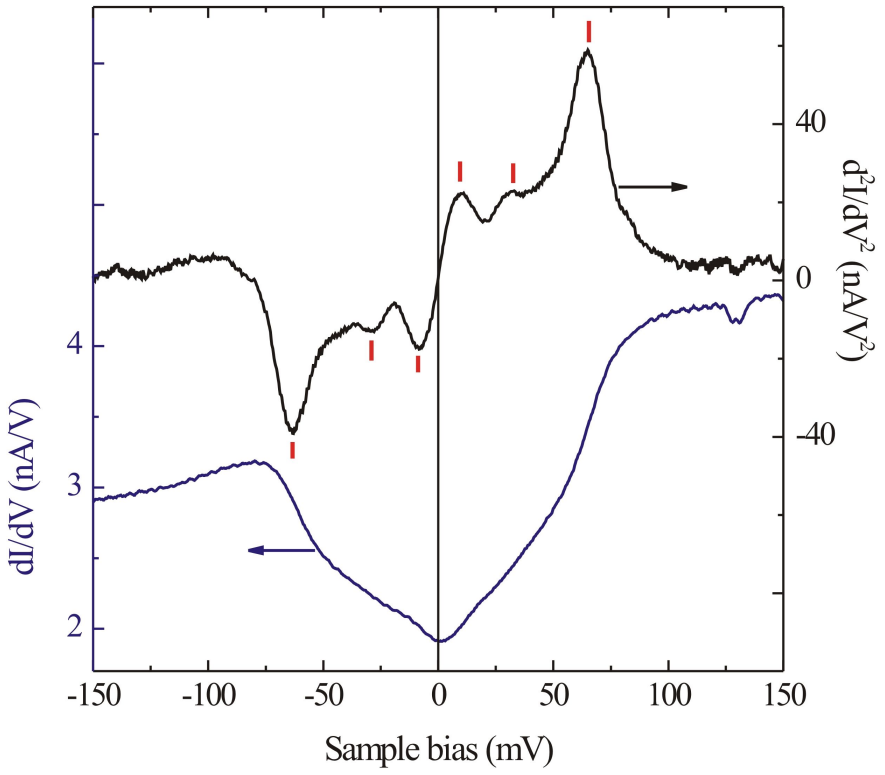

Figure 7.14: Differential conductance of $Ce_2@C_{80}$ and a corresponding IETS spectrum. The dI/dV curve exhibits a characteristic dip around E_F. The width of the feature is correlated with the vibrational excitations resolved in d^2I/dV^2 spectrum. (Tunneling parameters: $V = 150\,\mathrm{mV}$, $I = 0.5\,\mathrm{nA}$, $V_{ac} = 6\,\mathrm{mV}$ (rms).)

modes. The broadening of the features has been defined by the parameter Γ, corresponding to the width of vibrational peak. The thermal broadening described by Eq. (2.17) leads to $\Gamma = 5.4\,k_BT$ [45]. However in the experiments, apart from the thermal broadening, also other effects contribute to the width of the peak, e.g. the broadening due to the modulation voltage, tip-induced broadening and instrumental broadening due to the noise [51]. Therefore, the fitting may result in the values of Γ much higher than it could be expected from the base temperature of the STM ($T = 7\,\mathrm{K}$ gives $\Gamma \approx 3.2\,\mathrm{meV}$). The energies of the excitations $\hbar\omega_1$ and $\hbar\omega_2$ have been predefined by the experiments, by the positions of the peaks ν_1 and ν_2 resolved by STM-IETS spectra (within the experimental error $\pm 2\,\mathrm{meV}$). The energy of the third mode, $\hbar\omega_3$, accounts for the presence of all other vibrational modes active in STM-IETS. A different inelastic constant σ_i, describing the intensity of the modes, has been considered for each vibration.

Before the fitting, the background has been subtracted from the dI/dV data. The background subtraction has been done by fitting the slope of the dI/dV spectrum

resolved on the bare substrate and subtracting the resulting line from the dI/dV curve obtained for $Ce_2@C_{80}$. The procedure has usually led to a symmetric dip around the Fermi level.

Using the Equation (2.17), an excellent fit has been found for all the dips corresponding to different vibrational spectra. Fig. 7.15 shows the fitting results for the characteristic dip features resolved on Cu(111) and Au(111). The evaluated dI/dV spectra correspond to the IETS curves presented in Figs. 7.11(a) and 7.12. The fit reproduces very well the experimental data, including the fine structure of the dip. The energies of the vibrational modes ν_1 and ν_2 are denoted in the graph, given by the experimental d^2I/dV^2 curves. For the energy of the third vibration $\hbar\omega_3$, which accounts for the presence of other modes, best fit value $\hbar\omega_3 = 37(\pm 4)$ has been obtained. Consistent best fit values of the broadening parameter Γ have been obtained for particular modes, regardless of the molecule-substrate system. $\Gamma_1(\nu_1) = 18(\pm 2)\, meV$ has been obtained for the ν_1 mode and $\Gamma_2(\nu_2) = 15(\pm 2)$ for the ν_2 mode. These values are in a good agreement with the full-widths at half maximum (FWHM) of the peaks ν_1 and ν_2 observed in experiment. The fitted broadening of the middle mode is a bit larger, $\Gamma_3 = 25(\pm 5)\, meV$, which is due to the excitation of the modes which have not been explicitly included in the fitting equation. For the inelastic conductance constants σ_i unusually high values have been obtained, compared to the elastic conductance σ_e. The numbers are consistent with the estimation of $\Delta\sigma/\sigma$ for the particular peaks given above.

The presented fitting of the data can accurately reproduce the characteristic shape of the dip. Its structure can be then explained as the superposition of the steps in differential conductance induced by the excitation of several vibrational modes. However, the model explains only the shape of the spectrum and treats the values of σ_i as parameters. As discussed in Section 2.4, the intensity of the peak and the cross section for the specific vibration is determined by the electron-molecule interaction, in particular the electron-phonon coupling. The extremely high values of $\Delta\sigma/\sigma$ observed in the experiment suggest that the excitation of the vibrations strongly perturbs the electronic structure of $Ce_2@C_{80}$ near the Fermi level via the electron-phonon coupling, which in result leads to large changes in conductance. The reason for the surprisingly strong electron-phonon coupling can be determined only by considering a complex theoretical model of the inelastic tunneling through the molecule. However, it is still worth to speculate about the possible effects that can give rise to such behavior.

It is remarkable that the interesting processes that lead to the appearance of the dip for $Ce_2@C_{80}$ are absent in case of the other two fullerenes studied in this work, C_{60} and $Ce@C_{82}$. For comparison, the differential conductance of $Ce@C_{82}$ is given in Fig. 7.16, together with the corresponding vibrational spectrum of this molecule. The dI/dV curve is rather featureless and the vibrational excitations are superimposed on the background. The estimated value of $\Delta\sigma/\sigma$ for $Ce@C_{82}$ is of the order of 5-15%. This comparison suggests that there is something specific about the encapsulation of the two cerium atoms that distinguishes the dimetallofullerene from other fullerenes. Indeed, when one looks into the theoretical calculations of the geometric structure of

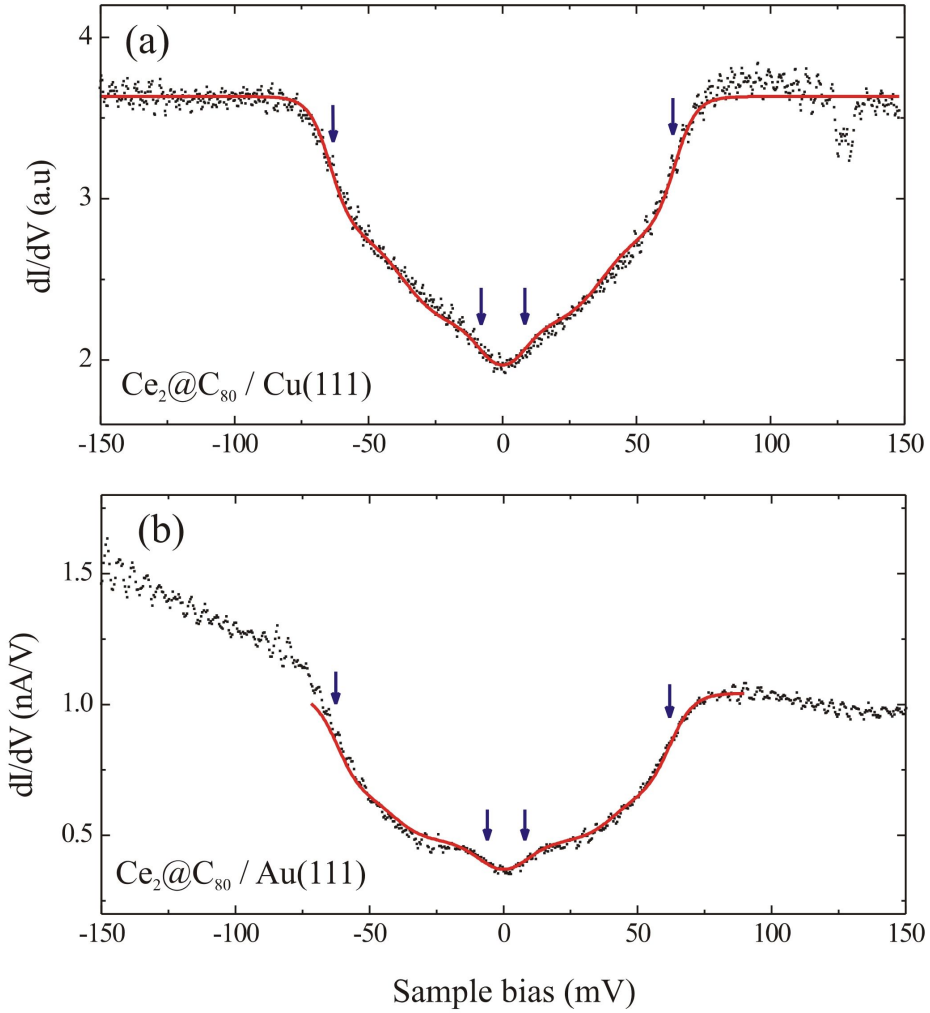

Figure 7.15: Fitting of the dI/dV spectra by the IETS equation (2.17). Black points are the experimental data, red lines correspond to the fit. The fitting has been done for the data with subtracted background. (a) dI/dV curve obtained for $Ce_2@C_{80}$ on Cu(111). The corresponding IETS spectrum is presented in 7.11(a). The best fit results in the broadening of the features $\Gamma_1(\nu_1) = 19\,\text{mV}$, $\Gamma_2(\nu_2) = 16\,\text{mV}$ and $\Gamma_3 = 27\,\text{mV}$. (b) dI/dV curve obtained for $Ce_2@C_{80}$ on Au(111), corresponding to the IETS spectrum in 7.12. The obtained best fit value for the parameter Γ are $\Gamma_1(\nu_1) = 18\,\text{meV}$, $\Gamma_2(\nu_2) = 16\,\text{meV}$ and $\Gamma_3 = 20\,\text{meV}$.

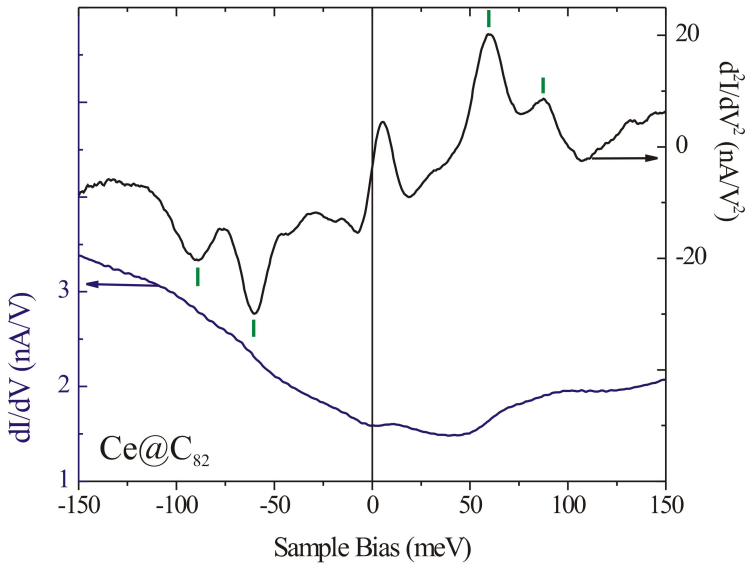

Figure 7.16: Differential conductance of $Ce@C_{82}$ and the corresponding IETS spectrum. The characteristic dip present in the dI/dV spectrum of $Ce_2@C_{80}$ does not appear in case of $Ce@C_{82}$. In contrast, the small steps in conductance are superimposed on the featureless background. (Tunneling parameters: V =250 mV, I =0.5 nA, V_{ac} =6 mV (rms))

both molecules (see Section 7.1 for $Ce_2@C_{80}$ and Section 6.1 for $Ce@C_{82}$), it becomes clear that there is a significant difference in the cerium-cage bonding properties for the two fullerenes. In case of $Ce@C_{82}$ the metal atom occupies one preferential position inside the cage and this configuration is ~ 0.5 eV lower in energy than any other geometric structure. The bonding between cerium and the cage in $Ce_2@C_{80}$ is weaker and the potential barrier between two equivalent chemisorption sites is relatively low. This allows for a free motion of the metal atoms at room temperature, which for $La_2@C_{80}$ has been confirmed by the x-ray diffraction experiments (see Fig. 3.6 in Section 3.4). The calculations for $Ce_2@C_{80}$ yield a potential barrier of the order of 50 meV. The low activation energy has been estimated also from the intramolecular dynamics measurements, where freezing of intramolecular motion has been observed at the temperatures well below 40 K [169]. It is striking that the predicted values of potential barrier are in the same range as the energies of the vibrational modes of the $Ce_2@C_{80}$ molecule. As already discussed, the vibrational mode ν_1 resolved by IETS probably corresponds to the vibrations of cerium and other modes resolved in the spectrum may involve a strong stretching of Ce-C bonds. Taking into account the low diffusion barrier inside the cage, it may be possible to induce the motion of the metal atoms by the inelastic tunneling and excitation of the vibrational mode. The vibration induced hopping of the molecules has been already observed in STM [11, 16, 18]. T. Komeda *et al.* have shown that the translational motion of CO molecule can be initiated by the vibra-

tional excitation and the underlying mechanism involves the anharmonic coupling to the hindered-translational mode related to the lateral hopping. Analogous process can take place in case of the Ce atoms inside the cage, if energy stored in the vibrational mode is transferred to overcome the diffusion barrier. It can be expected that such effect would have a huge influence on the tunneling current and may dramatically change the conductance. Unfortunately, even though such hypothesis seems plausible in case of $Ce_2@C_{80}$, it cannot be verified by STM experiments.

The main conclusion of the above discussion is that the dramatic changes in the differential conductance observed for $Ce_2@C_{80}$ are most likely related to the excitation of molecular vibrational modes. However, the unusual strength of the electron-phonon coupling in case of $Ce_2@C_{80}$ cannot be easily explained. The fact that the vibrational excitation may lead to the occurrence of the dip in the differential conductance curve has been also recently proposed by M. Ternes [50] and W. A. Hofer *et al.* [170] to explain the dI/dV spectrum of an individual Ce atom on Ag(100).

Finally, it should be emphasized, that also other effects can lead to the appearance of the dip-like feature around the Fermi level in STM tunneling spectra, e.g. Kondo effect. Therefore, it cannot be excluded that apart from vibrational excitation, also another mechanism contributes to the observed behavior. The possible scenario that may lead to the formation of the dip is discussed in the following.

7.5.2 Molecular Kondo effect

The Kondo effect arises due to the interaction of magnetic impurity with the conduction electrons of the metal substrate [171, 172]. It can be observed only if the total spin of the electrons of the impurity is nonzero. The typical system for which a Kondo effect can occur at surfaces is a transition or rare earth metal atom on a nonmagnetic substrate [173, 174, 175]. The magnetic moment of these metals is due to the presences of the localized $3d$ or $4f$ states. Single cerium atoms have a highly localized $4f$ electron, and therefore exhibit a nonvanishing magnetic moment and a localized single spin. I has been already shown that also molecules composed from magnetic ions can have a nonzero magnetic moment and give rise to the Kondo scattering [176, 177, 178, 179]. In case of $Ce_2@C_{80}$ two magnetic Ce^{3+} ions are encapsulated in the C_{80} cage. The interaction of their f electrons with the environment may in principle lead to the Kondo effect.

Principles of Kondo effect

When a magnetic atom is adsorbed on a metal surface its spin is screened by the spins of the conduction electrons, as illustrated in Fig. 7.17(a). Below the characteristic Kondo temperature, T_K, the ground state of the system is a singlet state (total spin equal to zero) and the local moment of the adsorbate is completely quenched by the polarization of the metal spins. However, on a short timescale, given by the energy-time Heisenberg uncertainty, the exchange processes may take place that effectively flips the

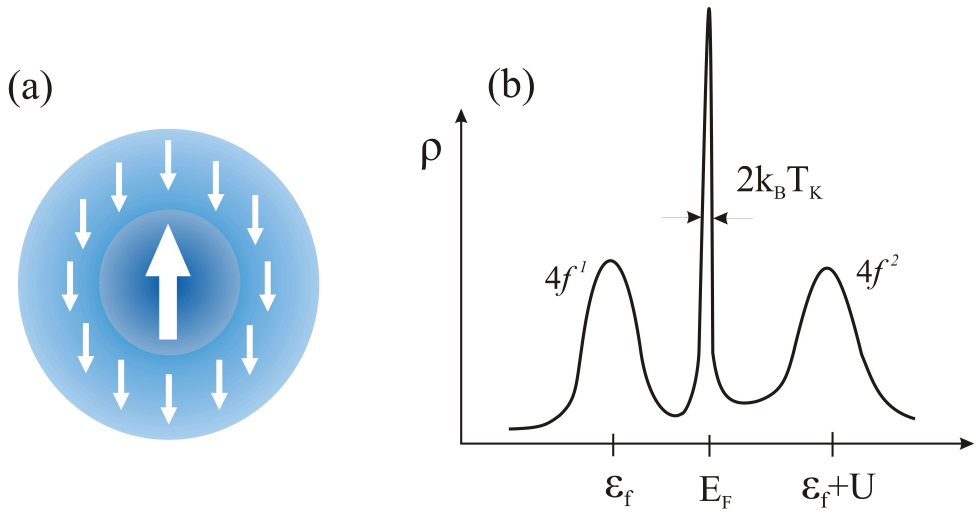

Figure 7.17: The principles of Kondo effect: (a) The magnetic moment of the impurity is screened by the spins of the host conduction electrons. (b) The $4f^1$ state of the atom is broadened by hybridization and is separated from the $4f^2$ states by Coulomb energy U. Due to the spin-flip processes a sharp resonance in the density of states forms at the Fermi energy. The width of the Kondo resonance is related to the Kondo temperature: $\Gamma = 2k_BT_K$.

spin of the adsorbate from 'up' state to 'down' state, and vice versa. Simultaneously, a spin excitation near the Fermi level is created. This spin exchange process changes the energy spectrum of the system and leads to the formation of the new state close to the Fermi level, as shown in Fig. 7.17(b). The state, called Kondo resonance, is a result of many-body interactions. The width of this resonance, Γ, is determined by the Kondo temperature: $\Gamma = 2k_BT_K$. The theoretical model used most-widely to explaining the Kondo effect has been proposed by P. W. Anderson, who considered a single magnetic impurity embedded in a nonmagnetic metallic host [180].

The Kondo resonance can be detected by STS measurements. STM has been used to study the properties of the magnetic impurities on the nonmagnetic metals, like Cu or Au, and has revealed the Kondo feature in the tunneling spectra of single atoms [58, 173, 174, 175]. However, the feature resolved by STS appears usually as a dip not a peak. The characteristic shape of the Kondo resonance in STS originates from the quantum interference between two tunneling channels: one directly into the empty states of the metal and another indirectly, via the spin-flip process [181]. The line-shape of the feature has been identified to be a Fano line shape, defined by the following equation [182]:

$$\frac{dI}{dV} \propto \frac{(q+\varepsilon)^2}{1+\varepsilon} \tag{7.1}$$

In the formula ε stands for $\varepsilon = (eV - E_K)/(\Gamma/2)$, where E_K is the position of the resonance of the width Γ. The Kondo temperature can be identified from the width of

the resonance $\Gamma = 2k_BT_K$. The parameter q characterizes the shape of the resonance which can range from the dip ($q \approx 0$) to a Lorentian peak ($q \to \infty$).

Kondo effect in $Ce_2@C_{80}$?

As mentioned before, the Kondo effect has been already detected in STM for the molecules containing a cobalt ion [176, 178, 179]. In general, the Kondo phenomenon is very sensitive to the local environment of the magnetic atom. In case of molecules, the interaction of the magnetic ion with the ligands may completely quench the magnetic moment, as has been shown for CoPc molecule [176]. The Kondo temperature observed for molecules is usually higher then that for the single atom due to the change in the chemical environment of the ion and partial hybridization of the d state. Iancu *et al.* have shown, for the example of the TBrPP-Co molecules, that the Kondo temperature can be also modified by switching of the conformation of the molecule [178] or manipulating the number of the nearest-neighbors [179]. Their study also indicates that the Kondo effect may be generated by a spin-electron coupling through the molecular bonding.

All the Kondo systems studied so far by STM exhibit spin $S = \frac{1}{2}$. In case of $Ce_2@C_{80}$ there are two magnetic ions, each of the exhibiting a single spin originating from $4f$ electron. The DFT calculations predict that the ground state of the molecule is a triplet. It would mean that $Ce_2@C_{80}$ has a nonzero spin in the ground state $S = 1$, originating from the two parallel spins of the localized f electrons. In principle then, the Kondo effect in such system may be possible. However, the analysis of the Kondo scattering for the system with spin $S = 1$ is much more complicated than in case of spin $\frac{1}{2}$.

As discussed above, the Kondo mechanism leaves as a fingerprint a Fano-shaped feature at E_F in the STS spectra. To investigate the hypothesis of Kondo effect in $Ce_2@C_{80}$ the dip resolved for the molecule at the Fermi level has been fitted with the Fano equation 7.1. The results are presented in Fig. 7.18, for the dip discussed previously in Fig. 7.14(a). Fano parameters obtained from the fit are: $q \approx 0$, $E_K = 5.6\,\text{meV}$ and $k_BT_K = 72\,\text{meV}$. The Kondo temperature determined from the fitting of different data sets is of the order of $600 - 800\,\text{K}$. The obtained value is very large, but seems possible taking into account the high Kondo temperature of the γ-phase of bulk Ce $T_K > 1000\,\text{K}$ [183]. For a single Ce atoms on Ag(111) also a relatively high temperature has been observed, $T_K \approx 150\,\text{K}$ [175].

However, the overall agreement between the fit and experiment is worse than in case the IETS equations (Fig. 7.15). The Fano equation does not describe very well the shape of the dip and does not account for the slope changes within the dip. The Kondo resonance also cannot explain the fact why the width of the dip is always correlated with the vibrational spectrum, regardless of the number and energy of resolved modes. The dips also usually appear rather symmetric after the background subtraction, whereas the the Fano feature resolved by STS is normally slightly asymmetric. Futhermore, it remains unclear why Kondo effect would occur for $Ce_2@C_{80}$ and not for $Ce@C_{82}$, which also exhibits a nonzero spin $S = \frac{1}{2}$. All this seems to point out the Kondo

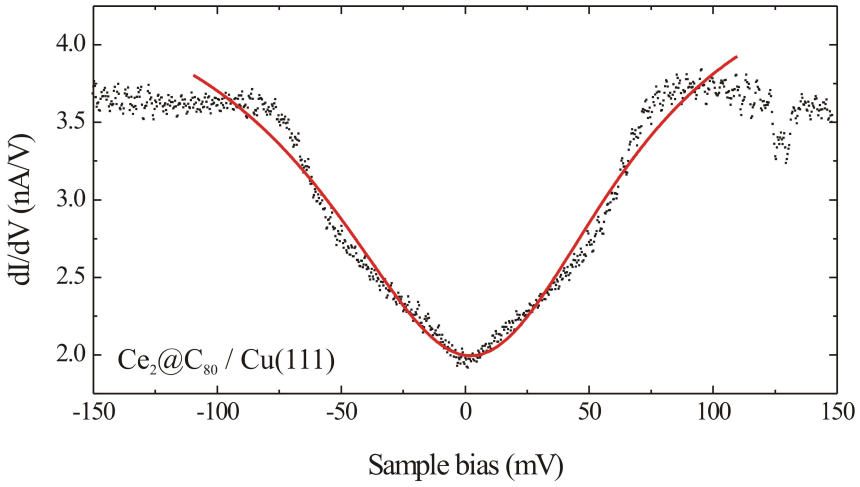

Figure 7.18: Fano fit for the characteristic dip resolved in dI/dV spectrum of $Ce_2@C_{80}$ on Cu(111). The parameters of the fit are: $q \approx 0$, $E_K = 5.6\,\text{meV}$ and $k_B T_k = 72\,\text{meV}$.

scattering is not the most probable explanation for the appearance of the dip. However, at the moment its contribution cannot be completely excluded. The presence of the Kondo effect could be verified by comparing the results for $Ce_2@C_{80}$ with the study of $La_2@C_{80}$, for which the two encapsulated ions are not magnetic. Unfortunately, such measurements are not available at the moment. Additionally, the investigations of the temperature or magnetic field dependence of the spectrum could also help to establish the origin of the feature.

Finally, also other effects may lead to the formation of the dip at the Fermi energy. Other processes occurring for strongly correlated electron system may account for anomalies at zero-bias [184]. Jahn-Teller distortion has been determined to be a driving mechanism of the gap opening in K_4C_{60} layers [185]. In case of the systems weakly coupled to the electrodes, a current suppression at low bias voltages can be expected, due to the Franck-Condon blockade [186]. However, none of theses effects seems to be probable in case of $Ce_2@C_{80}$, and therefore they will be not discussed in detail in this thesis.

7.6 Conclusions

Depending on the deposition conditions, two different structures of $Ce_2@C_{80}$ molecules have been grown on Cu(111): islands, as in case of $Ce@C_{82}$, and chains, in which molecules are arranged in double rows along the steps. The tunneling spectroscopy study of these structures has revealed several important features of $Ce_2@C_{80}$ molecules. STS measurements and energy-resolved mapping of the electronic states show that

the molecules within one chain exhibit two types of dI/dV spectra with corresponding different sets of spectroscopic maps. The observed modifications in the electronic structure are most probably due to existence of two different preferential adsorption configurations of the molecules.

Interesting results have been obtained by the inelastic spectroscopy measurements (STM-IETS). The total number of resolved modes is relatively high, compared to measurements presented in this thesis for C_{60} and $Ce@C_{82}$. Surprisingly, the vibrational spectra reveal also the presence of a low energy mode (ν_1), not excited in case of other fullerenes. It seems very likely that the mode is related to the movement of two cerium atoms and corresponds to one of the vibrations of the Ce-Ce unit, predicted in this energy range by DFT calculations.

The investigation of the STS spectra of $Ce_2@C_{80}$ at low bias voltages reveals rather unexpected results. Unusual changes in the differential conductance of the molecule are observed near the Fermi energy. The comparison of the dI/dV curves and the vibrational spectra suggests that the increase in conductance is related to the excitations of vibrational modes. However, the origin of this exceptionally strong electron-phonon coupling in case of $Ce_2@C_{80}$ remains unclear. It cannot be excluded that also other effects may contribute to the observed behavior. In particular, it has been pointed out that there exists a possibility of Kondo effect, arising due to the presence of two magnetic cerium ions. To undoubtedly establish the reason of the observed behavior, futher measurements and theoretical calculations are required.

Chapter 8

Contact to a single fullerene molecule

Miniaturization of the electronic devices down to the atomic and molecular size requires understanding of the properties of nanoscale contacts. Over the last years research has been focused on the nature of the electron transport through various nanostructures, among them metallic point contacts [187, 188], carbon nanotubes [189], DNA [190, 191] and molecular junctions [192, 193, 194, 195, 196].

The two most popular techniques applied to fabricate and study the nano-contacts are mechanically controllable break junctions (MCB) and STM. Both methods allow the adjustment of the contact size between the electrodes by using the piezoelectric actuators. In break junction experiments the distance between two microscopic pieces of metal can be tuned with sub-atomic precision, however the area of the contact and the structure of the electrodes remains unknown. In contrast, STM allows to partially define the junction geometry. Structure of the investigated system can be imaged prior to and after contact formation. Therefore the identity, location, and number of atoms/molecules in between the electrodes can be well controlled. In case of single molecules several parameters influencing the conductance can be determined, e.g. orientation of the molecule with respect to the substrate or its bonding site. Additionally, the structure of the second electrode, STM tip, can be to some extent characterized by analysis of the data measured on the clean surface.

This chapter presents a study of the contact formation between a single molecule and the STM tip. First sections briefly introduce the principles of the ballistic transport and shortly report on the main findings in the field of the atomic and molecular scale STM contacts. Subsequently, the conductance measurements through single fullerene molecules are described. A controlled contact has been formed for two different fullerene molecules, C_{60} and $Ce_2@C_{80}$, adsorbed on Cu(111). The results reflect the differences in the electron transport properties hollow and doped fullerenes.

8.1 Principles of ballistic transport

The transport through a macroscopic object is described by the Ohm's law. The conductance, $G = I/V$, is proportional to the area of the conductor, A, and inversely proportional to the conductor length, L, i.e. $G = \sigma A/L$. The conductivity σ is the property of the material, independent of the dimensions. However, this simple relation holds only if the dimensions of the conductor are much larger than the characteristic scattering length of the system. When the size of the object gets smaller, below the mean free path of the electrons, ballistic transport takes place, i.e. the electrons travel without scattering on defects or impurities. In the ballistic transport regime Ohm's law is no longer valid and the conductance becomes quantized.

A theoretical explanation of the ballistic transport was proposed by Landauer [197]. In the model one dimensional (1D) conductor is placed between the ideal electron reservoirs held at the potential difference V. Such a system exhibits a distinct number of conduction modes N_c, each of them having a characteristic transmission probability T. The conductance can be then expressed by the formula

$$G = \frac{2e^2}{h} \sum_{n=1}^{N_c} T_n, \tag{8.1}$$

where T_n denotes the transmission probability of the n-th channel, e is the electron charge and h the Planck constant. In the ideal case the transmission of each channel is equal to 1, $T_n = 1$, and the Equation (8.1) simplifies to

$$G = N_c \frac{2e^2}{h}, \tag{8.2}$$

with $G_0 = \frac{2e^2}{h}$ being the conductance quantum.

An important feature of this expression is that the conductance is finite, i.e. the resistance in nonzero. Voltage drop associated with this finite resistance is localized on the contact, which means that even though electrons travel trough the conductor without scattering, a contact resistance is always present in ballistic systems.

As already mentioned, the quantized conductance can be observed for a system of the size smaller than the electron mean free path. For metals the Fermi wavelength is in the range of the atomic distances and the conductance quantization occurs only for the atomic-size contacts. Essentially, the conductance of the metal point-contact depends on the character of the valence orbitals of the atoms forming the electrodes [198]. In case of the molecular junctions, the main factor determining the transport properties is the electronic structure of the molecule [1]. The number and transmission probabilities of the conduction channels are defined by the molecular resonances and the chemistry of the electrode-molecule contact.

8.2 Nanoscale contacts in STM

The properties of the nanoscale contacts have been frequently investigated by STM [199, 200, 201, 202]. The first studies have been focused on the conductance of the metallic point contacts, formed by the controlled indentation of the tip into the substrate material [199, 200, 201]. Upon retracting the tip, the contact is gradually broken and the conductance of the junction exhibits characteristic plateaus as the function of the tip-sample displacement. For most of the metals the last plateau before loosing contact is nearly flat and very close to $1\,G_0$, indicating that the conductance of the single-metal-atom point contact is close to the conductance quantum. The jumps in the conductance are attributed to a sudden rearrangement of the atomic structure of the contact. The results obtained in this way by STM are similar to the measurements by the break junction technique.

STM is also an ideal tool to study the contact formation. For the clean surfaces, the tunneling-to-contact transition is often accompanied by an abrupt increase in conductance [202, 203]. Jump-to-contact can be understood in terms of relaxation of the geometry of the system, due to the adhesive forces acting between the tip and the metal surface [203]. This process often leads to an irreversible atomic rearrangement of the tip. Lately, Limot *et al.* [202] have reported a reproducible contact formation between STM tip and silver and copper adatoms on Ag(111) and Cu(111) surfaces. In contrast to the bare (111) metallic surface, for which a discontinuous sharp jump in conductance has been observed, a smooth and reproducible transition has occurred in case of single adatoms, with contact conductance close to G_0. The calculations have indicated presence or absence of jump-to-contact is related to the elastic properties of material or adsorbate [202, 203].

Surprisingly however, not much attention has been paid to the tip-molecule contact in STM. One of the first studies was devoted to the contact with the individual C_{60} molecule [194]. Recently, Neel *at al.* [195] have revisited the formation of the C_{60} junction and investigated in detail the conductance behavior. The contact point is characterized by a sudden increase in conductance, however the transition region is smooth, as in case of single adatoms [202, 204].

Apart from STM, also other techniques provide valuable information about the conductance of individual molecules, for instance mechanically controllable break junction techniques [192, 193] or electrochemical approach [196]. In particular, MCB methods have been used to fabricate C_{60} molecular junctions and study the conduction mechanism in a single molecule transistor (SMT) [168, 205].

8.3 Conductance of single fullerene molecules

The main goal of the experiments presented in this section has been to investigate the conductance of a single endohedral fullerene upon contact with the STM tip. Compared to the hollow cages, e.g. C_{60}, dimetallofullerenes have additional degrees of freedom associated with the two encapsulated atoms, that can influence the electron transport

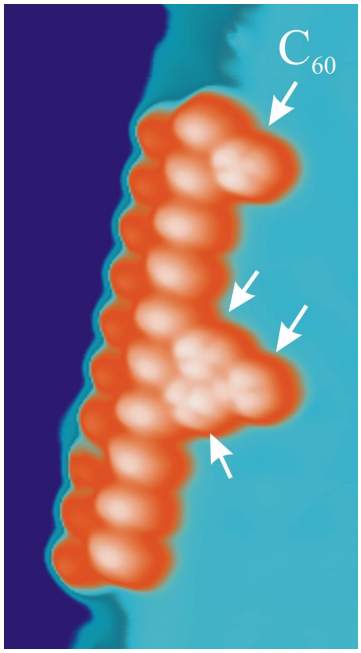

Figure 8.1: STM image of $Ce_2@C_{80}$ and C_{60} molecules co-deposited on Cu(111). C_{60} (indicated by arrows) can be distinguished from endohedral fullerenes due to the characteristic internal structure. ($12 \times 7\,\mathrm{nm}^2$, $V = 0.1\,\mathrm{V}$, $I = 1\,\mathrm{nA}$)

trough the molecule. Therefore, one can raise an interesting question, if the contact to the STM tip induces any changes in geometry of the encaged atoms and if those changes are reflected in the conductance curves.

8.3.1 Experimental procedure

An ideal way to study the influence of the metal atoms on the molecular conductance would be to correlate the results obtained for $Ce_2@C_{80}$ with the ones for an undoped C_{80} cage. However, the empty C_{80} has low stability and is hardly available. Therefore, the C_{60} molecule has been chosen as a reference. The sample has been prepared by the co-deposition of C_{60} and $Ce_2@C_{80}$ on the Cu(111) substrate. Firstly, the $Ce_2@C_{80}$ molecules have been deposited, as described in Section 4.2. Subsequently, the sample has been cooled to T=77 K and C_{60} molecules have been sublimed. Figure 8.1 shows STM image of the Cu(111) surface covered with $Ce_2@C_{80}$ and C_{60} molecules. C_{60} can be easily distinguished from the endohedral complexes due to the specific internal structure resolved by STM. $Ce_2@C_{80}$ molecules appear in the image as smooth and featureless protrusions, whereas C_{60} is characterized by a clear three-lobed pattern. The three-fold symmetry allows also to establish that C_{60} molecules are adsorbed with a hexagonal face pointing up (see Section 5.3).

Following procedure has been used to contact the molecules:

- The tip has been positioned over the middle of the fullerene molecule. The feedback has been disabled. The starting position of the tip ($\Delta z = 0$) is then defined by the set current and voltage before opening the feedback loop.
- The tip has been moved towards the molecule ($\Delta z < 0$) by 6-8 Å. The sample bias has been kept constant and the current has been simultaneously measured,

giving a characteristic conductance trace versus tip-sample distance.

- The tip has been retracted from the sample. During retraction the current has been recorded, as well.

The usual time range of the whole procedure has been approximately 10-15 s, corresponding to the tip displacement speed of 1-2 Å/s. All the experiments have been performed at low temperature ($T = 7\,\mathrm{K}$) what ensured the necessary stability of the molecular junction. Tungsten tips have been prepared by controlled indentation into the Cu surface. Prior and after the contact formation the tip status has been monitored by recording a dI/dV spectrum on Cu(111). Only tips giving a featureless spectrum with clearly resolved onset of the surface state have been used in the futher measurements.

An important issue to mention is the wide range of the current measured during the experiment. The current values in one cycle vary from $\sim$3 nA up to $\sim$30 μA, corresponding to the tunneling resistance R changing from $\sim$100 MΩ to $\sim$10 kΩ. Such a big range of resistance could cause the voltage drop at the input impedance R_{in} of the current preamplifier [201]. As a consequence, the bias voltage of the tunneling junction would be decreased by $(1+R_{in}/R)^{-1}$, which would lead to a incorrect conductance measurements. As discussed in Ref. [206], the problem can be solved by using the variable gain current preamplifier. The curves presented in this Chapter have been measured with the preamplifier gain 10^5, for which the input impedance is equal to 50 Ω. Since the input impedance is still significantly lower than the tunneling resistance ($R_{in}/R = 0.5\%$ in maximum), no considerable voltage drop is present in the discussed measurements.

8.3.2 Transport measurements through C_{60} and $Ce_2@C_{80}$

Typical conductance curves obtained for C_{60} and $Ce_2@C_{80}$ fullerenes are shown in Fig. 8.2. The conductance $G = I/V$ is presented in a logarithmic scale versus the relative distance between tip and molecule. The *zero* position of the tip is defined by the feedback parameters: $I_0 = 3\,\mathrm{nA}$ and $V_0 = 300\,\mathrm{mV}$, afterwards tip is moved by $6 - 6.5$ Å towards the molecule. The contact process has been completely reversible, i.e. neither tip nor the molecule has changed during the measurements, what has been confirmed by STM images and dI/dV spectra.

Two general conclusions follow from the analysis of Fig. 8.2(a). First of all, there is no striking difference between the conductance traces obtained for C_{60} and $Ce_2@C_{80}$. Both curves have qualitatively similar shape and reveal two sudden changes in conductance at roughly the same tip-molecule displacements. Secondly, the measurements for both molecules resemble the results obtained for C_{60} by Neel *at al.* in Ref. [195], suggesting that the curves reflect the general trend in conductance upon contacting the fullerene molecule.

The conductance traces are analyzed in detail in the following.

- First region, between $\Delta z = 0$ and $\Delta z \approx -2$ Å, is characteristic for the tunneling regime. The conductance increases exponentially as the tip moves towards the sample, which reflects the exponential dependence of current over distance.

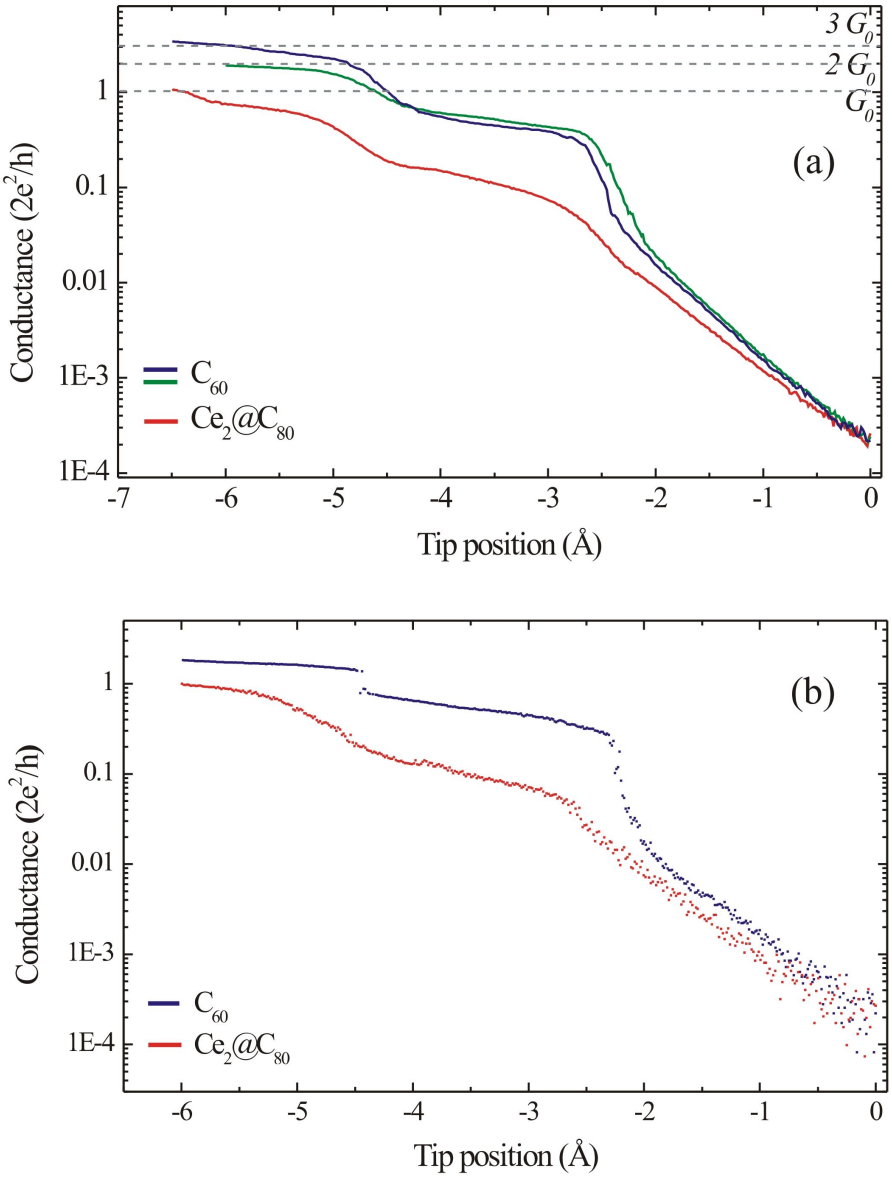

Figure 8.2: (a) Conductance curves obtained for C_{60} (blue and green) and $Ce_2@C_{80}$ molecules (red), as a function of tip-molecule distance. Each curve is an average of approximately 50 single measurements. The contact is formed for both molecules at tip displacement ≈2.5 Å. The *zero* position of the tip is defined by feedback parameters $U = 300\,\mathrm{mV}$, $I = 3\mathrm{nA}$. (b) Examples of the single measurements of the conductance vs distance curves for C_{60} (blue) and $Ce_2@C_{80}$ (red). At the tip displacement of ≈4.5 Å, C_{60} exhibits a discontinuous jump in conductance, whereas for $Ce_2@C_{80}$ transition is smooth.

The exponential behavior, $G \propto exp(-2\kappa\Delta z)$, is determined by the inverse decay length, κ, which is related to the apparent barrier height, Φ, by $\kappa = \sqrt{2m\Phi/\hbar^2}$ (see Section 2.1). The values of the apparent barrier height extracted from the measurements are following: $\Phi = 4.1(\pm 0.8)\,\mathrm{eV}$ for Cu(111), $\Phi = 5.1(\pm 1)\,\mathrm{eV}$ for C_{60}/Cu(111) and $\Phi = 4.4(\pm 1.1)\,\mathrm{eV}$ for $Ce_2@C_{80}$/Cu(111). The higher value for C_{60} compared to the of $Ce_2@C_{80}$, is in agreement with the fact that the ionization potential of C_{60} is higher than that of endohedral fullerenes [98].

- Around $\Delta z = -2.5\,\text{Å}$ a sudden increase of conductance is observed for both molecules. In agreement with Ref. [195], this jump is assigned to the transition from the tunneling into contact. The formation of the contact is accompanied by the creation of the chemical bond between the tip and the fullerene. After establishing the contact, the conductance of both fullerene molecules is lower than G_0. For the C_{60} the typical value is $\approx 0.4\,G_0$, whereas $Ce_2@C_{80}$ exhibits smaller conductance, around $\approx 0.08\,G_0$. The reason for this difference will be discussed later in this section.

- Futher movement of the tip towards the molecule causes a rise of conductance, however, with smaller slope than in the tunneling regime. Around $\Delta z = -4.5\,\text{Å}$ a second jump in conductance is observed. Detailed analysis of the curves reveal, that the jump has different character for C_{60} and $Ce_2@C_{80}$, which is illustrated in Fig. 8.2(b).

- Finally, for tip displacements $\Delta z < -4.5\,\text{Å}$, the conductance increases slowly and reaches the values close to multiples of G_0. Usually values $\approx 2\,G_0$ or $3\,G_0$ have been observed for C_{60}. The conductance of $Ce_2@C_{80}$ rises up to $1\,G_0$ but is still lower than of C_{60}. The high conductance values $G \geq G_0$ are in good agreement with the theoretical calculations [207, 208].

The characteristic feature of the traces is that the transition from tunneling to contact is rather smooth and, contrary to the bare substrate [204], no discontinuous jump is observed. Neel *at al.* [195] associate this broadening of the transition region with the rise of the temperature of the junction. Fig. 8.3 shows the influence of the bias voltage on the width of the transition region. For low voltages a steep jump is observed, whereas a significant broadening is present for higher voltages. This finding is consistent with the proposed thermal nature of the broadening, since smaller energy dissipation in the junction is expected for lower bias voltages.

The fact that the two jumps in conductance observed for endohedral fullerene occur as well in the curves for the undoped molecule suggests that none of the changes can be unambiguously assigned to the switching of the geometry of the encaged metal atoms. However, despite similar trends, the traces of C_{60} and $Ce_2@C_{80}$ exhibit some differences, as discussed in the following.

The first evident difference between the results for empty and doped fullerene is the range of conductance of the two molecules after the contact formation. The tunneling-to-contact transition occurs for both fullerenes at roughly the same tip displacement,

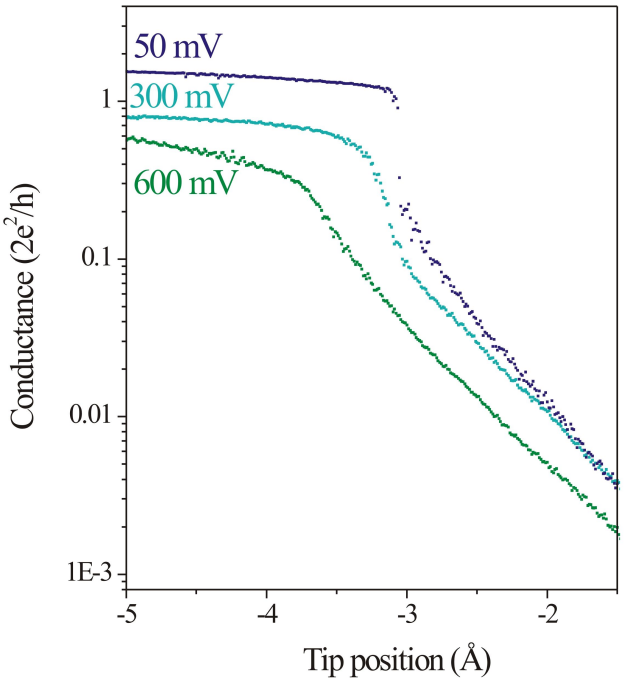

Figure 8.3: Bias dependence of the width of the tunneling-to-contact transition region. The curves have been recorded for the C_{60} molecule, at bias voltages 50 mV, 300 mV and 600 mV. The starting current point was set to 0.5 nA, 3 nA and 6 nA, respectively.

however, $Ce_2@C_{80}$ exhibits around 5 times lower conductance than C_{60}. The explanation is not simply related to the different sizes of the carbon cages. The diameter of C_{80} is ∼1Å bigger than that of C_{60}, however an easy approximation of a fullerene as a sphere of a defined conductivity gives the conductance independent of the diameter. This suggests that difference in the transport properties is rather related to the electronic structure of the molecules than a size effect.

In the contact regime the transport through the molecule strongly depends on the electronic structure of molecule and the coupling between the molecule and the electrodes. The voltage applied in the discussed experiments correspond to region in the STS spectra which is for both molecules dominated by the LUMO resonance. Therefore, most probably the conduction occurs primarily through the lowest unoccupied orbital. The LUMO of isolated C_{60} is threefold degenerate, which may account for the higher number of available transmission channels. However, simulations predict that only one of the three states contribute strongly to the transport and the transmission coefficients of other two are very low [208]. More likely explanation of the difference in the conductance is that the presence of metal ion influences the conduction channels. According to Refs. [208, 209], transport through fullerene molecules occurs mainly along the C-C bonds and not directly through the middle of the cage. The lowest unoccupied orbitals of $Ce_2@C_{80}$ are dominated by cerium states and it can be expected that the partial localization of the orbital on metal atoms disturbs the conduction mechanism. This effect has been confirmed by the theoretical study of Senapati *et al.* [209], who found that doping of C_{82} with Gd atom reduces some of the conducting channels and in consequence decreases the conductivity of the $Gd@C_{82}$ species relative to the empty C_{82} molecule.

Lower conductivity of the endohedral complexes, compared to that of C_{60}, was also observed in the molecular field effect transistors. The low mobility of carriers measured for $La_2@C_{80}$ thin film has been related to the smaller overlap of molecular LUMOs due to the localization of electron density on metal ions [33].

Interestingly, theory predicts that endohedral doping may increase the conductance of the fullerene dimers [208]. However, the reason for it is not related to the conductance of individual molecules, but to the scattering effects on the junction between the fullerenes.

The last characteristic feature in the curves is the second increase in conductance which for both molecules takes place at the tip position $\Delta z \approx -4.5\,\text{Å}$. From the single traces presented in Fig. 8.2(b) it becomes clear that for C_{60} this rise is actually a discontinuous jump, while in case of $Ce_2@C_{80}$ the transition is smooth. The origin of this conductance change is not exactly clear. As proposed in Ref. [195], it is most probably due to a rearrangement of the junction geometry, which leads to the higher number of available conductance channels. The measurements discussed in this Chapter suggest that the atomic rearrangement of the tip is not a very probable explanation. The experimental conductance traces exhibit usually no hysteresis and the unchanged structure of the tip is confirmed by the STM images and the dI/dV spectra of the clean surface. The fact that for exactly the same tip different behavior is observed for hollow and doped fullerene indicates that the rise in conductance may be related to the molecule itself. The possible explanations are e.g. a reversible modification of molecular geometry or the formation of additional tip-fullerene bonds.

8.4 Conclusions

The presented results illustrate the main differences in the transport properties of the hollow and endohedrally doped fullerenes. The conductance traces measured as the function of the tip displacement show similar trends in case of $Ce_2@C_{80}$ and C_{60}. In both cases the contact formation is indicated by a smooth transition region. The futher indentation of the tip into the molecules leads to the second sudden increase in conductance, of so far not clear origin. Neither of these changes can be directly related to presence of the encapsulated cerium atoms. However, from theoretical studies it is known that the endohedral doping with the metal atoms influences the transport properties of the fullerene and affects the conduction channels [208, 209]. This effect is in our measurement reflected by the lower conductance measured for $Ce_2@C_{80}$ molecules, compared to that of the C_{60}.

The results indicate also that a low temperature STM may provide interesting information regarding the contact formation and the conductance of a single molecule. The control over the geometry of the junction allows to obtain reliable and reproducible data. The great advantage is also the possibility of measuring the data for a number species with the same tip. Such a procedure enables a direct comparison of the transport properties of different molecules.

Chapter 9

Summary

This thesis presents the study of electronic and vibrational properties of three fullerene molecules: C_{60}, $Ce@C_{82}$ and $Ce_2@C_{80}$, adsorbed on metal surfaces. The investigated molecules are representatives of the hollow and doped fullerene families, significantly different in their nature and properties. The electronic structure of C_{60} is defined by the delocalized π orbitals. The molecule adsorbed on a metal substrate forms a well-defined and already extensively investigated system, providing good reference data for the futher study of metallofullerenes. In contrast, the properties of the endohedral complexes are influenced by hybridization of the metal-cage orbitals. The encapsulation of the metal atoms also reduces the symmetry of the system which accounts for much more complex electronic structure of these molecules, compared to C_{60}. The $Ce@C_{82}$ and $Ce_2@C_{80}$ molecules chosen for the study belong to two different classes of endohedral complexes: monometallofullerenes $M@C_{80}$, which exhibit open shell structure and a characteristic singly occupied oribital (SOMO), and dimmetallofullerenes $M_2@C_{82}$ which have a highly symmetric cage geometry and exhibit a large HOMO-LUMO gap. The properties of these molecules have been studied locally by means of elastic and inelastic scanning tunneling spectroscopy. The explanation of the complex results obtained for the metallofullerenes has been possible by considering the structure of the molecules predicted by DFT calculations [1].

STM imaging allows to resolve the characteristic internal structure of the molecules and consequently to distinguish between different molecular orientations. The interpretation of the constant current STM images of C_{60} is relatively easy and the resolved pattern can be directly related to the structure of the highly symmetric molecular orbitals. Such straightforward interpretation of the images of the endohedral fullerenes is not possible because the geometry of these molecule is much more complicated. The STM images of $Ce@C_{82}$ islands resolve different intramolecular patterns, of a complex, bias dependent structure. Based on the DFT calculations performed for a free $Ce@C_{82}$ molecule, a particular orientation of the cage have been assigned to the specific intramolecular pattern. The results obtained for $Ce_2@C_{80}$ show that upon annealing the disordered metallofullerene islands evolve into molecular chains adsorbed along the step

[1] calculations by K. Muthukumar and J. A. Larsson, Tyndall National Institute, Cork, Ireland

edges. The topography images of $Ce_2@C_{80}$ on Cu(111) did not show any intramolecular features, however the energy-resolved spectroscopic imaging show that $Ce_2@C_{80}$ molecules in the chains exhibit two preferential bonding configurations.

The investigation of the electronic properties of the fullerenes reveals that the electronic structure of the molecules is affected by the chemisorption. In particular, the STS study of C_{60} on Cu(111) have shown that additional LUMO-derived peak appears in the spectra, arising due to the charge transfer from the substrate into the LUMO orbital of the fullerene. As indicated by the tunneling spectroscopy measurements of $Ce@C_{82}$ and $Ce_2@C_{80}$, and confirmed by DFT calculations, the electronic structure of the metallofullerenes is much more complex. The molecular orbitals of endohedral fullerenes are no longer delocalized on the carbon cage, as in case of C_{60}, but the hybridization of the metal-cage states leads to a partial localization of the orbitals on the cerium atom/atoms. The fact that the electronic states exhibit a partial Ce-character has an observable effect on the STS spectra of the metallofullerenes. For $Ce@C_{82}$ molecules, a strong dependence of the tunneling spectra on the molecular orientation has been observed. This finding has been explained by the dominating number of the hybrid states in the molecular spectrum, which due to the localization give different contribution to the tunneling current for different bonding configurations. In contrast to $Ce@C_{82}$ islands, the differences observed for dI/dV measurements of $Ce_2@C_{80}$ recorded over the molecular chains on Cu(111) are not so pronounced. The STS reveals the modification of the electronic structure of the lowest lying unoccupied states. The energy-resolved mapping of the electronic states suggests that the differences are due to two different bonding geometries.

Vibrational spectroscopy study of the fullerenes show that out the many intramolecular vibrational modes, only few are active in the inelastic tunneling spectroscopy (STM-IETS). For C_{60} molecule on Cu(111) two vibrational modes have been resolved. The features correspond most probably to the $H_g(\omega_2)$ and $H_g(\omega_5)$ vibrational modes of a free molecule. In case of metallofullerene the exact assignment of the modes has not been possible, due to a large number of vibrational frequencies. However, it has been established that none of the modes involving the movement of the encapsulated atom is active in case of $Ce@C_{82}$. The two modes resolved in the spectrum clearly correspond to the internal phonons of C_{82} cage. The outcome of the inelastic spectroscopy measurement for $Ce_2@C_{80}$ has been much more interesting. Firstly, the number of the modes excited in case of $Ce_2@C_{80}$ is higher than for other two fullerenes - altogether at least five modes of different vibrational frequencies have been resolved. Secondly, a characteristic low energy peak ($\hbar\omega(\nu_1) = 6 - 9\,\mathrm{meV}$) appears in the STM-IETS spectrum. The fact that this feature is absent in the vibrational spectra of C_{60} and $Ce@C_{82}$ allows to relate it to the two encaged cerium atoms. It seems likely that this excitation corresponds to one of the two doubly degenerate modes of the Ce-Ce unit, predicted in this frequency range by DFT calculations. However the hypothesis of molecule-against-substrate vibration has to be also taken into account.

The spectroscopic results obtained for $Ce_2@C_{80}$ reveal that an unexpected effect occurring in case of tunneling through $Ce_2@C_{80}$, which leads to exceptionally large changes in the differential conductance near the Fermi energy and formation of a dip-

like feature in the dI/dV spectrum. The detailed analysis suggest that this process is correlated with the excitations of molecular vibrational modes. The reason for the surprisingly strong electron-phonon coupling is not clear, however, the fact that the feature is not observed in case of C_{60} and $Ce_2@C_{80}$ suggests that it may be related to the presence of two cerium atoms. However, it cannot be excluded that apart from the inelastic excitations also other processes contribute to the observed behavior.

Finally, the transport properties of hollow and doped fullerenes have been investigated. A single-molecule STM junction has been formed by controlled contact formation to C_{60} and $Ce_2@C_{80}$. The measurements of conductance as a function of tip-sample reveal two characteristic transition regions, but neither of them can be related with the encapsulated atoms. The tunneling-to-contact transition is smooth for both molecules and the conductance traces of C_{60} and $Ce_2@C_{80}$ exhibit generally similar trends. The experiments show, however, that the conductance of a $Ce_2@C_{80}$ junction is lower, compared to that of C_{60}. The finding suggests that the presence of metal atoms hinders the conduction process which primary takes place along the carbon cage.

Several questions that have emerged during discussing the results presented in this thesis still remain unanswered. The metallofullerenes adsorbed on metal surfaces exhibit rather complex properties, due to the presence of encapsulated atoms and partially also due to the chemisorption effects. The explanation of all the raised issues would require futher experimental measurements as well as theoretical modelling of the interaction of the fullerenes with the substrate. The spectroscopic measurements performed in this work reveal that unexpected effects occur in case of tunneling through $Ce_2@C_{80}$, which distinguishes this molecule from other two fullerenes, C_{60} and $Ce@C_{82}$. Dimetallofullerenes adsorbed on metal substrates may, therefore, provide an interesting system for a deeper study.

Bibliography

[1] C. Joachim, J. K. Gimzewski and A. Aviram. Electronics using hybrid-molecular and mono-molecular devices. *Nature* **408**, 541 (2000)

[2] J. K. Gimzewski and C. Joachim. Nanoscale Science of Single Molecules Using Local Probes. *Science* **283**, 1683 (1999)

[3] S. A. Wolf, D. D. Awschalom, R. A. Buhrman, J. M. Daughton, S. von Molnar, M. L. Roukes, A. Y. Chtchelkanova and D. M. Treger. Spintronics: A Spin-Based Electronics Vision for the Future. *Science* **294**, 1488 (2001)

[4] A. J. Heinrich, J. A. Gupta, C. P. Lutz and D. M. Eigler. Single-atom spin-flip spectroscopy. *Science* **306**, 466 (2004)

[5] G. Binnig, H. Rohrer, C. Gerber and E. Weibel. Surface studies by scanning tunneling microscopy. *Phys. Rev. Lett.* **49**, 57 (1982)

[6] G. Binnig, H. Rohrer, C. Gerber and E. Weibel. Tunneling through a controllable vacuum gap. *Appl. Phys. Lett.* **40**, 178 (1982)

[7] W. Ho. Single-molecule chemistry. *J. Chem. Phys.* **117**(24), 11033 (2002)

[8] J. K. Gimzewski, E. Stoll and R. R. Schlittler. Scanning tunneling microscopy of individual molecules of copper phthalocyanine adsorbed on polycrystalline silver surfaces. *Surf. Sci.* **181**, 267 (1987)

[9] H. Ohtani, R. J. Wilson, S. Chiang and C. M. Mate. Scanning tunneling microscopy observations of benzene molecules on the Rh(111)-(3×3)(C_6H_6+2CO) surface. *Phys. Rev. Lett.* **60**, 2398 (1988)

[10] B. C. Stipe, M. A. Rezaei and W. Ho. Single-Molecule Vibrational Spectroscopy and Microscopy. *Science* **280**, 1732 (1998)

[11] T. Komeda. Chemical identification and manipulation of molecules by vibrational excitation via inelastic tunneling process with scanning tunneling microscopy. *Prog. Surf. Sci.* **78**, 41 (2005)

[12] J. Gaudioso, L. J. Lauhon and W. Ho. Vibrationally Mediated Negative Differential Resistance in a Single Molecule. *Phys. Rev. Lett.* **85**(9), 1918 (2000)

[13] D. M. Eigler, C. P. Lutz and W. E. Rudge. An atomic switch realized with the scanning tunnelling microscope. *Nature* **352**, 600 (1991)

[14] D. M. Eigler and E. K. Schweizer. Positioning single atoms with a scanning tunneling microscope. *Nature* **334**, 524 (1990)

[15] M. F. Crommie, C. P. Lutz and D. M. Eigler. Confinement of electrons to quantum corrals on metal surface. *Science* **262**, 218 (1993)

[16] T. Komeda, Y. Kim, M. Kawai, B. N. J. Persson and H. Ueba. Lateral Hopping of Molecules Induced by Excitation of Internal Vibration Mode. *Science* **295**, 2055 (2002)

[17] B. C. Stipe, M. A. Rezaei and W. Ho. Coupling of Vibrational Excitation to the Rotational Motion of a Single Adsorbed Molecule. *Phys. Rev. Lett.* **81**, 1263 (1998)

[18] J. I. Pascual, N. Lorente, Z. Song, H. Conrad and H.-P. Rust. Selectivity in vibrationally mediated single-molecule chemistry. *Nature* **423**, 525 (2003)

[19] J. Repp, G. Meyer, S. Paavilainen, F. E. Olsson and M. Persson. Imaging Bond Formation Between a Gold Atom and Pentacene on an Insulating Surface. *Science* **312**, 1196 (2006)

[20] J. R. Hahna and W. Ho. Chemisorption and dissociation of single oxygen molecules on Ag(110). *J. Chem. Phys.* **123**, 214702 (2005)

[21] Y. Kim, T. Komeda and M. Kawai. Single-Molecule Reaction and Characterization by Vibrational Excitation. *Phys. Rev. Lett.* **89**, 126104 (2002)

[22] J. R. Hahn and W. Ho. Oxidation of a Single Carbon Monoxide Molecule Manipulated and Induced with a Scanning Tunneling Microscope. *Phys. Rev. Lett.* **87**(16), 166102 (2001)

[23] S. W. Wu, N. Ogawa and W. Ho. Atomic-Scale Coupling of Photons to Single-Molecule Junctions. *Science* **312**, 1362 (2006)

[24] P. Moriarty. Nanostructured Materials. *Rep. Prog. Phys.* **64**, 297 (2001)

[25] M. S. Dresselhaus, G. Dresselhaus and P. C. Eklund. *Science of Fullerenes and Carbon Nanotubes* (Acedemic Press, San Diego, 1996)

[26] P. M. Allemand, K. C. Khemani, A. Koch, F. Wudl, K. Holczer, S. Donovan, G. Gruner and J. D. Thompson. Organic Molecular Soft Ferromagnetism in a Fullerene C_{60}. *Science* **253**, 301 (1991)

[27] A. F. Hebard, M. J. Rosseinsky, R. C. Haddon, D. W. Murphy, S. H. Glarum, T. T. M. Palstra, A. P. Ramirez and A. R. Kortan. Superconductivity at 18 K in potassium-doped C_{60}. *Nature* **350**, 600 (1991)

[28] A. M. Rao, P. Zhou, K. A. Wang, G. T. Hager, J. M. Holden, Y. Wang, W. T. Lee, X. X. Bi, P. C. Eklund, D. S. Cornett, M. A. Duncan and I. J. Amster. Photoinduced polymerization of solid C_{60} films. *Science* **259**, 955 (1993)

[29] R. Taylor and D. R. M. Walton. The chemistry of fullerenes. *Nature* **363**, 685 (1993)

[30] H. Shinohara. Endohedral Metallofullerenes. *Rep. Prog. Phys.* **63**, 843 (2000)

[31] S. Guha and K. Nakamoto. Electronic and spectral properties of endohedral fullerenes. *Coord. Chem. Rev.* **249**, 1111 (2005)

[32] S. Bosi, T. D. Ros, G. Spalluto and M. Prato. Fullerene derivatives: an attractive tool for biological applications. *Eur. J. Med. Chem.* **38**, 913 (2003)

[33] S. Kobayashi, S. Mori, S. Iid, H. Ando, T. Takenobu, Y. Taguchi, A. Fujiwara, A. Taninaka, H. Shinohara and Y. Iwasa. Conductivity and Field Effect Transistor of $La_2@C_{80}$ Metallofullerene. *J. Am. Che. Soc.* **125**, 8116 (2003)

[34] W. Harneit. Fullerene-based electron-spin quantum computing. *Phys. Rev. A* **65**, 032322 (2002)

[35] J. A. Larsson, J. C. Greer, W. Harneit and A. Weidinger. Phosphorous trapped within buckminsterfullerene. *J. Chem. Phys.* **116**, 7849 (2002)

[36] H. Kato, Y. Kanazawa, M. Okumura, A. Taninaka, T. Yokawa and H. Shinohara. Lanthanoid endohedral metallofullerenols for MRI contrast agents. *J. Am. Chem. Soc.* **125**, 4391 (2003)

[37] J. Bardeen. Tunnelling from a many-particle point of view. *Phys. Rev. Lett.* page 57 (1961)

[38] J. Tersoff and D. Hamann. Theory and application for the scanning tunneling microscope. *Phys. Rev. Lett.* **50**, 1998 (1983)

[39] J. Tersoff and D. Hamann. Theory of scanning tunneling microscope. *Phys. Rev. B* **31**(2), 805 (1985)

[40] J. A. Stroscio, R. M. Feenstra and A. P. Fein. Electronic Structure of the Si(111)-(2×1) Surface by Scanning-Tunneling Microscopy. *Phys. Rev. Lett.* **57**, 2579 (1986)

[41] R. M. Feenstra, J. A. Stroscio and A. P. Fein. Tunneling spectroscopy of the Si(111)-(2×1) surface. *Surf. Sci.* **181**, 295 (1987)

[42] J. A. Stroscio and R. M. Feenstra. In: *Scanning Tunneling Microscopy*, edited by J. A. Stroscio and W. J. Kaiser (Academic Press, San Diego, 1993)

[43] N. D. Lang. Spectroscopy of single atoms in the scanning tunneling microscope. *Phys. Rev. B* **34**(8), 5947 (1986)

[44] J. Mysliveček, A. Stróżecka, J. Steffl, P. Sobotík, I. Ošt'ádal and B. Voigtländer. Structure of the Adatom Electron Band of the Si(111)-(7×7) Surface. *Phys. Rev. B* **73**, 161302 (2006)

[45] R. C. Jacklevic and J.Lambe. Molecular vibration spectra by electron tunneling. *Phys. Rev. Lett.* **17**, 1139 (1966)

[46] G. Binnig, N. Garcia and H. Rohrer. Conductivity sensitivity of inelastic scanning tunneling microscopy. *Phys. Rev. B* **32**, 1336 (1985)

[47] T. Komeda, Y. Kim, M. Kawai, B. N. J. Persson and H. Ueba. Lateral Hopping of Molecules Induced by Excitation of Internal Vibration Mode. *Science* **295**, 2055 (2002)

[48] B. C. Stipe, M. A. Rezaei and W. Ho. Inducing and Viewing the Rotational Motion of a Single Molecule. *Science* **279**, 1907 (1998)

[49] F. Moresco. In: *Scanning Probe Microscopies Beyond Imaging*, edited by P. Samori (John Wiley & Sons, New York, 2005)

[50] M. Ternes. *Scanning tunneling spectroscopy at the single atom scale*. Ph.D. thesis, EPFL, Lausanne (2006)

[51] L. J. Lauhon and W. Ho. Effects of temperature and other experimental variables on single molecule vibrational spectroscopy with the scanning tunneling microscope. *Rev. Sci. Inst.* **72**(1), 216 (2001)

[52] B. N. J. Persson and A. Baratoff. Inelastic electron tunneling from a metal tip: contribution from resonant processes. *Phys. Rev. Lett.* **59**(3), 339 (1987)

[53] N. Lorente. Mode excitation induced by the scanning tunnelling microscope. *Appl. Phys. A* **78**, 799 (2004)

[54] N. Lorente, M. Persson, L. J. Lauhon and W. Ho. Symmetry Selection Rules for Vibrationally Inelastic Tunneling. *Phys. Rev. Lett.* **86**(12), 2593 (2001)

[55] N. Lorente and M. Persson. Theory of Single Molecule Vibrational Spectroscopy and Microscopy. *Phys. Rev. Lett.* **85**(14), 2997 (2000)

[56] E. J. Heller, M. F. Crommie, C. P. Lutz and D. M. Eigler. Scattering and absorption of surface electron waves in quantum corrals. *Nature* **369**, 464 (1994)

[57] K.-F. Braun and K.-H. Rieder. Engineering Electronic Lifetimes in Artificial Atomic Structures. *Phys. Rev. Lett.* **88**(9), 096801 (2002)

[58] H. C. Manoharan, C. P. Lutz and D. M. Eigler. Quantum mirages formed by coherent projection of electronic structure. *Nature* **403**, 512 (2000)

[59] T. A. Jung, R. R. Schlittler, J. K. Gimzewski, H. Tang and C. Joachim. Controlled Room-Temperature Positioning of Individual Molecules: Molecular Flexure and Motion. *Science* **271**, 181 (1996)

[60] D. L. Keeling, M. J. Humphry, R. H. J. Fawcett, P. H. Beton, C. Hobbs and L. Kantorovich. Bond Breaking Coupled with Translation in Rolling of Covalently Bound Molecules. *Phys. Rev. Lett.* **94**, 146104 (2005)

[61] L. Bartels, G. Meyer and K.-H. Rieder. Basic Steps of Lateral Manipulation of Single Atoms and Diatomic Clusters with a Scanning Tunneling Microscope Tip. *Phys. Rev. Lett.* **79**(4), 697 (1997)

[62] S.-W. Hla, K.-F. Braun and K.-H. Rieder. Single-atom manipulation mechanisms during a quantum corral construction. *Phys. Rev. B* **67**, 201402R (2003)

[63] F. Moresco, G. Meyer, K.-H. Rieder, H. Tang, A. Gourdon and C. Joachim. Recording Intramolecular Mechanics during the Manipulation of a Large Molecule. *Phys. Rev. Lett.* **87**(8), 088302 (2001)

[64] K.-F. Braun and S.-W. Hla. Force measurement with a scanning tunneling microscope. *Phys. Rev. B* **75**, 033406 (2007)

[65] H. W. Kroto, J. R. Heath, S. C. O'Brien, R. F. Curl and R. E. Smalley. C_{60}: Buckminsterfullerene. *Nature* **318**, 162 (1985)

[66] S. Iijima. Helical microtubules of graphitic carbon. *Nature* **354**, 56 (1991)

[67] K. S. Novoselov, A. K. Geim, S. V. Morozov, D. Jiang, Y. Zhang, S. V. Dubonos, I. V. Grigorieva and A. A. Firsov. Electric Field Effect in Atomically Thin Carbon Films. *Science* **306**, 666 (2004)

[68] W. Kraetschmer, L. D. Lamb, K. Foristopoulos and D. R. Huffman. Solid C_{60}: A new form of carbon. *Nature* **347**, 354 (1990)

[69] H. W. Kroto. The stability of the fullerenes C_n with $n = 24$, 28, 32, 36, 50, 60 and 70. *Nature* **329**, 529 (1987)

[70] R. C. Haddon. Electronic Structure, Conductivity and Superconductivity of Alkali Metal Doped C_{60}. *Acc. Che. Res.* **25**, 127 (1992)

[71] R. L. Carter. *Molecular symmetry and group theory* (John Wiley & Sons)

[72] Z. H. Dong, P. Zhou, J. M. Holden, P. Eklund, M. S. Dresselhaus and G. Dresselhaus. Observation of higher-order Raman modes in C_{60} films. *Phys. Rev. B* **48**, 2862 (1993)

[73] K. A. Wang, A. M. Rao, P. C. Eklund, M. S. Dresselhaus and G. Dresselhaus. Observation of higher-order infrared modes in solid C_{60} films. *Phys. Rev. B* **48**, 11375 (1993)

[74] R. A. Jishi, R. M. Mirie and M. S. Dresselhaus. Force-constant model for the vibrational modes in C_{60}. *Phys. Rev. B* **45**, 13685 (1992)

[75] A. A. Quong, M. R. Pederson and J. L. Feldman. First principles determination of the interatomic force-constant tensor of the fullerene molecule. *Solid State Commun.* **87**, 535 (1993)

[76] J. L. Feldman, J. Q. Broughton, L. L. Boyer, D. E. Reich and M. D. Kluge. Intramolecular-force-constant model for C_{60}. *Phys. Rev. B* **46**, 12731 (1992)

[77] P. W. Fowler and D. E. Monolopoulos. *An atlas of fullerenes* (Oxford University Press, Oxford, 1995)

[78] R. C. Haddon. Conducting films of C_{60} and C_{70} by alkali-metal doping. *Nature* **350**, 320 (1991)

[79] J. Heith, S. C. O'Brien, Q. Zhang, Y. Liu, R. F. Curl, H. W. Kroto, F. K. Tittel and R. E. Smalley. Lanthanum Complexes of Spheroidal Carbon Shells. *J. Am. Chem. Soc.* **107**, 7779 (1985)

[80] M. Takata, B. Umeda, E. Nishibori, M. Sakata, Y. Saito, M. Ohno and H. Shinohara. Confirmation by X-ray diffraction of the endohedral nature of the metallofullerene $Y@C_{82}$. *Nature* **377**, 46 (1995)

[81] M. Sakata, R. Mori, S. Kumazawa, M. Takata and H. Toraya. Electron-density distribution form the x-ray powder data by use of profile fits and the maximum-entropy method. *J. Appl. Phys.* **23**, 526 (1990)

[82] S. Stevenson, G. Rice, T. Glass, K. Harich, F. Cromer, M. R. Jordan, J. Craft, E. Hadju, R. Bible, M. M. Olmstead, K. Maitra, A. J. Fisher, A. L. Balch and H. C. Dorn. Small-bandgap endohedral metallofullerenes in high yield and purity. *Nature* **401**, 55 (1999)

[83] M. Saunders, R. J. Cross, H. A. Jiménez-Vázquez, R. Shimshi and A. Khong. Noble Gas Atoms Inside Fullerenes. *Science* **271**, 14281693 (1996)

[84] B. Pietzak, M. W. nad T. A. Murphy, A. Weidinger, M. Hohne, E. Dietel and A. Hirsch. Buckminsterfullerene C_{60}: a chemical Faraday cage for atomic nitrogen. *Chem Phys. Lett.* **279**, 259 (1997)

[85] Y. Chai, T. Guo, E. D. Haufler, L. P. F. Chibante, J. Fure, L. Wang, J. M. Alford and R. E. Smalley. Fullerenes with metals inside. *J. Phys. Chem.* **95**, 7564 (1991)

[86] B.-B. Liu, G.-T. Zou, H.-B. Yang, S. Yu, J.-S. Lu, Z.-Y. Liu, S.-Y. Liu and W.-G. Xu. Synthesis, extraction and electronic structure of $Ce@C_{2n}$. *J. Phys. Chem. Solids* **58**, 1837 (1997)

[87] J. Ding and S. Yang. Systematic Isolation of endohedral fullerenes containing lathanide atom and their characterization. *J. Phys. Chem. Solids* **58**, 1661 (1997)

[88] J. Ding and S. Yang. Isolation and Characterization of the Dimetallofullerene $Ce_2@C_{80}$. *Ang. Chem. Int. Ed.* **35**, 2234 (1996)

[89] A. J. Martin and R. L. Synge. *Biochem. J.* **35**, 1358 (1941)

[90] R. Taylor, J. P. Hare, A. K. Abdul-Sada and H. Kroto. *J. Chem. Soc. Chem. Commun.* **20**, 1423 (1990)

[91] K. Muthukumar and J. A. Larsson. Structural, Vibrational and Electronic Structure Characterisation of $Ce@C_{82}$: a Density Functional Study. accepted by *J. Phys. Chem. A* (2007)

[92] Y. Rikiishi, Y. Kubozono, T. Hosokawa, K. Shibata, Y. H. nad Yasuhiro Takabayashi, A. Fujiwara, S. Kobayashi, S. Mori and Y. Iwasa. Structural and Electronic Characterizations of Two Isomers of $Ce@C_{82}$. *J. Phys. Chem. B* **108**, 7580 (2004)

[93] K. Shibata, Y. Rikiishi, T. Hosokawa, Y. Haruyama, Y. Kubozono, S. Kashino, T. Uruga, A. Fujiwara, H. Kitagawa, T. Takano and Y. Iwasa. Structural and electronic properties of $Ce@C_{82}$. *Phys. Rev. B* **68**, 094104 (2003)

[94] E. Nishibori, M. Takata, M. Sakata, H. Tanaka, M. Hasegawa and H. Shinohara. Giant motion of La atom inside C_{82} cage. *Chem. Phys. Lett.* **330**, 497 (2000)

[95] W. Andreoni and A. Curioni. Ab initio approach to the structure and dynamics of metallofullerenes. *Appl. Phys. A* **66**, 299 (1998)

[96] K. Kobayashi and S. Nagase. Structures and electronic states of endohedral dimetallofullerenes: M_2@C_{80} (M=Sc, Y, La, Ce, Pr, Eu, Gd, Yb and Lu). *Chem. Phys. Lett.* **262**, 227 (1996)

[97] E. Nishibori, M. Takata, M. Sakata, A. Taninaka and H. Shinohara. Pentagonal-Dodecahedral La_2 Charge Density in [80-I_h]Fullerene: La_2@C_{80}. *Ang. Chem. Int. Ed.* **40**, 2998 (2001)

[98] S. Nagase, K. Kobayashi and T. Akasaka. Endohedral Metallofullerenes: New Spherical Cage Molecules with Interesting Properties. *Bull. Che. Soc. Jpn.* **69**, 2131 (1996)

[99] L. Mora, R. S. Ruoff, C. H. Becker, D. C. Lorents and R. Malhotra. Studies of Metallofullerene Primary Soots by Laser and Thermal Desorption Mass Spectrometry. *J. Phys. Chem.* **97**, 6801 (1993)

[100] H. Funasaka, K. Sugiyama, K. Yamamoto and T. Takahashi. Magnetic Properties of Rare-Earth Metallofullerenes. *J. Phys. Chem.* **99**, 1826 (1995)

[101] K. Laasonen, W. Andreoni and M. Parrinello. Structural and Electronic Properties of La@C_{82}. *Science* **258**, 1916 (1992)

[102] J. Ding, L.-T. Weng and S. Yang. Electronic Structure of Ce@C_{82}: An Experimental Study. *J. Phys. Chem.* **100**, 11120 (1996)

[103] T. Pichler, M. S. Golden, M. Knupfer, J. Fink, U. Kirbach, P. Kuran and L. Dunsch. Monometallofullerene Tm@C_{82}: Proof of an Encapsulated Divalent Tm Ion by High-Energy Spectroscopy. *Phys. Rev. Lett.* **79**, 3026 (1997)

[104] B. Kessler, A. Bringer, S. Cramm, C. Schlebusch, W. Eberhardt, S. Suzuki, Y. Achiba, F. Esch, M. Barnaba and D. Cocco. Evidence for Incomplete Charge Transfer and La-Derived States in the Valence Bands of Endohedrally Doped La@C_{82}. *Phys. Rev. Lett.* **79**, 2289 (1997)

[105] S. Lebedkin, B. Renker, R.Heid, H. Schober and H. Rietschel. A spectroscopic study of M@C_{82} metallofullerenes: Raman, far-infrared, and neutron scattering results. *Appl. Phys. A* **66**, 273 (1998)

[106] R. Jaffiol, A. Debarre, C. Julien, D. Nutarelli, P. Tchenio, A. Taninaka, B. Cao, T. Okazaki and H. Shinohara. Raman spectroscopy of La_2@C_{80} and Ti_2@C_{80} dimetallofullerenes. *Phys. Rev. B* **68**, 014105 (2003)

[107] M. Krause, M. Hulmana, H. Kuzmany, P. Kuranb, L. Dunschb, T. J. S. Dennis, M. Inakuma and H. Shinohara. Low-energy vibrations in Sc_2@C_{84} and Tm@C_{82} metallofullerenes with different carbon cages. *J. Mol Struc.* **521**, 325 (2000)

[108] M. Krause, P. Kuran, U. Kirbach and L. Dunsch. Raman and infrared spectra of Tm@C_{82} and Gd@C_{82}. *Carbon* **37**, 113 (1999)

[109] T. Wågberg, P. Launois, R. Moret, H. Huang, S. Yang, I. Li and Z. Tang. Study by X-ray diffraction and Raman spectroscopy of a DyC82 single crystal. *Eur. Phys. J. B* **35**, 371 (2003)

[110] T. Hosokawa, S. Fujiki, E. Kuwahara, Y. Kubozono, H. Kitagawa, A. Fujiwara, T. Takenobu and Y. Iwasa. Electronic properties for the C_{2v} and C_s isomers of Pr@C_{82} studied by Raman, resistivity and scanning tunneling microscopy/spectroscopy. *Chem. Phys. Lett.* **395**, 78 (2004)

[111] M. Moriyama, T. Sato, A. Yabe, K. Yamamoto, K. Kobayashi, S. Nagase, T. Wakahara and T. Akasaka. Vibrational Spectroscopy of Endohedral Dimetallofullerene, La_2@C_{80}. *Chem. Lett.* page 524 (2000)

[112] H. Shimotani, T. Ito, Y. Iwasa, A. Taninaka, H. Shinohara, E. Nishibori, M. Takata and M. Sakata. Quantum Chemical Study on the Configurations of Encapsulated Metal Ions and the Molecular Vibration Modes in Endohedral Dimetallofullerene La_2@C_{80}. *J. Am. Chem. Soc.* **126**, 364 (2004)

[113] M. Kanai. *Production, Isolation and Characterization of Incar-Fullerenes*. Ph.D. thesis, Queen Mary University of London (2004)

[114] K. Tanaka, H. Waki, Y. Ido, S. Akita, Y. Yoshida and T. Yoshida. *Rapid Commun. Mass Spectrom.* **2**, 151 (1988)

[115] S. Zöphel. *Der Aufbau eines Tieftemperatur-Rastertunnelmikroskops und Strukturuntersuchungen auf vicinalen Kupferoberflachen*. Ph.D. thesis, Freie Universtiät Berlin (2000)

[116] R. J. Wilson, G. Meijer, D. S. Bethune, R. D. Johnson, D. D. Chambliss, M. S. de Vries, H. E. Hubziker and H. R. Wendt. Imaging C_{60} clusters on a surface using a scanning tunnelling microscope. *Nature* **348**, 621 (1990)

[117] T. Hashizume, K. Motai, X. D. Wang, H. Shinohara, Y. Saito, Y. Maruyama, K. Ohno, Y. Kawazoe, Y. Nishina, H. W. Pickering, Y. Kuk and T. Sakurai. Intramolecular Structures of C_{60} Molecules Adsorbed on the Cu(111)-(1x1) Surface. *Phys. Rev. Lett.* **71**, 2959 (1993)

[118] X.-D. Wang, T. Hashizume, H. Shinohara, Y. Saito, Y. Nishina and T. Sakurai. Adsorption of C_{60} and C_{84} on the Si(100)-(2x1) surface studied by using the scanning tunneling microscope. *Phys.Rev. B* **47**, 15923 (1993)

[119] N. A. Pradhan, N. Liu and W. Ho. Vibronic Spectroscopy of Single C_{60} Molecules and Monolayers with the STM. *J. Phys. Chem. B* **109**, 8513 (2005)

[120] C. Silien, N. A. Pradhan, W. Ho and P. A. Thiry. Influence of adsorbate-substrate interaction on the local electronic structure of C_{60} studied by low-temperature STM. *Phys. Rev. B* **69**, 115434 (2004)

[121] N. Liu, N. A. Pradhan and W. Ho. Vibronic states in single molecules: C_{60} and C_{70} on ultrathin Al_2O_3 films. *J. Chem. Phys.* **120**, 11371 (2004)

[122] J. I. Pascual, J. Gómez-Herrero, D. Sánchez-Portal and H.-P. Rust. Vibrational spectroscopy on single C_{60} molecules: The role of molecular orientation. *J. Chem. Phys.* **117**, 9531 (2002)

[123] J. I. Pascual, J. Gómez-Herrero, C. Rogero, A. Baró, D. Sánchez-Portal, E. Artacho, P. Ordejón and J. Soler. Seeing molecular orbitals. *Che. Phys. Lett.* **321**, 78 (2000)

[124] C. Rogero, J. I. Pascual, J. Gómez-Herrero and A. M. Baró. Resolution of site-specific bonding properties of C_{60} adsorbed on Au(111). *J. Chem Phys.* **116**, 832 (2002)

[125] X. Lu, M. Grobis, K. H. Khoo, S. G. Louie and M. F. Crommie. Charge transfer and screening in individual C_{60} molecules on metal substrates: a scanning tunneling spectroscopy and theoretical study. *Phys. Rev. B* **70**, 115418 (2004)

[126] X. Lu, M. Grobis, K. H. Khoo, S. G. Louie and M. F. Crommie. Spatially Mapping the Spectral Density of a Single C_{60} Molecule. *Phys. Rev. Lett.* **90**, 096802 (2003)

[127] R. W. G. Wyckoff. *Crystal Structures* (John Wiley & Sons, New York, 1963)

[128] W. Shockley. On the surface states associated with a periodic potential. *Phys. Rev.* **56**, 317 (1939)

[129] H. Ibach. *Physics of Surfaces and Interfaces* (Springer, Berlin, 2006)

[130] G. Hormadinger. Imaging of the Cu(111) surface state in scanning tunneling microscopy. *Phys. Rev. B* **49**, 13897 (1994)

[131] M. F. Crommie, C. P. Lutz and D. M. Eigler. Imaging standing waves in a two-dimensional electron gas. *Nature* **363**, 524 (1993)

[132] J. Li, W.-D. Schneider, R. Berndt, O. R. Bryant and S. Crampin. Surface-state lifetime measured by scanning tunneling spectroscopy. *Phys. Rev. Lett.* **81**, 4464 (1998)

[133] R. Hoffmann. A chemical theoretical way to look at the bonding on surfaces. *Rev. Mod. Phys.* **60**, 601 (1988)

[134] C. Cepek, A. Goldoni and S. Modesti. Chemisorption and fragmentation of C_{60} on Pt(111) and Ni(110). *Phys. Rev. B* **53**, 7466 (1996)

[135] M. R. C. Hunt, S. Modesti, P. Rudolf and R. E. Palmer. Charge transfer and structure in C_{60} adsorption on metal surfaces. *Phys. Rev. B* **51**, 10039 (1995)

[136] K.-D. Tsuei, J.-Y. Yuh, C.-T. Tzeng, R.-Y. Chu and W.-S. Lo. Photoemission and photoabsorption study of C_{60} adsorption on Cu(111) surfaces. *Phys. Rev. B* **56**, 15412 (1997)

[137] L.-L. Wang and H.-P. Cheng. Rotation, translation, charge transfer, and electronic structure of C_{60} on Cu(111) surface. *Phys. Rev. B* **69**, 045404 (2004)

[138] C.-T. Tzeng, W.-S. Lo, J.-Y. Yuh, R.-Y. Chu and K.-D. Tsuei. Photoemission, near-edge x-ray-absorption spectroscopy, and low-energy electron-diffraction study of C_{60} on Au(111) surfaces. *Phys. Rev. B* **61**, 2263 (2000)

[139] L. H. Tjeng, R. Hesper, A. C. L. Heessels, A. Heeres, H. T. Jonkman and G. A. Sawatzky. Development of the electronic structure in a K-doped C_{60} monolayer on a Ag(111) surface. *Solid State Commun.* **103**, 31 (1997)

[140] A. Stróżecka, J. Mysliveček and B. Voigtländer. Scanning tunneling spectroscopy and manipulation of C_{60} on Cu(111). *Appl. Phys. A* **87**, 475 (2007)

[141] M. Grobis, X. Lu and M. F. Crommie. Local electronic properties of a molecular monolayer: C_{60} on Ag(001). *Phys. Rev. B* **66**, 161408(R) (2002)

[142] J. A. Larsson, S. D. Elliott, J. C. Greer, J. Repp, G. Meyer and R. Allenspach. Orientation of Individual C_{60} Molecules Adsorbed on Cu(111): Low- Temperature Scanning Tunneling Microscopy and Density Functional Calculations. submitted (2007)

[143] G. K. Wertheim and D. N. E. Buchanan. Onterfacial reaction of C_{60} with silver. *Phys. Rev. B* **50**, 11070 (1994)

[144] K.-D. Tsuei and P. Johnson. Charge transfer and a new image state of C_{60} on Cu(111) surface studied by inverse photoemission. *Solid State Comm.* **101**, 337 (1997)

[145] C. Silien, I. Marenne, J. Auerhammer, N. Tagmatatchis, K. Prassides, P. A. Thiry and P. Rudolf. Adsorption of fullerene and azafullerene on Cu(111) studied by electron energy loss spectroscopy. *Surf. Sci.* **482-485**, 1 (2001)

[146] S. J. Chase, W. S. Bacsa, M. G. Mitch, L. J. Pilione and J. S. Lannin. Surface-enhanced Raman scattering and photoemission of C_{60} on noble-metal surface. *Phys. Rev. B* **46**, 7873 (1992)

[147] M. T. Cuberes, R. R. Schlittler and J. K. Gimzewski. Room-temperature repositioning of individual C_{60} molecules at Cu steps: Operation of a molecular counting device. *Appl. Phys. Lett.* **69**, 3016 (1996)

[148] M. T. Cuberes, R. R. Schlittler and J. K. Gimzewski. Manipulation of C_{60} molecules on Cu(111) surfaces using a scanning tunneling microscope. *Appl. Phys. A* **66**, S669 (1998)

[149] A. W. D. P. H. Beton and P. Moriarty. Manipulation of C_{60} molecules on a Si surface. *Appl. Phys. Lett.* **67**, 1075 (1995)

[150] C. Ton-That, A. Shard, S. Egger, A. Taninaka, H. Shinohara and M. Welland. Structural and electronic properties of ordered La@C_{82} films on Si(111). *Surf. Sci. Lett.* **522**, L15 (2003)

[151] A. Taninaka, K. Shino, T. Sugai, S. Heike, Y. Terada, T. Hashizume and H. Shinohara. Scanning Tunneling Microscopy / Spectroscopy Studies of Lanthanum Endohedral Metallofullerenes. *Nano Lett.* **3**, 337 (2003)

[152] S. Fujiki, Y. Kubozono, Y. Rikiishi, and T. Urisu. Scanning tunneling microscopy/spectroscopy studies of two isomers of Ce@C_{82} on Si(111)-(7x7) surfaces. *Phys. Rev. B* **70**, 235421 (2004)

[153] D. F. Leigh, J. Owen, S. M. Lee, K. Porfyrakis, A. Ardavan, T. J. Dennis, D. Pettifor and G. A. D. Briggs. Distinguishing two isomers of Nd@C_{82} by scanning tunneling microscopy and density functional theory. *Chem. Phys. Lett.* **414**, 307 (2005)

[154] K. Wang, J. Zhao, S. Yang, L. Chen, Q. Li, B. Wang, S. Yang, J. Yang, J. Hou and Q. Zhu. Unveiling Metal-Cage Hybrid States in a Single Endohedral Metallofullerene. *Phys. Rev. Lett.* **91**, 185504 (2003)

[155] M. Grobis, K. H. Khoo, R. Yamachika, X. Lu, K. Nagaoka, S. G. Louie, M. F. Crommie, H. Kato and H. Shinohara. Spatially Dependent Inelastic Tunneling in a Single Metallofullerene. *Phys. Rev. Lett.* **94**, 136802 (2005)

[156] J. P. Perdew, K. Burke and M. Ernzerhof. Generalized Gradient Approximation Made Simple. *Phys. Rev. Lett.* **77**, 3865 (1996)

[157] A. Schäfer, C. Huber and R. Ahlrichs. Fully optimized contracted Gaussian basis sets of triple zeta valence quality for atoms Li to Kr. *J. Phys. Chem.* **100**, 5829 (1994)

[158] M. Dolg, H. Stoll and H. Preuss. Energy-adjusted ab initio pseudopotentials for the rare earth elements. *J. Chem. Phys.* **90**, 1730 (1989)

[159] R. Ahlrichs, M. Baer, M. Haeser, H. Horn and C. Koelmel. Electronic structure calculation on workstation computers: the program system TURBOMOLE. *Chem. Phys. Lett.* **162**, 165 (1989)

[160] L. Wang, K. Schulte, R. Woolley, M. Kanai, T. Dennis, J. Purton, S. Patel, S. Gorovikov, V. Dhanak, E. Smith, B. Cowie and P. Moriarty. Morphology, structure, and electronic properties of Ce@C_{82} films on Ag:Si(111)-($\sqrt{3} \times \sqrt{3}$)R30°. *Surf. Sci.* **564**, 156 (2004)

[161] K. Schulte, L. Wang, P. J. Moriarty, J. Purton, S. Patel, H. Shinohara, M. Kanai and T. J. S. Dennis. Well-shielded cerium atoms: Electronic structure of adsorbed Ce@C_{82} on Si surfaces. *Phys. Rev. B* **71**, 115437 (2005)

[162] R. A. J. Woolley, K. H. G. Schulte, L. Wang, P. J. Moriarty, B. C. C. Cowie, H. Shinohara, M. Kanai and T. J. S. Dennis. Does an Encapsulated Atom 'feel' the Effects of Adsorption?: X-ray Standing Wave Spectroscopy of Ce@C_{82} on Ag(111). *Nano Lett.* **4**, 361 (2004)

[163] D. Poirier, M. Knupfer, J. Weaver, W. Andreoni, K. Laasonen, M. Parrinello, D. Bethune, K. Kikuchi and Y. Achiba. Electronic and geometric structure of La@C_{82} and C_{82}: Theory and Experiment. *Phys. Rev. B* **49**, 17403 (1994)

[164] A. Taninaka, H. Kato, K. Sato, T. Sigai, S. Heike and Y. Terada. Scanning Tunneling Microscopy / Spectroscopy of La_2@C_{72} Multilayer Islands on Si(100)-(2x1)-H Surfaces. *Jap. J. Appl Phys.* **44**, 3226 (2005)

[165] S. Hino, N. Wanita, M. Kato, K. Iwasaki, D. Yoshimura, T. Inoue, T. Okazaki and H. Shinohara. Ultraviolet photoelectron spectroscopy of multiple atoms encapsulated fullerenes. *J. El .Spect. Rel. Phen.* **144**, 239 (2005)

[166] W. Xiao, P. Ruffieux, K. Aït-Mansour, O. Gröning, K. Palotas, W. A. Hofer, P. Groning and R. Fasel. Formation of a Regular Fullerene Nanochain Lattice. *J. Phys. Chem. B* **110**, 21394 (2006)

[167] A. Schäfer, H. Horn and R. Ahlrichs. Fully Optimized Contracted Gaussian Basis Sets for Atoms Li to Kr. *J. Chem. Phys.* **97**, 2571 (1992)

[168] H. Park, J. Park, A. K. L. Lim, E. H. Anderson, A. P. Alivisatos and P. L. McEuen. Nanomechanical oscillations in a single-C_{60} transistor. *Nature* **407**, 57 (2000)

[169] W. Sato, K. Sueki, K. Kikuchi, S. Suzuki, Y. Achiba, H. Nakahara, Y. Ohkubo, K. Asai and F. Ambe. Molecular and intramolecular dynamics of a C_{80} dimetallofullerene. *Phys. Rev. B* **58**, 10850 (1998)

[170] W. A. Hofer, G. Teobaldi and N. Lorente. Creating pseudo Kondo-resonances by field-induced diffusion of atomic hydrogen (2007). arXiv:0706.1516

[171] J. Kondo. Resistance Minimum in Dilute Magnetic Alloys. *Prog. Theor. Phys.* **32**, 37 (1964)

[172] L. Kouwenhoven and L. Glazman. Revival of the Kondo effect. *Physics World* **33** (2001)

[173] V. Madhavan, W. Chen, T. Jamneala, M. F. Crommie and N. S. Wingreen. Tunneling into a Single Magnetic Atom: Spectroscopic Evidence of the Kondo Resonance. *Science* **280**, 567 (1998)

[174] N. Quaas, M. Wenderoth, A. Weismann and R. G. Ulbrich. Kondo resonance of single Co atoms embedded in Cu(111). *Phys. Rev. B* **69**, 201103(R) (2004)

[175] J. Li, W.-D. Schneider, R. Berndt and B. Delley. Kondo Scattering Observed at a Single Magnetic Impurity. *Phys. Rev. Lett.* **80**, 2893 (1998)

[176] A. Zhao, Q. Li, L. Chen, H. Xiang, W. Wang, S. Pan, B. Wang, X. Xiao, J. Yang, J. G. Hou and Q. Zhu. Controlling the Kondo Effect of an Adsorbed Magnetic Ion Through Its Chemical Bonding. *Science* **309**, 1542 (2005)

[177] P. Wahl, L. Diekhöner, G. Wittich, L. Vitali, M. A. Schneider and K. Kern. Kondo Effect of Molecular Complexes at Surfaces: Ligand Control of the Local Spin Coupling. *Phys. Rev. Lett.* **95**, 166601 (2005)

[178] V. Iancu, A. Deshpande and S.-W. Hla. Manipulating Kondo Temperature via Single Molecule Switching. *Nano Lett.* **6**, 820 (2006)

[179] V. Iancu, A. Deshpande and S.-W. Hla. Manipulation of the Kondo Effect via Two-Dimensional Molecular Assembly. *Phys. Rev. Lett.* **97**, 266603 (2006)

[180] P. W. Anderson. Localized Magnetic States in Metals. *Phys. Rev.* **124**, 41 (1961)

[181] O. Újsághy, J. Kroha, L. Szunyogh and A. Zawadowski. Theory of the Fano Resonance in the STM Tunneling Density of States due to a Single Kondo Impurity. *Phys. Rev. Lett.* **85**, 2557 (2000)

[182] U. Fano. Effects of Configuration Interaction on Intensities and Phase Shifts. *Phys. Rev.* **124**, 1866 (1961)

[183] R. Galera, D. Givord, J. Pierre, A. P.Murani, J. Schweizer, C. Vettier and K. R. A. Ziebeck. Polarized neutron scattering in Kondo or intermediate valence compounds. *J. Mag. Mag. Mat.* **52**, 103 (1985)

[184] R. Haug and H. Schoeller, eds. *Interacting Electrons in Nanostructures* (Springer, Berlin, 2001)

[185] A. Wachowiak, R. Yamachika, K. H. Khoo, Y. Wang, M. Grobis, D.-H. Lee, S. G. Louie and M. F. Crommie. Visualization of the Molecular Jahn-Teller Effect in an Insulating K_4C_{60} Monolayer. *Science* **310**, 468 (2005)

[186] J. Koch, F. von Oppen and A. V. Andreev. Theory of the Franck-Condon blockade regime. *Phys. Rev. B* **74**, 205438 (2006)

[187] J. M. van Ruitenbeek. In: *Metal Clusters at Surfaces: Structure, Quantum Properties, Physical Chemistry*, edited by K.-H. Meiwes-Broer (Springer, Berlin, 2000)

[188] C. J. Muller, J. M. van Ruitenbeek and L. J. de Jongh. Conductance and supercurrent discontinuities in atomic-scale metallic constrictions of variable width. *Phys. Rev. Lett.* **69**, 140 (1992)

[189] S. Frank, P. Poncharal, Z. L. Wang and W. A. de Heer. Carbon Nanotube Quantum Resistors. *Science* **280**, 1744 (1998)

[190] D. Porath, A. Bezryadin, S. de Vries and C. Dekker. Direct measurement of electrical transport through DNA molecules. *Nature* **403**, 635 (2000)

[191] H. W. Fink and C. Schönenberger. Electrical conduction through DNA molecules. *Nature* **398**, 407 (1999)

[192] B. Q. Xu and N. J. J. Tao. Measurement of single-molecule resistance by repeated formation of molecular junctions. *Science* **301**, 1221 (2003)

[193] M. A. Reed, C. Zhou, C. J. Muller, T. P. Burgin and J. M. Tour. Conductance of a Molecular Junction. *Science* **278**, 252 (1997)

[194] C. Joachim, J. K. Gimzewski, R. R. Schlittler and C. Chavy. Electronic transparence of a single C_{60} molecule. *Phys. Rev. Lett.* **74**, 2102 (1995)

[195] N. Néel, J. Kröger, L. Limot, T. Frederiksen, M. Brandbyge and R. Berndt. Controlled Contact to a C_{60} Molecule. *Phys. Rev. Lett.* **98**, 065502 (2007)

[196] Z. Li, I. Pobelov, B. Han, T. Wandlowski, A. Błaszczyk and M. Mayor. Conductance of redox-active single molecular junctions: an electrochemical approach. *Nanotechnology* **18**, 044018 (2007)

[197] R. Landauer. Electrical resistance of disordered one-dimensional lattices. *Phil. Mag.* **21**, 863 (1970)

[198] E. Scheer, N. Agrait, J. C. Cuevas, A. L. Yeyati, B. Ludoph, A. Martin-Rodero, G. R. Bollinger, J. M. van Ruitenbeek and C. Urbina. The signature of chemical valence in the electrical conduction through a single-atom contact. *Nature* **394**, 154 (1998)

[199] J. K. Gimzewski and R. Möller. Transition from the tunneling regime to point conctact using scanning tunneling microscopy. *Phys. Rev. B* **36**, 1284 (1987)

[200] J. I. Pascual, J. Méndez, J. Gómez-Herrero, A. Baró, N. García and V. T. Binh. Quantum Contact in Gold Nanostructures by Scanning Tunneling Microscopy. *Phys. Rev. Lett.* **71**, 1852 (1993)

[201] L. Olesen, E. Laegsgaard, I. Stensgaard, F. Besenbacher, J. Schiotz, P. Stoltze, K. W. Jacobsen and J. K. Norskov. Quantized conductance in an Atom-Sized Point Contact. *Phys. Rev. Lett.* **72**, 2251 (1994)

[202] L. Limot, J. Kröger, R. Berndt, A. Garcia-Lekue, and W. A. Hofer. Atom Transfer and Single-Adatom Contacts. *Phys. Rev. Lett.* **94**, 126102 (2005)

[203] C. Untiedt, M. J. Caturla, M. R. Calvo, J. J. Palacios, R. C. Segers and J. M. van Ruitenbeek. Formation of a Metallic Contact: Jump to Contact Revisited. *Phys. Rev. Lett.* **98**, 206801 (2007)

[204] N. Néel, J. Kröger, L. Limot and R. Berndt. Conductance of single atoms and molecules studied with a scanning tunnelling microscope. *Nanotechnology* **18**, 044027 (2007)

[205] L. H. Yu and D. Natelson. The Kondo Effect in C_{60} Single-Molecule Transistors. *Nano Lett.* **4**, 79 (2004)

[206] L. Limot, E. Pehlke, J. Kröger and R. Berndt. Surface-State Localization at Adatoms. *Phys. Rev. Lett.* **94**, 036805 (2005)

[207] J. J. Palacios, A. J. Perez-Jimenez, E. Louis and J. A. Verges. Fullerene-based molecular nanobridges: A first-principles study. *Phys. Rev. B* **64**, 115411 (2001)

[208] T. Ono and K. Hirose. First-Principles Study of Electron Conduction Properties of C_{60} Bridges. *Phys. Rev. Lett.* **98**, 026804 (2007)

[209] L. Senapati, J. Schrier and K. B. Whaley. Electronic Transport, Structure and Energetics of Endohedral Gd@C_{82} Metallofullerenes. *Nano Lett.* **4**, 2073 (2004)

Acknowledgements

This project would have not been completed without all the people who have given me help and support during these three years I have spent in Jülich. I want to express my greatest thanks to all of them. I would also like to acknowledge Prof. Harald Ibach, who was at that time the leader of the Institute, for giving me opportunity to work in the Institue of Bio- and Nanosystems in Research Center in Jülich.

My deepest thanks go to my supervisor, Dr Bert Voigtländer. This work would have been impossible without his encouragement and guidance. I am very grateful for the number of fruitful discussion and for giving me the most interesting insight into the field of surface science and STM research.

I also thank Prof. Markus Morgenstern for agreeing to be the second evaluator of this thesis.

I would like to express my gratitude to Dr. Josef Mysliveček for introducing me to the STM and tunneling spectroscopy techniques. He has always been there to help me and I am very grateful for his patience and all the advice he has given me throughout this research.

I was lucky to work with the wonderful people within the 'Nanocage' project, our collaboration has been very successful. I would like to thank all who have contributed to this work: Aneta Dybek, Dr. John Dennis, Kaliappan Muthukumar, Dr. Andreas Larsson, Dr. Karina Schulte and Prof. Philip Moriarty. In particular, I want to thank Aneta for purification of the metallofullerene samples used in this work and 'quick course' in the HPLC technique. I am especially grateful to Muthu and Andreas, who performed the DFT calculations presented in this thesis. The numerous discussions which we had, finally led to much better understanding of the experimental results. I am also thankful to Karina for the great encouragement she has always given me and for the introduction to the synchrotron spectroscopies.

I would like to thank Prof. Nacho Pascual for the helpful discussions and support. I am also grateful to Prof. Jascha Repp for his useful remarks.

Great thanks go to Peter Coenen and Helmut Stollwerk who were helping me with any technical problems in the lab. It was a pleasure for me to work with them.

In addition, I thank also the coworkers in Research Center who contributed to the work, in particular Udo Linke for preparing the single crystal samples and Dr. Thomas Müller for his help with the Turbomole calculation system.

I would like to thank my present and former colleagues from the group: Dr. Vasily Cherepanov, Philipp Jaschinsky, Michel Kazempoor, Dr. Sergey Filimonov, Dr. Jacek Brona and Konstantin Romanyuk for the advice, discussions and the nice time working

together.

My special thanks go to my friends in Germany, especially Lidiya (also for the great time sharing the office!), Agnieszka, Misha, Ania and Damian, and to all my Polish friends in Jülich, for always being there for me. Their support and friendship have meant a lot to me.

Na koniec dziękuję mojej rodzinie, szczególnie rodzicom i siostrze, oraz przyjaciołom w Polsce za to, że zawsze udzielali mi wsparcia i byli ze mną, mimo odległości która nas dzieliła.

The financial support from the Marie Curie Actions is gratefully acknowledged ('NANOCAGE' project, MEST-CT-2004-506854).

Curriculum Vitae

Name:	Anna Stróżecka
Date of Birth:	June 26, 1980 in Bydgoszcz, Poland
Nationality:	Polish

November 2007	PhD thesis at RWTH in Aachen, Germany
2004 - 2007	Research assistant in the group of Dr. Bert Voigtländer at the Institute of Bio- and Nanosystems, Research Center Jülich, Germany
June 2004	Master thesis under supervision of Prof. W. Jaskólski at the Nicolaus Copernicus University in Toruń, Poland *Title:* "Electronic properties of semiconductor quantum dots in electric field: Tight Binding Calculations"
1999 - 2004	Master studies in physics at the Nicolaus Copernicus University in Toruń, Poland
1995 - 1999	High School in Bydgoszcz, Poland